Inverting Solar Spectroscopic Data using the OLA Helioseismic Inversion Method

by

Piyush Agrawal

M.Sc. (Applied Physics), Indian Institute of Technology (ISM), 2013

M.S. (Astrophysics), University of Colorado, Boulder, 2017

A thesis submitted to the

Faculty of the Graduate School of the

University of Colorado in partial fulfillment

of the requirements for the degree of

Doctor of Philosophy

Department of Astrophysical and Planetary Sciences

2021

Committee Members:

Mark P. Rast

Juri Toomre, Chair

Bradley Hindman

Basilio Ruiz Cobo

Ivan Milić

Agrawal, Piyush (Ph.D., Astrophysics)

Inverting Solar Spectroscopic Data using the OLA Helioseismic Inversion Method

Thesis directed by Mark P. Rast

One relies on inversion methods to infer the vertical structure of the solar atmosphere. Given the ill-posed nature of the inverse problems, combined with error sources from spectral noise and neglected higher-order terms, the inverted solutions are unrealistically highly oscillatory in nature. Regularization is required to produce physically meaningful solutions. In SIR inversions, one regularizes by inverting at a few user-defined depth locations (nodes). These nodes set the vertical resolution limit of the inverted atmosphere and do not correspond to the 'true resolution limit' achievable using the data that will be provided by DKIST. It is critical to determine the true resolution limit achievable and invert at that resolution to use the telescope at its full potential.

In this thesis, we, for the first time, apply the Optimally Localized Averages (OLA) inversion method, developed for helioseismology and geoseismology applications, to spectroscopic data to invert for solar photospheric thermodynamic parameters. The method aims to find the 'best possible' solution for a given variable at each depth. We discuss the OLA methodology and advancements we have made to allow inversion for non-linear (large amplitude) perturbations by iteration. 'Edge-effects' caused by non-localized large-scale perturbations are the most challenging aspect in this iterative approach. A hybrid SIR (large-scale, low-resolution) + OLA (small-scale, high-resolution) approach successfully addresses this issue. We discuss inversion results using MURaM atmospheres and make comparisons with SIR inversions. The results are promising, though some limitations remain, and we propose future improvements to address those.

The results of this thesis have broader importance and suggest ways to improve overall inversion capabilities. We show that using response function amplification can improve inherent spectral sensitivity to sub-dominant variables and allow electronic pressure inversion in the presence of unknown temperature perturbations. Additionally, removing redundancies from the response

function matrix can significantly improve its inversion capability. Finally, we demonstrate that the slope of the response function singular value curve can be used as a quantitative metric for assessment of line combinations and their inversion capability. Once line combinations are identified, OLA averaging kernel widths can be used to gain insight into the corresponding inversion quality achievable.

To dadaji, nani, maa, paa

&

my family and friends

Acknowledgements

"Wherever you go, whoever you meet, becomes part of you somehow" - someone awesome. This work would not have been possible without the help of my family, friends and colleagues who were there with me, one way or the other, throughout this amazing journey. Among these were (a list necessarily incomplete and not in any order), Mark Rast, Izna Manzoor, Brice Hawley, Dadaji, Gokul dada, Nani and Nanaji, Maa, Paa, Di, Jiju, Viraj, Nidhi, Shruti, Siddharth, Rudra, Diwakar, all cousins, Mama and Mami (all of them), Mausi and Mausaji (all of them), Gajanand Nanaji and Shakun Naniji, Sanjeev Mama, Jessica Roberts, Jhett Bordwell, Evan Anders, Sam Van Kooten, Nick Erickson, Tristan Weber, Courtney Peck, Neeraj Kulkarni, Nicole, Momo, Jay Chittidi, Sami Starkey, all APS friends, Komal and Daljeet Singh, Bua ji, Sanjay Chacha, Priithu, Ivan Milić, Jelena Pajovic, Leah Andreja, Mckenna Brooks, Paul Christianson, Tom Bogdan, Anand Sahay, Be Rajesh, Saurabh Pandey, Udbhav Ojha, Rishabh Jain, Prakhar Prakash, Sumit Shikhar, Shivangi Garg, Satya Prakash, Suraj Singh, Ankit Goel and my IIT (ISM) friends/juniors/seniors, Brad Hindman, Jason Jackiewicz, Benoit Tremblay, Shashi Kumar (and Kota friends), Michael Knoelker, Liz Knoelker, Alice Lecinski, Mausumi Dikpati, P.S. Gupta, P. Venkatakrishnan, Sanjay Gosain, Lisa Upton, Kevin Reardon, Gianna Cauzzi, Han Uitenbroek, Valentin Martinez Pillet, Serena Criscuoli, Basilio R. Cobo, Milan Gosić, Luis Bellot Rubio, Shah Bahauddin, Sanjiv Tiwari, Rishav and Piyush Kanodia, Sonal and Shilpa Jain, Saurav Kumar (and DAV friends), Jesse Lord, Huzefa Jaliwala, Gaurav Bishnoi, Keri Piehl, Jean-Francois Cossette, Byung Jun and Lindsey Cramer, Tracy Casault, Michelle Erks, Allison Youngblood, Ashutosh Mishra and Krishan Kanhaiya (and all others I forgot to mention here). Thank you very much.

Contents

Chapter

Tables

Table

Figures

Figure

Chapter 1

General Introduction

Our Sun is a G-type main-sequence star. It fuses hydrogen into helium in its core, releasing energy in process. This energy can take over a hundred thousand years to reach the solar surface [38], and then just a little over 8 minutes to make its way to the Earth. The solar radiation is undoubtedly the most important source of energy that drives the biological and physical processes on earth. Without it, our earth would be an inhospitable wasteland.

In addition to radiation, Sun also releases a stream of highly energetic charged particles that make up the solar wind. This wind significantly influences the region of space encompassing the solar system and drives the 'space weather'. Space weather is the variable space environment that can directly or indirectly endanger life on Earth by impacting the functioning and reliability of both space-based and ground-based technological systems. Even though Earth's magnetic field acts as a shield [12] and protects surface technology, from all but the most powerful, by deflecting most of the solar wind particles (see Figure 1.1), understanding it is critical to extending human activity into space. Solar wind particles can cause damage to the satellites and communications systems, cause health risk for astronauts during a solar storm or during future manned missions to Moon or Mars, and in the most extreme cases, cause damage to electrical power grids on Earth. It is very important to understand the behavior of the Sun to be able to predict the occurrence of these events well in advance, so that necessary measures can be taken to protect our technological society.

Further, Sun exhibits striking physical structures such as plages, sunspots, coronal holes, etc.,

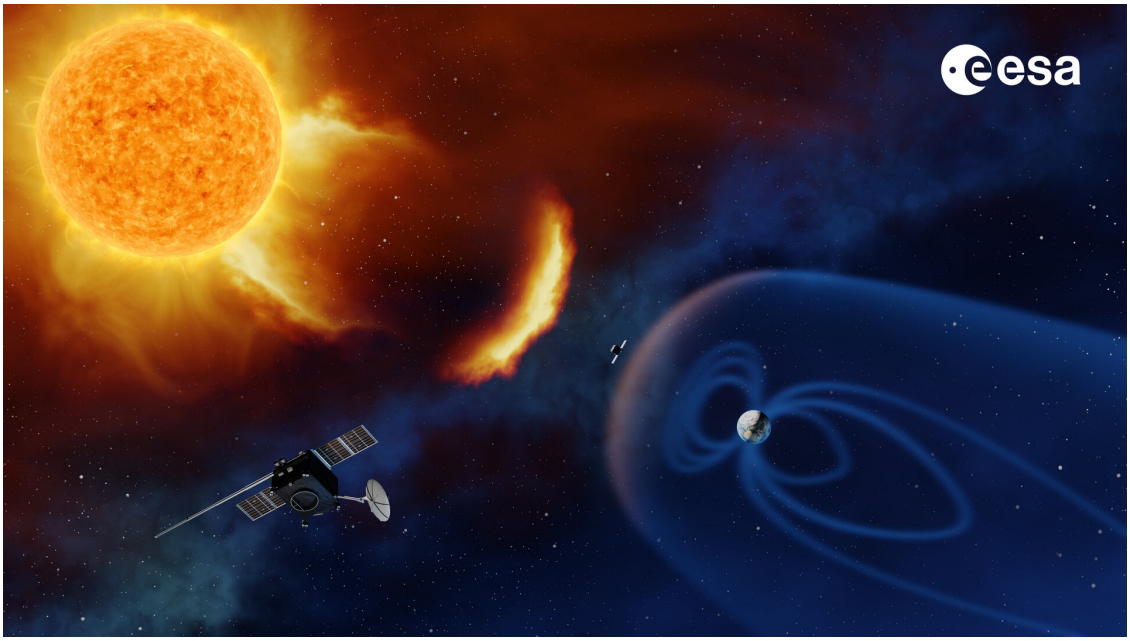

Figure 1.1: Artist render showing the Sun-Earth connection. The bright yellow blob corresponds to the CME traveling towards the Earth, while the Earth's protective magnetic shield is shown in blue. Image credit: ESA.

and its close proximity to us allows us to resolve these structures at great detail e.g. in Figure 1.2 we shows the resolved photospheric granular structures. This means that we can study the Sun in ways which is not possible with any other star. Physical processes such as the operation of solar dynamo [8], which aims to explain the cause for the 11-year solar magnetic cycle, and heating of the solar corona [43], which aims to explain why the corona (uppermost layer of the solar atmosphere) is at about 1 MK while the photosphere (deepest layer of the solar atmosphere) is only at about 6000 K, can be studied in detail. In understanding its workings of the Sun we can learn about processes on other stars and test our theories of stellar evolution.

1.1 Ingredients required to study the Sun

In order to study the Sun in detail, we require a model of its atmospheric structure, its physical properties such as temperature, gas pressure, magnetic flux etc., with height. This structure is highly non-uniform with position. Ideally, we would want to make direct measurements. But

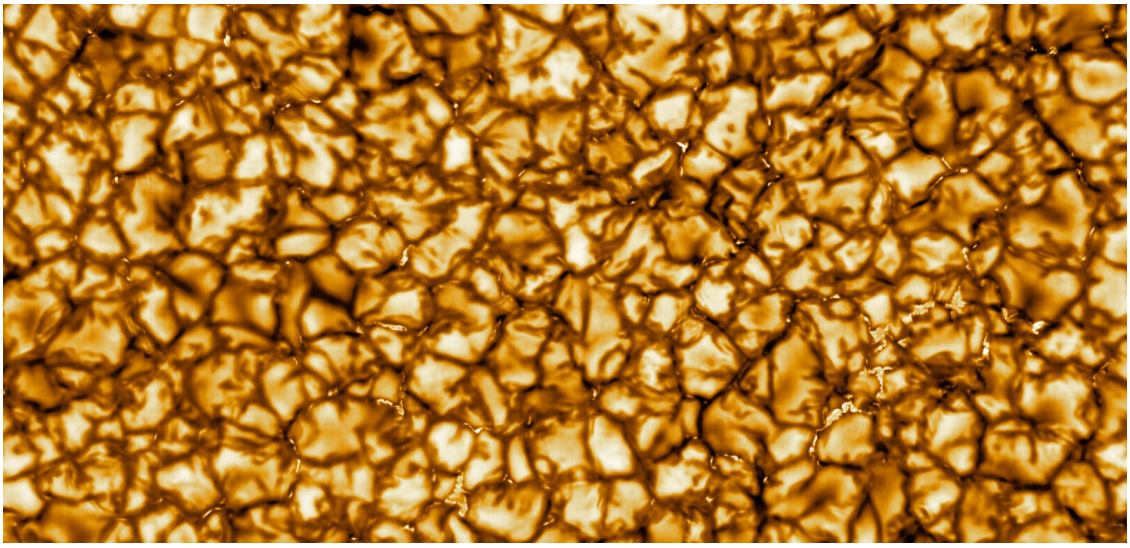

Figure 1.2: First light image of photospheric granulation obtained using DKIST, with resolved features as small as 30 km. Each 'cell' corresponds to a granule where hotter (brighter) material rises in the center and cooler (darker) material sinks in the dark lanes. Image credit: NSO/AURA/NSF, `https://nso.edu/telescopes/dkist/first-light-full-image/`

given the harsh physical conditions on the Sun, it is impossible to do so. Parker Solar Probe [33] aims to get within 10 solar radii (0.046 AU) of the Sun but direct measurements of the deep solar atmosphere, such as the lower corona, chromosphere and photosphere, are not possible. One thus has to rely on indirect methods to infer Sun's physical properties. A general class of such problems is called an 'inverse problem' where one aims to indirectly infer the properties of a system from its measured response (or observations obtained from the system). For example, in helioseismology one aims to infer the internal structure of the Sun using the oscillations seen on the solar surface, in geoseismology one aims to infer the properties of the interior of the Earth using surface wave observations, etc. The opposite of an inverse problem is called the 'forward problem' where one aims to determine the physical output signal given a known model that describes the working of the physical system (see Figure 1.3). The focus of this thesis is to infer the atmospheric parameters corresponding to the deepest layer of the solar atmosphere (solar photosphere) from measurements of electromagnetic spectra.

Solar photosphere is about 500 km thick and corresponds to the 'visible surface' of the Sun,

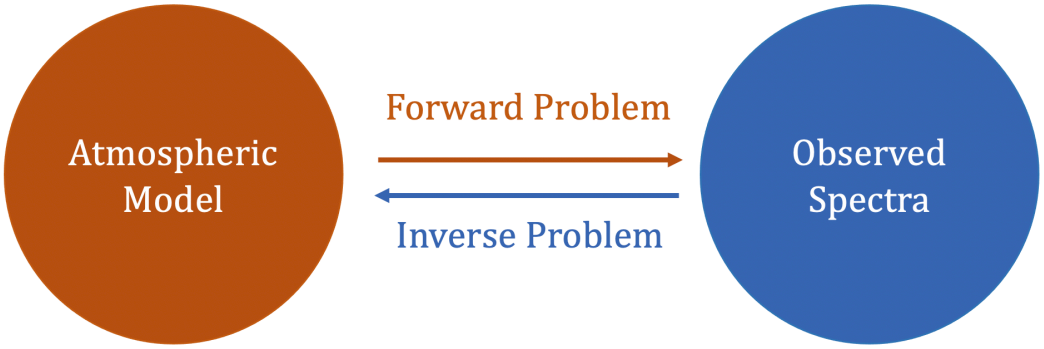

Figure 1.3: Graphical representation of the forward and inverse problem.

where the atmospheric conditions allow the visible light to escape from the solar interior. In this layer, temperature (and density) decreases with height. A one-dimensional, semi-empirical VAL atmospheric model [1, 49] is shown in Figure 1.4, where we plot the temperature (and density) as a function of height. The model corresponds to an average stratification and does not capture the in-homogeneous, dynamic and intermittent nature of the solar atmosphere. We use solar spectropolarimetric measurements to infer the atmospheric properties. This is possible because as radiation travels through the solar atmosphere, it interacts with the medium and is subject to absorption, emission and scattering processes. These interactions leave signatures in the spectra, which we can invert for the physical properties of the atmosphere. Further, different parts (wavelengths) of a spectral line are sensitive to different layers of the solar atmosphere (line-core region of a spectral line is more sensitive to the upper layers of the solar atmosphere, while the line-wing (continuum) is more sensitive to the deeper layers), and, different spectral lines themselves can be sensitive to different regions of the solar atmosphere. This is demonstrated in Figure 1.5 where we plot the spectra for visible and infrared lines (≈ 1.5 μm). The continuum wavelengths near the 1.5 μm lines are sensitive to deeper, hotter layers, and thus have relatively larger intensities, as compared to the visible spectra. This variable sensitivity of different spectral regions to different atmospheric depths is also demonstrated in Figure 1.6 which shows how Sun 'appears' in different wavelength

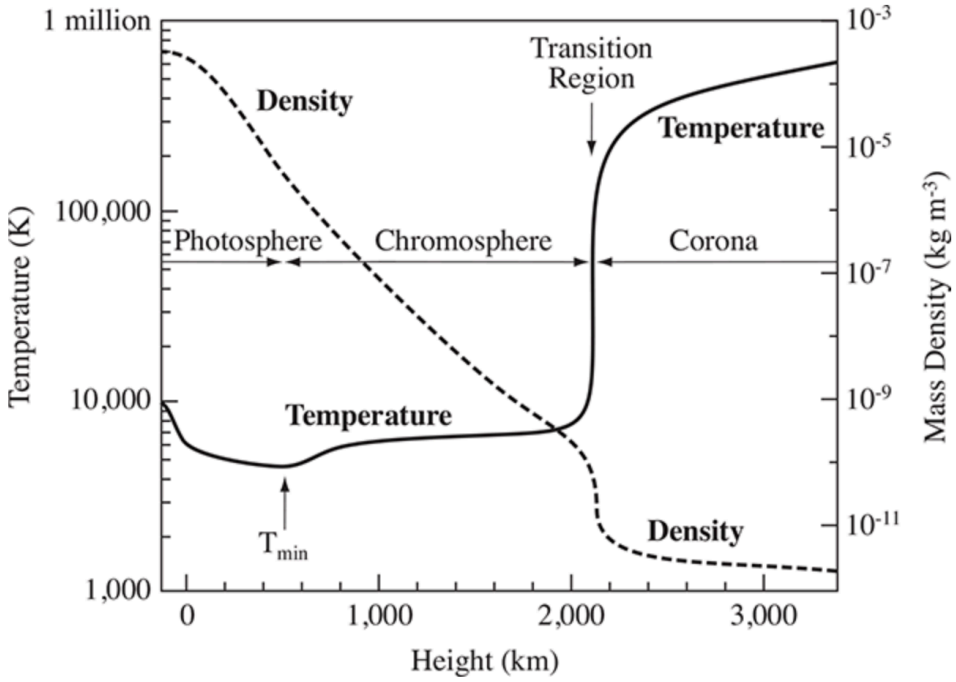

Figure 1.4: The temperature and mass density stratification for the 1-D semi-empirical quiet-Sun VAL model. The model corresponds to an average stratification of the given parameters and do not capture the dynamic and intermittent nature of the solar atmosphere.

channels on the Solar Dynamics Observatory [45]. Here the atmosphere above the photosphere is being observed rather than the deep photosphere, as was the case for 1.5 μm.

In summary, we usually require a combination of multiple spectral lines with differential sensitivity to variables and depths in order to achieve a 'good' inversion result. The quality of inversion depends on the quality of the spectral data, assessed based on the noise level, spectral, spatial and temporal resolution, and the 'amount' of orthogonal sensitivity to different variables and depths.

1.2 DKIST - A new era of solar physics measurements

The Daniel K. Inouye Solar Telescope (DKIST) [53] is the upcoming 4-meter solar telescope, nearing completion on Haleakala, Maui, which will allow us to make multi-line observations at unprecedented spectral, spatial and temporal resolution. It has an off-axis, clear aperture design

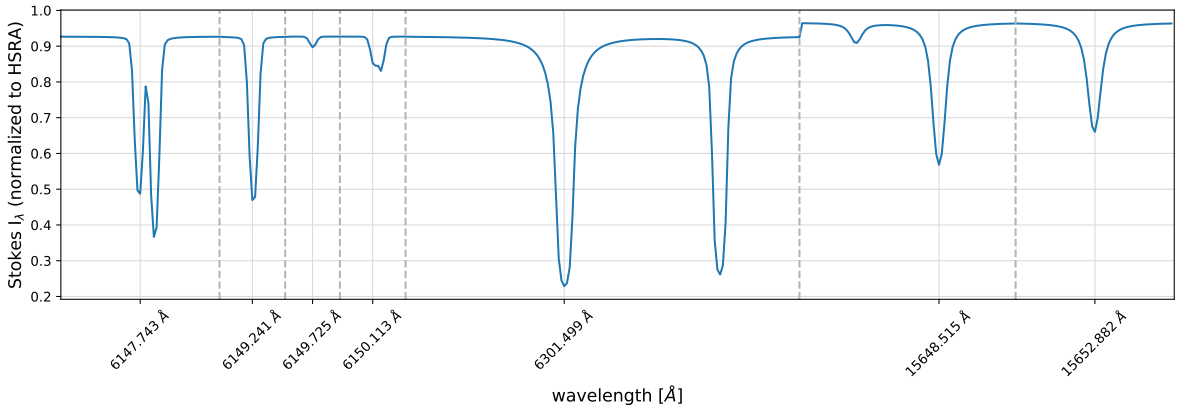

Figure 1.5: Synthetic spectra (Stokes I, normalized to HSRA intensity [18]) through the mean MURaM atmosphere, synthesized using SIR forward solver, for the spectral lines mentioned in Table A.1.

which prevents the secondary optical elements from obstructing the primary aperture, thus minimizing scattered light in the process. The aperture size of 4-meters is the world's largest for a solar telescope and will allow us to resolve features smaller than $\approx$ 25 km (at 500 nm) in the solar photosphere. An example first light image of the solar granulation from DKIST is shown in Figure 1.2. The large aperture size means that a short integration time is required to achieve a high signal-to-noise, high resolution measurements at high cadences. The telescope will have a polarization accuracy of 10^{-4} allowing precise measurements of the weak magnetic fields in the solar photosphere. The telescope's five instrument suite will allow observations of the Sun over a wide wavelength range, 300 nm to 35 μm, giving us the diagnostic ability to constrain the atmospheric properties from the photosphere to corona.

This multi-line, multi-height observational capability at unprecedented spatial resolution (and high signal-to-noise) will allow us to answer many outstanding questions in the community e.g. how small-scale photospheric magnetic fields are created and destroyed, what leads to the heating of the outer layers of the solar atmosphere to over 1 MK temperatures, etc. For a more exhaustive list of projects possible with DKIST, see [50].

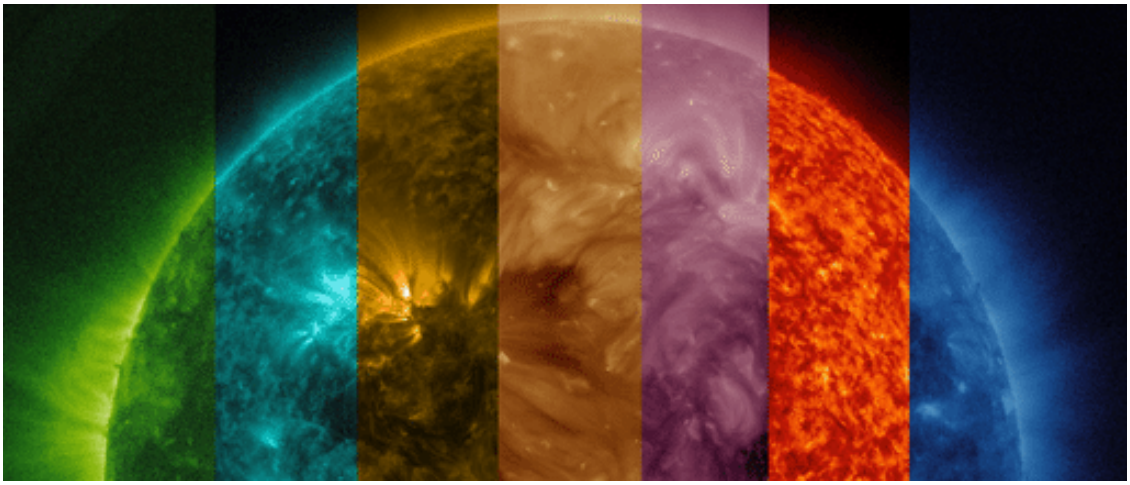

Figure 1.6: Sun as it appears in different SDO wavelength channels (false colors). The wavelengths sample drastically different atmospheric layers. Image credit: SDO/NASA.

1.3 Relevance of this work and thesis structure

While great effort has been put into improving the quality of observations, the quality of inverse solutions are dictated by the inversion method employed. In particular, the horizontal resolution of inversions is determined by the observational resolution while the vertical resolution is determined by the inversion method itself. Given the inherent underdetermined nature of the inverse problems, inverse solutions are often unrealistically oscillatory with depth. In order to achieve physically meaningful solutions, current state of the art inversion methods (e.g. SIR) manually force a globally smooth solution, putting a limit to its vertical resolution, i.e. SIR inversions typically have a vertical resolution of $\approx$ 50 km at best. In MURaM simulations of the solar photosphere, we find sharp gradients with depth in the atmospheric variables at spatial scales much smaller than that could be resolved using the SIR method. Moreover, SIR solutions likely do not capture the 'true resolution limit' achievable given the spectral data. To use the DKIST telescope at its full potential and to recover these gradients as best as possible, it is critical to obtain the solutions that are at resolution limit achievable given the spectral data available.

In this work, for the first time, we apply the Optimally Localized Averages (OLA) method

to invert solar spectroscopic data to achieve this goal. The method was previously developed for geoseismology and helioseismology to invert for the internal properties of the Earth and Sun, respectively. It is fundamentally different from SIR as it aims to find the most vertically localized solution possible at each depth. This inversion resolution limit achievable is mostly determined by the sensitivity of spectra to different variables and depths, and the observational noise.

In spite of the several advantages over the SIR method, the original OLA method has its own set of disadvantages and limitations when applied to spectroscopic data. In the next Chapter 2, we discuss those challenges faced and develop methods needed to obtain reliable inversions. We limit ourselves to inverting only for the thermodynamic properties of the solar photosphere i.e. temperature T, electronic pressure P_e and line-of-sight velocity V_{los}. Inverting for magnetic field vector remains for the future.

In Chapter 2 we briefly describe the fundamental ingredients and equations involved when carrying out inversions in general. We further discuss inversions within the SIR framework and those used in helioseismology. We describe the basic methodology of OLA, challenges faced when applying it to spectroscopic data, and changes made to mitigate those issue. For simplicity, here we limit ourselves to single variable inversions for artificial test cases. In Chapter 3, we apply the modified single variable OLA approach to invert MURaM atmospheres, statistically assess its inversion capability and compare it to the results obtained from SIR. In Chapter 4, we extend the modified OLA method to multivariable inversion of thermodynamic parameters. In Chapter 5 we discuss the caveats of having redundant response functions in the response function matrix and improvement in the quality of inversion solution when these redundancies are removed. We also discuss a potential way to quantitatively assess the inversion potential of different line combinations using the slope of the singular value curve. We finally conclude this thesis with Chapter 6 where we summarize the work and discuss the unresolved issues pertaining to the modified OLA approach and possible ways to mitigate them in the future.

In Appendix A we briefly discuss the theory of radiative transfer which describes the light-

matter interaction and the theory behind the formation of spectral lines. In Appendix B we mention the SIR node values employed for different cases.

Chapter 2

OLA single variable inversion

In this chapter, we start with a brief discussion of the general approach to spectroscopic inversions and later discuss the application of the OLA method and meeting the challenges faced when applying it in the spectroscopic context. Here, to introduce the concept, and for simplicity, the discussions would be limited to inverting temperature $\mathbf{T}$ only, using the 'observed' spectroscopic intensity data (Stokes $\mathbf{I}$). More realistic multivariable inversions will be discussed in Chapter 4. Here bold letters correspond to mathematical vectors (or matrices) e.g. $\mathbf{I}$ represents a vector of intensity spectra over multiple wavelengths, and $\mathbf{T}$ represents a vector of temperature over multiple optical depths.

2.1 Brief introduction to inversions

In general, spectropolarimetric inversions are carried out by starting with an initial guess for $\mathbf{T}$ (depth dependent quantity) and solving for the underlying difference $\Delta\mathbf{T}$ between the actual and guess $\mathbf{T}$ that accounts for the spectral difference $\Delta\mathbf{I}$ between the observed spectra and that derived from the guess model. When inversion is complete, the spectra from the updated (inverted) model, given by guess $\mathbf{T}+\Delta\mathbf{T}$, is 'as close as possible' to the observed spectra $\mathbf{I}$. An example test case is shown in the top plot in Figure 2.1, where the actual (underlying, observed) $\mathbf{T}$ is shown as gray-dashed curve, guess $\mathbf{T}$ as red-dashed curve and the difference $\Delta\mathbf{T}$ between them as red solid curve. In reality, actual $\mathbf{T}$, and thus the difference $\Delta\mathbf{T}$, are unknown. This $\Delta\mathbf{T}$ is what the inversion aims to capture.

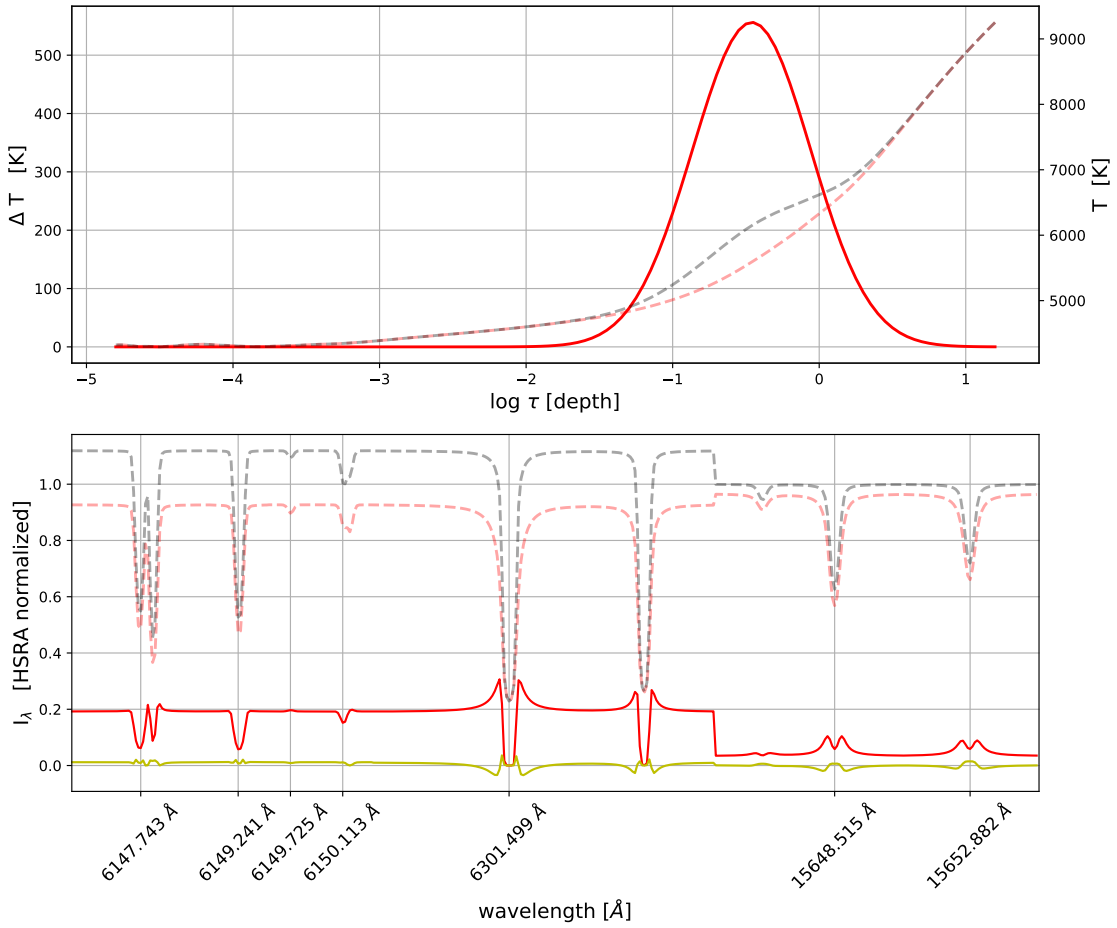

Figure 2.1: (Top plot) Mean MURaM guess $\mathbf{T}$ is shown in red-dashed, actual $\mathbf{T}$ is shown in gray-dashed and is artificially constructed by adding Gaussian-shaped perturbation $\Delta\mathbf{T}$ (red-solid) peaked at $\log\,\tau = -0.50$ (width = 0.40 $\Delta\log\,\tau$, perturbation amplitude = 10%) to the mean MURaM guess $\mathbf{T}$. Note that τ here corresponds to optical depth at 500 nm. (Bottom plot) Spectra synthesized using SIR for the mean MURaM model is shown by red-dashed curve, for artificial $\mathbf{T}$ is shown by gray-dashed curve and the difference between the two i.e. $\Delta\mathbf{I}$ = actual - guess $\mathbf{I}$, is shown in red-solid curve. Overplotted in yellow is the error from the higher order terms ($\Delta\mathbf{I} - \mathbf{R}_\mathrm{T}{}^\top \bullet \frac{\Delta\mathbf{T}}{\mathbf{T}}$).

2.1.1 Response functions and the 1st order linear system of equations

The relationship between $\Delta\mathbf{I}$ and $\Delta\mathbf{T}$ is described by linear response functions which define the sensitivity (response) of spectra to a small change in the variable at a given optical depth. These response functions depend on the underlying atmosphere being perturbed. The linear response of the spectrum at a given wavelength $\delta\mathrm{I}(\lambda)$ to a small amplitude temperature perturbation at an

optical depth τ defines the temperature response function,

$$\mathrm{R}'_{\mathrm{T}}(\tau,\lambda) \quad = \quad \frac{\delta \mathrm{I}(\lambda)}{\delta \mathrm{T}(\tau)} \tag{2.1}$$

In integral form, it can be rewritten as

$$\mathbf{R}'^{\top}_{\mathrm{T}}(\lambda) \cdot \delta\mathbf{T} \quad = \quad \delta \mathrm{I}(\lambda) \tag{2.2}$$

which states that the total change in intensity δI at a given wavelength λ is equal to the sum of the change in temperature $\delta\mathbf{T}$ at each depth location weighted by the corresponding response function (or sensitivity factors) at that wavelength.

Response functions are computed analytically ([16, 35, 54, 55]) for all optical depths τ and all wavelengths λ under consideration, given the underlying atmosphere. For a set of wavelengths, Equation 2.2 can be written in the matrix form as

$$\mathbf{R}'^{\top}_{\mathrm{T}} \cdot \delta\mathbf{T} \quad = \quad \delta\mathbf{I} \tag{2.3}$$

We note that, unlike the most other inversion methods we employ fractional response functions $\mathbf{R}_{\mathrm{T}}$ which are equal to the ratio of change in intensity at a given wavelength to the fractional change in temperature at a given depth location. With this definition, Equation 2.3 becomes

$$\mathbf{R}^{\top}_{\mathrm{T}} \cdot \frac{\delta\mathbf{T}}{\mathbf{T}} \quad = \quad \delta\mathbf{I} \tag{2.4}$$

This use of fractional response functions removes the dimensional dependency of the spectral sensitivity to change in a given variable, facilitating comparison of the response function magnitudes between variables. Note that for $\mathbf{T}$ (and $\mathbf{V_{los}}$), fractional and dimensional response functions are quite similar (see Figure 2.2) and produce very similar inversion results. This is because these variables don't vary significantly over photospheric depths (variation is of the order of a few multiples, see $\mathbf{T}$ in Figure 2.1) and given that $\mathrm{R}_{\mathrm{T}}(\tau,\lambda) = \mathrm{T}(\tau) \times \mathrm{R}'_{\mathrm{T}}(\tau,\lambda)$, $\mathbf{R}_{\mathrm{T}}$ is approximately a constant factor re-scaled version of $\mathbf{R}'_{\mathrm{T}}$. However, this is not the case with $\mathbf{P_e}$ which varies by a few orders of magnitude over the relevant depths resulting in a significant difference in the shape

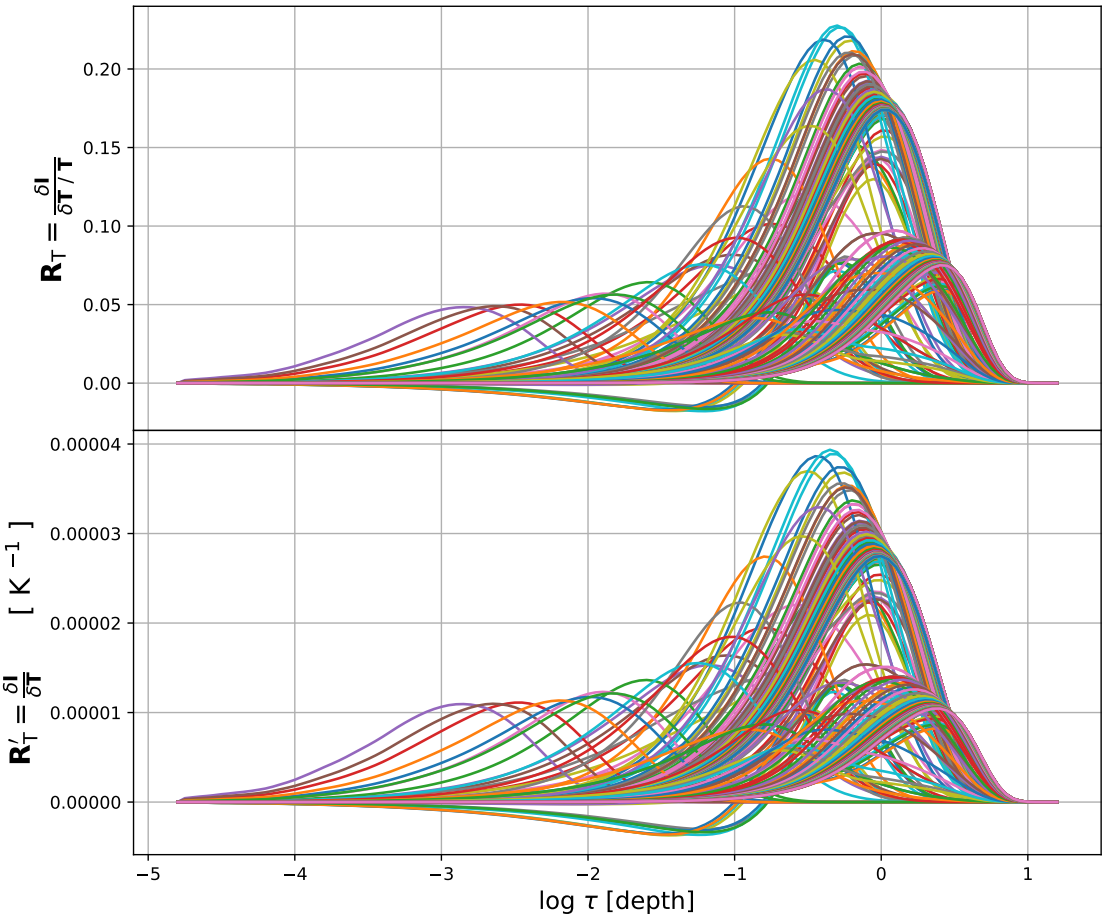

Figure 2.2: (top-plot) Fractional response functions $\mathbf{R}_\mathrm{T}$ computed using SIR (for mean MURaM model), for spectral lines mentioned in Table A.1. Each line curve corresponds to the response function for a given wavelength. (bottom-plot) Corresponding dimensional response functions $\mathbf{R}'_\mathrm{T}$. The dimensional and fractional response functions are related by $\mathrm{R_T}(\tau, \lambda) = \mathrm{T}(\tau) \times \mathrm{R'_T}(\tau, \lambda)$.

of the dimensional and fractional response functions (see Figure 3.6). Because of this, it is very difficult to invert for $\mathbf{P_e}$ using dimensional response functions (see Section 3.3.3 for details).

The fractional response functions for temperature $\mathbf{R}_\mathrm{T}$ establishes the linear relationship between the observed $\mathbf{\Delta I}$ and the desired $\frac{\mathbf{\Delta T}}{\mathbf{T}}$ that inversion aims to determine. Discretized in optical depth and wavelength, the relationship can be written as a system of linear equations (the 1st order equation),

$$\mathbf{\Delta I} \;=\; \mathbf{R}_\mathrm{T}^{\top} \cdot \frac{\mathbf{\Delta T}}{\mathbf{T}} \;+\; \boldsymbol{\varepsilon} \tag{2.5}$$

This system of equations can be derived by minimizing a merit function which is the sum of the squared differences between the observed and the guess-model spectra (see [16, page 201]). Here $\boldsymbol{\varepsilon}$ indicates error, resulting from the observational and instrumental errors, such as noise in observed intensities (real world scenario), as well as the higher order terms omitted by the linear approximation to the response function. When the guess-model is not close to the observed atmosphere, $\frac{\boldsymbol{\Delta T}}{\mathbf{T}}$ is not small, and the relationship between $\boldsymbol{\Delta I}$ and $\frac{\boldsymbol{\Delta T}}{\mathbf{T}}$ is no longer linear. Under these conditions the missing higher order terms (order $\left(\frac{\boldsymbol{\Delta T}}{\mathbf{T}}\right)^2$ and higher) contribute significantly to $\boldsymbol{\varepsilon}$. The 'observed' spectra (gray-dashed) and their differences $\boldsymbol{\Delta I}$ (red) as a function of wavelength for the test case mentioned above is plotted in Figure 2.1 (bottom plot). Also depicted with the yellow curve is the value of the higher order response function truncation error, given by $\boldsymbol{\Delta I} - \mathbf{R}_{\mathrm{T}}{}^{\top} \bullet \frac{\boldsymbol{\Delta T}}{\mathbf{T}}$, as observed $\mathbf{I}$ has no spectral noise contribution. Additional errors such as that due to discretization (from solving the radiative transfer equation on a grid) or numerical round-off are usually much smaller. In this section, error $\boldsymbol{\varepsilon}$ represents the missing higher order sensitivities only. The effect of observational errors on the inversion quality is discussed in Section 2.2.7.

2.1.2 Solving 1st order system of equations

Solving Equation 2.5, a linear system of equations, requires computing the inverse of the $\mathbf{R}_{\mathrm{T}}^{\top}$ matrix. This is a non-trivial task as the system of equations belongs to the ill-posed category, as evident from the exponential decay of the singular values of the $\mathbf{R}_{\mathrm{T}}^{\top}$ matrix to smaller values (see Section 2.2.1 for more details). This combined with the fact that the system of equations is not perfect (non-zero error $\boldsymbol{\varepsilon}$), means that the upper limit to the number of linearly independent equations 'that can be employed' (when computing matrix inverse) is much smaller than the total number of variables in Equation 2.5. Thus the system of equations is 'effectively' underdetermined and one 'cannot' uniquely solve for $\frac{\boldsymbol{\Delta T}}{\mathbf{T}}$. Physically, this is due to redundancy in the spectral line formation. Different wavelengths within different spectral lines have 'similarly shaped' response functions. Further, given that radiative transfer is an averaging (smoothing) process, detailed information about the atmosphere (sharp gradients in model properties) is lost in the process of

line formation. Thus, there is a limit to how well the underlying atmosphere can be recovered.

Mathematically, the ill-posed nature of the equations means that the numerical rank of the $\mathbf{R}_{\mathrm{T}}^{\top}$ matrix is ill-determined. Naively computing its *pseudo-inverse* (e.g. using normal equations approach) will likely result in an inverse matrix with large amplitude terms which can amplify error $\boldsymbol{\varepsilon}$ and result in an error dominated solution. Error dominated solutions are generally highly oscillatory with depth and lack physical significance (see Section 2.2.3 for further details).

In order to obtain a physically meaningful solution that is not dominated by error, some sort of regularization (smoothing) is employed. Mathematically, regularization removes the contribution of smaller singular values when computing *pseudo-inverse* matrix, as it is these smaller singular values that appear in the denominator and result in high amplitude terms in the *pseudo-inverse* matrix. The inversion solution depends heavily on the 'amount' of regularization. A strongly regularized solution corresponds to a smoother solution which might fail to capture the gradients in the underlying $\frac{\boldsymbol{\Delta}\mathbf{T}}{\mathbf{T}}$. Weak regularization can result in an inversion solution that is closer to the actual $\frac{\boldsymbol{\Delta}\mathbf{T}}{\mathbf{T}}$, but has a higher chance of being error dominated. Determining how to 'effectively' regularize (balance resolution and error amplification) is one of the hardest problems when doing inversions. In the next section, we briefly discuss inversion methods currently used in spectropolarimetry (SIR) and helioseismology (RLS) and how they obtain physically meaningful solutions, before moving on to the application of the helioseismic OLA method to spectroscopic data.

2.1.3 SIR inversion method

Current state of the art spectropolarimetric inversion code, SIR [15, 16, 17, 54], obtains a smooth solution by solving for $\boldsymbol{\Delta}\mathbf{T}$ at a limited number of user-defined locations called 'nodes'. The $\boldsymbol{\Delta}\mathbf{T}$ value for other depth points are then interpolated from these nodal values. Thus, by design, this method ensures that the inverted solution is non-oscillatory over nodal scales. Please note that, for consistency, we use the notation $\frac{\boldsymbol{\Delta}\mathbf{T}}{\mathbf{T}}$, though in reality SIR directly inverts for $\boldsymbol{\Delta}\mathbf{T}$.

Conceptually, SIR method can be understood in terms of solving a modified version of Equa-

tion 2.5:

$$\Delta\mathbf{I} \;=\; \mathbf{R}_{\mathrm{T}}^{\top}\cdot\mathbf{F}\cdot\mathbf{F}^{-1}\cdot\frac{\Delta\mathbf{T}}{\mathbf{T}} \;+\; \boldsymbol{\varepsilon} \tag{2.6}$$

where, matrix $\mathbf{F}$ contains the interpolation factors and is used to compute the response function values to node locations ($\mathbf{R}_{\mathrm{T}}^{\top}\cdot\mathbf{F}$). SIR inverts $\mathbf{R}_{\mathrm{T}}^{\top}\cdot\mathbf{F}$, and given that the number of depth points is reduced to the number of nodes, is essentially solving an overdetermined version of Equation 2.5. This indirectly removes the smaller singular values inherent in $\mathbf{R}_{\mathrm{T}}$ matrix and, by design, doesn't allow solutions to have spatial frequency larger than that allowed by the number of nodes. While $(\mathbf{R}_{\mathrm{T}}^{\top}\cdot\mathbf{F})^{-1}\cdot\Delta\mathbf{I}$ correspond to the inversion values at node locations, the final inversion solution at all depths is given by $\mathbf{F}\cdot(\mathbf{R}_{\mathrm{T}}^{\top}\cdot\mathbf{F})^{-1}\cdot\Delta\mathbf{I}$.

2.1.4 Regularized Least Squares (RLS) inversion method

In Regularized Least Squares method (RLS) of helioseismology [9, 10, 11, 27, 31], as applied to spectropolarimetry, $\frac{\Delta\mathbf{T}}{\mathbf{T}}$ is determined at all depths to best satisfy Equation 2.5, along with an additional constraint that acts as a smoothing/regularization term. Mathematically, RLS inverted solution is obtained by minimizing

$$\chi^2_{reg} \;=\; \left\|\Delta\mathbf{I}-\mathbf{R}_{\mathrm{T}}^{\top}\cdot\frac{\Delta\mathbf{T}}{\mathbf{T}}\right\|_2^2+\;\xi^2\left\|\frac{\Delta\mathbf{T}}{\mathbf{T}}\right\|_2^2 \tag{2.7}$$

where, ξ is a user-defined 'trade-off' parameter. The first term on the right hand side corresponds to the square of the residual, while the second term is the added constraint, which in this example is taken to be the square of the L2 norm of the obtained solution (one of many possible constraint choices). Note that unlike Equation 2.5, error $\boldsymbol{\varepsilon}$ here is not explicitly mentioned, but is implicit. Minimizing χ^2_{reg} in Equation 2.7, with respect to $\frac{\Delta\mathbf{T}}{\mathbf{T}}$, yields the following linear system of equations:

$$\begin{pmatrix}\Delta\mathbf{I}\\ 0\end{pmatrix} \;=\; \begin{pmatrix}\Delta\mathbf{R}_{\mathrm{T}}^{\top}\\ \xi\, I\end{pmatrix}\cdot\frac{\Delta\mathbf{T}}{\mathbf{T}} \tag{2.8}$$

where, I is an identity matrix.

The idea behind adding a smoothing constraint is to improve the overall ill-posedness of the system of equations. The trade-off parameter ξ determines the relative sensitivity with which

$\Delta\mathbf{I} = \mathbf{R}_{\mathrm{T}}^{\top} \cdot \frac{\Delta\mathbf{T}}{\mathbf{T}}$ and $I \cdot \frac{\Delta\mathbf{T}}{\mathbf{T}} = 0$ are solved. A larger value for ξ results in solutions which satisfies $I \cdot \frac{\Delta\mathbf{T}}{\mathbf{T}} = 0$ (a well-posed system) more strongly than $\Delta\mathbf{I} = \mathbf{R}_{\mathrm{T}}^{\top} \cdot \frac{\Delta\mathbf{T}}{\mathbf{T}}$. Mathematically, this removes contributions of smaller singular values when computing the *pseudo-inverse* matrix and thus results in a smoother inversion solution. A smaller value for ξ, on the other hand, results in solutions more prone to satisfying the ill-posed system $\Delta\mathbf{I} = \mathbf{R}_{\mathrm{T}}^{\top} \cdot \frac{\Delta\mathbf{T}}{\mathbf{T}}$, with the *pseudo-inverse* matrix having contributions from smaller singular values. If ξ is taken too small this results in an error dominated oscillatory solution.

2.1.5 Need for OLA inversion method

SIR and RLS methods are similar in the sense that they both intend to obtain a globally smooth solution. Their limitation is that the inverted solutions may not be the best localized solution that can be obtained at each depth given the spectra. It is very hard for these approaches to recover steep gradients in the underlying $\frac{\Delta\mathbf{T}}{\mathbf{T}}$ (or $\Delta\mathbf{T}$), or a priori know what gradients are recoverable. The depth resolution of the inversion depends on the user choice of the number of nodes (or the value of ξ), and may not be representative of the 'true' resolution achievable given the data. Determining what the maximum achievable depth resolution is and inverting at that resolution is critical to using the upcoming DKIST telescope at its full potential. Further, solutions obtained using SIR/RLS method suffer from cross-talk error from $\frac{\Delta\mathbf{T}}{\mathbf{T}}$ corresponding to other depths (and other variables, in a multivariable system), especially in the region with lesser orthogonal sensitivities in the $\mathbf{R}_{\mathrm{T}}$ matrix.

Goal of this thesis is to employ the OLA inversion method to invert spectroscopic data. The method is fundamentally different from SIR/RLS. It aims to obtain inversion solutions that are 'optimally' localized at each depth, given the spectra, with minimal cross-talk error contribution from perturbations from other depths (within the same variable) and from other variables. The method has origins in geoseismology [2, 3, 4] and was later adopted by helioseismologists [5, 10, 11, 20, 21, 29, 46, 47] to infer the internal properties of the Sun. In the next section, we describe this inversion method in context of spectroscopic inversions.

2.2 OLA inversion: Methodology

In this section we describe the OLA inversion method in the context of inverting temperature $\mathbf{T}$ using spectroscopic intensity data (Stokes $\mathbf{I}$). To introduce the method, we first examine single-variable inversions for artificial temperature perturbations. For these test cases, we use the horizontal mean state of a MURaM simulation (see Section 3.1 for details) as the initial guess-model atmosphere and add a height dependent temperature perturbations to mimic possible variations. We can then, starting with the mean model as the initial guess, conduct OLA inversion for $\mathbf{T}$ and compare the results with those of the perturbed (actual, underlying, observed) atmosphere, which in these test cases, but not in real observations, is known. This allows the assessment of the capabilities and limits of the method and the presentation of the advancements to the OLA method that are necessary in the spectropolarimetric context compared to its application in helioseismic inversions.

An example test case is shown in the top-panel in Figure 2.1. In that figure, the red-dashed curve corresponds to the initial guess model (the mean MURaM simulation), the gray-dashed curve corresponds to the artificially constructed observed atmosphere and red-solid line corresponds to the difference between observed and guess-model, $\Delta\mathbf{T}$. Since this discussion is focused on inverting the spectral data for $\mathbf{T}$ in the absence of cross-term variables, no perturbations are added to $\mathbf{P_e}$ and $\mathbf{V_{los}}$, i.e., $\Delta\mathbf{P_e}$ and $\Delta\mathbf{V_{los}}$ are taken to be zero.

Test of the OLA spectral-inversion technique proceeds as follows: Using the forward spectral synthesis capabilities of SIR, we compute the synthetic spectra (see Figure 2.1, bottom plot) for the observed and the guess-model, and at the same time the fractional spectral response function matrix $\mathbf{R}_{\mathrm{T}}$ at these observed wavelengths for the initial guess-model (see Figure 2.2, top plot). The computed response functions, along with the spectral difference between observed and guess spectra $\Delta\mathbf{I}$, define the 1st order linear system of Equations 2.5, which must be solved for $\frac{\Delta\mathbf{T}}{\mathbf{T}}$, and from this the inverted temperature profile is determined. It can then be compared to the input (underlying) atmosphere for accuracy and reliability.

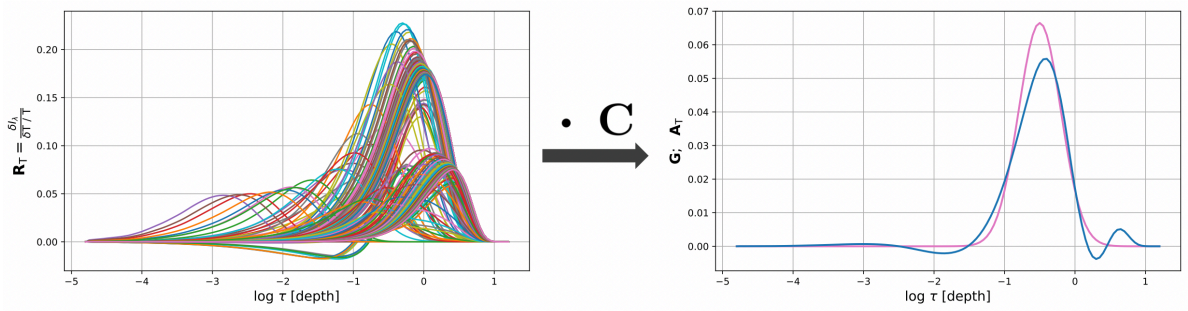

Figure 2.3: Graphical representation of Equation 2.9. $\mathbf{R}_\mathrm{T}$ is shown in the left plot, while $\mathbf{G}$ (pink) and $\mathbf{A}_\mathrm{T}$ (blue) are shown on the right plot. Here we aim to compute coefficients $\mathbf{C}$ such that $\mathbf{R}_\mathrm{T} \cdot \mathbf{C} = \mathbf{A}_\mathrm{T} \approx \mathbf{G}$. We computed *pseudo-inverse* of $\mathbf{R}_\mathrm{T}$ matrix with rank $k = 5$ (based on dominant singular values that add up to 95% of the total sum).

2.2.1 OLA method: Averaging kernels

As already mentioned in Section 2.1.2, inversion problems are inherently ill-posed and some sort of regularization is required to obtain a physically meaningful solution. Techniques such as SIR/RLS aim to find an overall smooth solution that best fits the observed spectra by solving for $\Delta\mathbf{T}$ at all depths (or nodes) simultaneously. The OLA method, on the other hand, aims to invert for $\Delta\mathbf{T}$ at one depth location τ_i at a time. The intention is to find the 'best possible' inversion at each location, with inversion regularization criteria not based on a global smoothness measure, but on how well localized (spatially/depth averaged) the solution is at each depth (minimal cross-talk error from other depths).

A localized inversion solution at a target depth τ_i is obtained by linearly combining the response functions vectors to form an averaging kernel $\mathbf{A}_\mathrm{T}(\tau_i)$ with the help of linear coefficient vector $\mathbf{C}$ ($[\mathrm{c}_{\lambda_1}, \mathrm{c}_{\lambda_2}, \mathrm{c}_{\lambda_3}, ...]^\top$). These coefficients are then used with $\Delta\mathbf{I}$ to obtain an inverted solution at depth τ_i. The averaging kernel $\mathbf{A}_\mathrm{T}(\tau_i) = \mathbf{R}_\mathrm{T} \cdot \mathbf{C}$ is obtained by solving the following linear system of equations:

$$\mathbf{R}_\mathrm{T} \cdot \mathbf{C} \quad = \quad \mathbf{G}(\tau_i, \sigma) \ , \tag{2.9}$$

where $\mathbf{G}$ is a user-defined target function localized around the inversion target depth τ_i. It is usually

taken to be a normalized Gaussian, with peak at τ_i and standard deviation (width) σ. An example is shown in Figure 2.3. Plotted on the left side of the figure are individual response functions for all observed wavelengths, and on the right, the target function (pink) and averaging kernel (blue) obtained by their linear combination. As will be explained further below, since Equation 2.9 can only be approximately solved, $\mathbf{A}_{\mathrm{T}}$ only approximates $\mathbf{G}$.

Once computed, the coefficients $\mathbf{C}$ can be used to obtain the inverted solution. Taking the dot product of Equation 2.5 with $\mathbf{C}^{\top}$ and recognizing $\mathbf{R}_{\mathrm{T}} \cdot \mathbf{C}$ as the averaging kernel yields

$$\mathbf{C}^{\top} \cdot \boldsymbol{\Delta}\mathbf{I} \;=\; \mathbf{A}_{\mathrm{T}}^{\top}(\tau_i) \cdot \frac{\boldsymbol{\Delta}\mathbf{T}}{\mathbf{T}} \;+\; \mathbf{C}^{\top} \cdot \boldsymbol{\varepsilon} \tag{2.10}$$

Here, $\mathbf{C}^{\top} \cdot \boldsymbol{\Delta}\mathbf{I}$ is the inversion solution at τ_i which, if the error contribution ($\mathbf{C}^{\top} \cdot \boldsymbol{\varepsilon}$) is small, corresponds to an optical depth averaged value of $\frac{\Delta \mathbf{T}}{\mathbf{T}}$, defined as $\left\langle \frac{\Delta \mathrm{T}}{\mathrm{T}}(\tau_i) \right\rangle \equiv \mathbf{A}_{\mathrm{T}}^{\top}(\tau_i) \cdot \frac{\Delta \mathbf{T}}{\mathbf{T}}$. Finally, inverted $\Delta \mathrm{T}(\tau_i)$ at location τ_i is given by $\mathrm{T}(\tau_i) \times (\mathbf{C}^{\top} \cdot \boldsymbol{\Delta}\mathbf{I}) \approx \mathrm{T}(\tau_i) \times \left\langle \frac{\Delta \mathrm{T}}{\mathrm{T}}(\tau_i) \right\rangle$. A narrower width averaging kernel yields less averaging with $\left\langle \frac{\Delta \mathrm{T}}{\mathrm{T}}(\tau_i) \right\rangle$ closer to the underlying $\frac{\Delta \mathrm{T}}{\mathrm{T}}(\tau_i)$; if a δ-function averaging kernel could be constructed, then $\left\langle \frac{\Delta \mathrm{T}}{\mathrm{T}}(\tau_i) \right\rangle \equiv \frac{\Delta \mathrm{T}}{\mathrm{T}}(\tau_i)$. This is typically not possible. For a given finite set of response functions, the inherent ill-posed nature of the Equation 2.9 limits the minimum target function width that can be reasonably fit by the averaging kernel. Additionally, 'successfully' constructing narrower averaging kernels comes with the cost of larger coefficient amplitudes which amplify the error $\boldsymbol{\varepsilon}$ through $\mathbf{C}^{\top} \cdot \boldsymbol{\varepsilon}$ in Equation 2.10 and can lead to an inverted solution $\mathbf{C}^{\top} \cdot \boldsymbol{\Delta}\mathbf{I}$ that is error dominated.

To understand this further, it helps to see how Equation 2.9 is solved for coefficients $\mathbf{C}$. Lets say we want to construct an averaging kernel at depth $\log \tau_i = -0.5$, with a width of 0.4 (in $\Delta \log \tau$ units), and we define the target function $\mathbf{G}$ accordingly. To solve for $\mathbf{C}$, we first need to compute the inverse of the response function matrix $\mathbf{R}_{\mathrm{T}}$. That matrix is usually non-invertible, and we have to computed a generalized inverse (*pseudo-inverse* or approximate inverse, [6, 19, 27, 48]) of the matrix. One approach is to utilize the singular value decomposition (SVD, [27, 28, 48, 61, 62]) of the $\mathbf{R}_{\mathrm{T}}$ matrix, given by

$$\mathbf{R}_{\mathrm{T}} \;=\; \mathbf{U}\,\mathbf{S}\,\mathbf{V}^{\top} \;=\; \sum_{i=1}^{r} (\mathbf{u}_i \otimes \mathbf{v}_i^{\top}) \times s_i \tag{2.11}$$

Here, $\mathbf{U}$ and $\mathbf{V}$ are the left and right orthogonal matrices and $\mathbf{S}$ is a diagonal matrix with the singular values $(s_1, s_2, ..., s_r)$ as the diagonal elements. These are usually ordered $s_1 \geq s_2 \geq s_3 \geq ... \geq s_r$. The orthogonal matrix $\mathbf{U}$ is composed of individual unitary orthogonal modes/vectors $\mathbf{u}_i$ i.e. [$\mathbf{u}_1$, $\mathbf{u}_2$, ..., $\mathbf{u}_r$] with $\mathbf{u}_i^\top \cdot \mathbf{u}_j = 1$ for $i = j$ and zero otherwise. Similarly, $\mathbf{V}$ = [$\mathbf{v}_1$, $\mathbf{v}_2$, ..., $\mathbf{v}_r$]. Physically, one can think of SVD as decomposing the matrix into individual orthogonal eigenmaps of the response function 'map' $\mathbf{R}_\mathrm{T}$ (in λ and τ), given by $(\mathbf{u}_i \otimes \mathbf{v}_i^\top) \times s_i$, where s_i corresponds to individual map's contribution in making up the matrix and '$\otimes$' denotes the outer product of the vectors. Given that the $\mathbf{R}_\mathrm{T}$ matrix is oriented such that individual rows correspond to sensitivity at a given depth τ while individual columns correspond to sensitivity for a given wavelength λ, we can interpret individual $\mathbf{u}_i$ and $\mathbf{v}_i$ vectors as the eigenmodes for the depth and wavelength space, respectively.

When computing the *pseudo-inverse* of the matrix, it is important to know its rank r, which signifies the maximum number of linearly independent/non-degenerate rows (or columns) of the matrix. The matrix is said to be full rank when $r = min\ (n, m)$, where size of the matrix is $n \times m$. If there are degeneracies within the matrix, then rank $r < min\ (n, m)$ and is equal to the number of singular values s_i that are non-zero. Once we identify the rank r of the matrix (the number of non-zero s_i), then we can compute its *pseudo-inverse* which is given by

$$\mathbf{R}_\mathrm{T}^{-1} \ = \ \mathbf{V}_r \cdot \mathbf{S}_r^{-1} \cdot \mathbf{U}_r^\top = \sum_{i=1}^{r} \frac{\mathbf{v}_i \otimes \mathbf{u}_i^\top}{s_i} \ , \tag{2.12}$$

from which the coefficients, from Equation 2.9, follow

$$\mathbf{C} = \left(\mathbf{V}_r \cdot \mathbf{S}_r^{-1} \cdot \mathbf{U}_r^\top \right) \ \cdot \ \mathbf{G} = \sum_{i=1}^{r} \mathbf{v}_i \times \left(\frac{\mathbf{u}_i^\top \cdot \mathbf{G}}{s_i} \right) \tag{2.13}$$

Here, $\mathbf{U}_r$ (and similarly $\mathbf{V}_r$, $\mathbf{S}_r$) corresponds to the matrix constructed by keeping the orthogonal eigenvectors ($\mathbf{u}_i$) corresponding to r largest singular values, i.e. $\mathbf{U}_r$ = [$\mathbf{u}_1$, $\mathbf{u}_2$, ..., $\mathbf{u}_r$].

The central issue with spectropolarimetric inversions in general, and with the formulation of the OLA averaging kernel in particular, is that they involve solving a discrete ill-posed system of equations for which the numerical rank r is ill-determined. The ordered singular values s_i

of the response function matrix $\mathbf{R}_{\mathrm{T}}$ quickly decay to smaller values with increasing i, with the corresponding eigenvectors $\mathbf{u}_i$ and $\mathbf{v}_i$ becoming more oscillatory. This is shown in Figure 2.4. Those modes that are potentially more useful in localizing the contribution to the spectral response have smaller singular values. The exponential decay of s_i with increasing index i (upper panel in Figure 2.4) indicates that the response function matrix is severely ill-posed, with only a few orthogonal modes capturing most of the information in the matrix. For $\mathbf{R}_{\mathrm{T}}$ corresponding to the mean MURaM model being considered (with 121 depth points and more than 400 wavelength points), over 100 orthogonal modes have nonzero singular values, but only the largest 11 of them contribute to 99.9% of the total singular value sum (s_i to the left of vertical dashed line in the top plot in Figure 2.4). Unfortunately, the ill-posedness changes only very slowly with the additional spectral response functions (additional observations at other wavelengths) because of the underlying inherent degeneracy in the formation of spectra.

The severe ill-posedness (exponential decay rate of s_i) of the $\mathbf{R}_{\mathrm{T}}$ matrix is the central issue when computing $\mathbf{C}$ using Equation 2.13. Ideally, $\mathbf{u}_i^{\top} \cdot \mathbf{G}$ should decrease faster than s_i with increasing i, so that the ratio $\left(\frac{\mathbf{u}_i^{\top} \cdot \mathbf{G}}{s_i}\right)$ remains less than one. This is called the Discrete Picard Condition [24, 25, 26, 27, 65] and ensures the stability of the solution. When the system is severely ill-posed, this condition is usually not met, and leads to coefficients that are uncontrollably larger and a solution dominated by the highly oscillatory modes which are not dominant in the original $\mathbf{R}_{\mathrm{T}}$ matrix, as their corresponding singular value s_i contributions are negligible. When these larger amplitude coefficients are used in Equation 2.10, the inversion solution $\mathbf{C}^{\top} \cdot \mathbf{\Delta I}$ is typically dominated by the error term $\mathbf{C}^{\top} \cdot \boldsymbol{\varepsilon}$, and does not correspond to the desired $\mathbf{A}_{\mathrm{T}}^{\top}(\tau_i) \cdot \frac{\mathbf{\Delta T}}{\mathbf{T}}$.

As already mentioned, to successfully solve an ill-posed system (the core of many inverse problems including those of spectropolarimetry), regularization is needed. In the context of averaging kernel construction (solving Equation 2.9) regularization means dampening or removing the contribution of smaller s_i. The truncated SVD method (TSVD, [24, 25, 27]), achieves this by simply inverting a lower-rank version of the matrix, i.e. by using only the k ($\ll r$) most dominant singular modes to compute the inversion. Employing this technique, we compute coefficients from

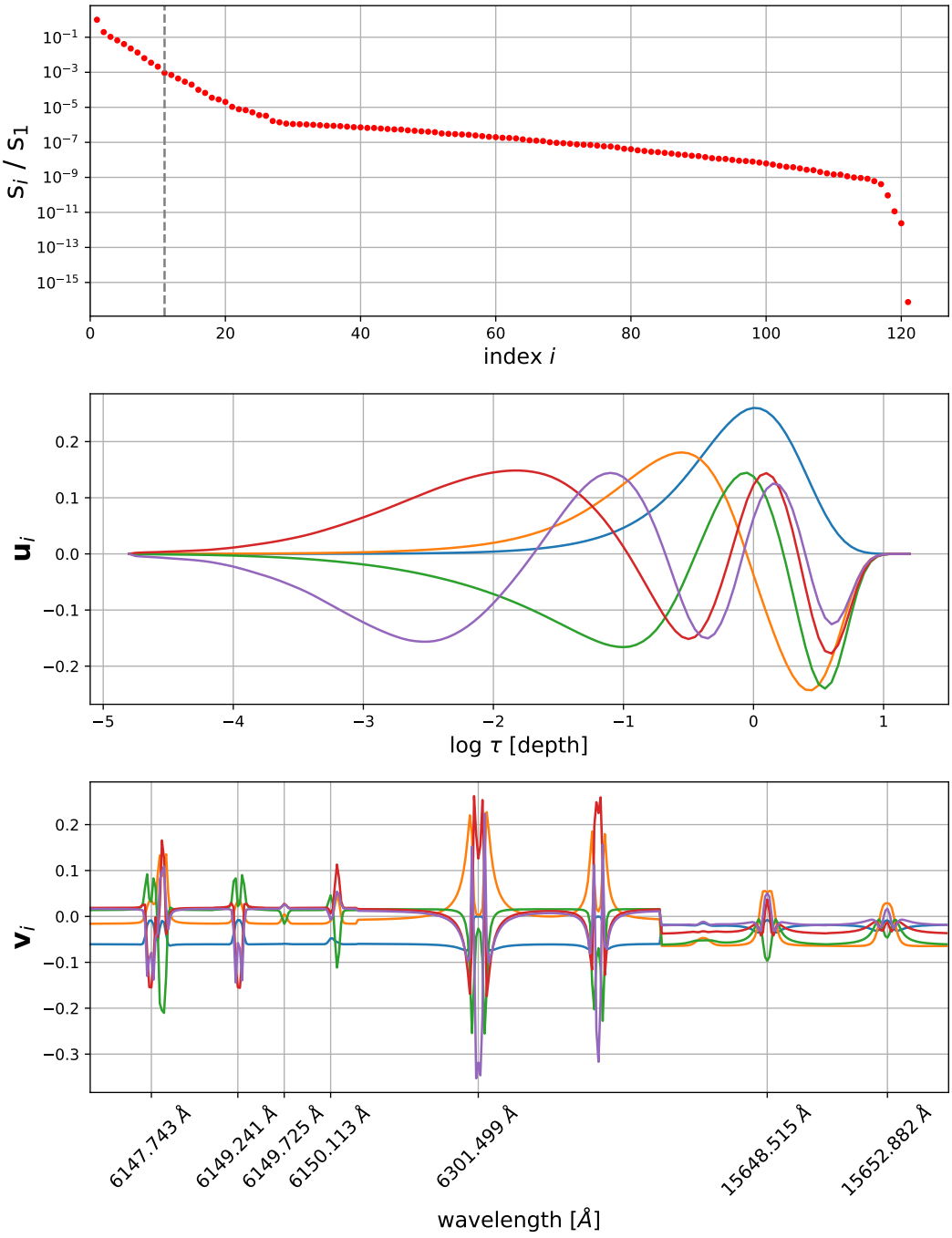

Figure 2.4: (Top-plot) Singular values s_i, normalized by dominant singular value s_1, obtained from SVD for $\mathbf{R}_{\mathrm{T}}$. Vertical dashed line at $i = 11$ mark the index where the cumulative sum of the largest singular values add to about 99.9% of the total sum. (Middle and bottom plots) $\mathbf{u}_i$ and $\mathbf{v}_i$ vectors corresponding to the 5 largest singular values. Note that a more oscillatory eigenvector in general corresponds to a smaller singular value.

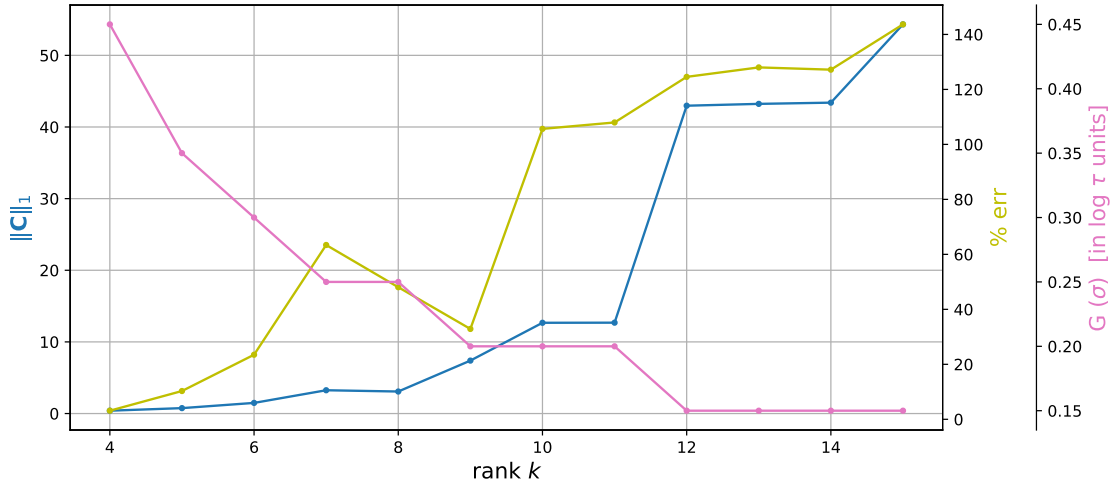

Figure 2.5: Parameters obtained when inverting at $\log \tau = -0.25$, for the perturbation in Figure 2.1 using OLA, for different rank k. L1 norm of $\mathbf{C}$ ($\sum_i |c_{\lambda_i}|$) is shown in blue, minimum target function width achievable in pink and the % error contribution in the inverted solution $\left(\left|\frac{\mathbf{C}^\top \cdot \boldsymbol{\varepsilon}}{\mathbf{C}^\top \cdot \Delta\mathbf{I}}\right| \times 100\right)$ in yellow.

Equation 2.13, by replacing rank r with a lower rank k so that $\mathbf{U}_k = [\mathbf{u}_1, \mathbf{u}_2, ..., \mathbf{u}_k]$, with $\mathbf{V}_k$ and $\mathbf{S}_k$ truncated similarly. The biggest challenge then is determining what rank k to employ. This would not be as big a problem if we had the error estimates $\boldsymbol{\varepsilon}$, as we could then determine if our solution is error dominated or not. In addition, we could also incorporate $\boldsymbol{\varepsilon}$ in Equation 2.9 and solve for coefficients that simultaneously minimize the error contribution in the solution i.e. $\mathbf{R}_\mathrm{T} \cdot \mathbf{C} = \mathbf{A}_\mathrm{T}$, and $\mathbf{C}^\top \cdot \boldsymbol{\varepsilon} = 0$. Unfortunately, $\boldsymbol{\varepsilon}$ is not available because, while estimates of the spectral noise in the observational data can be made, we do not in general know how far away the guess-model is from the real atmosphere, and we do not thus know the magnitude of the truncated non-linear contributions to $\boldsymbol{\varepsilon}$.

Typically, the lower the approximated rank k, the smaller are the coefficient amplitudes and smaller the relative error magnitude compared to the idealized solution, i.e. $\mathbf{C}^\top \cdot \boldsymbol{\varepsilon}$ is small compared to $\mathbf{A}_\mathrm{T}^\top \cdot \frac{\Delta\mathbf{T}}{\mathbf{T}}$. This is illustrated by Figure 2.5, where we plot for our test problem $\|\mathbf{C}\|_1$ (L1 norm of the coefficients i.e. $\sum_i |c_{\lambda_i}|$) in blue and the fractional error $\left(\left|\frac{\mathbf{C}^\top \cdot \boldsymbol{\varepsilon}}{\mathbf{C}^\top \cdot \Delta\mathbf{I}}\right| \times 100\right)$ in yellow. The two follow similar trends with k. At the same time, the larger the rank k the closer the averaging

kernel $\mathbf{A}_\mathrm{T}$ is to the target function $\mathbf{G}$ of a given width. This is because the coefficient vector $\mathbf{C}$ from Equation 2.13, corresponds to the minimum residual solution of the approximated matrix i.e. $min\ \left\|\mathbf{R}_\mathrm{T}^k \cdot \mathbf{C} - \mathbf{G}\right\|_2$, where $\mathbf{R}_\mathrm{T}^k$ is the k-rank approximated version of the original matrix $\mathbf{R}_\mathrm{T}$. The averaging kernel $\mathbf{A}_\mathrm{T}$, given by $\mathbf{R}_\mathrm{T}^k \cdot \mathbf{C}$ $(= \mathbf{R}_\mathrm{T} \cdot \mathbf{C})$, can be rewritten as $\left(\mathbf{U}_k \otimes \mathbf{U}_k^\top\right) \cdot \mathbf{G}$. The larger the rank k, the closer $\mathbf{U}_k \otimes \mathbf{U}_k^\top$ is to the identity matrix I and thus the closer is $\mathbf{A}_\mathrm{T}$ to $\mathbf{G}$. Physically, $\mathbf{A}_\mathrm{T}$ is given by the linear combination of the $\mathbf{u}_i$ vectors i.e. $\mathbf{A}_\mathrm{T} = \sum_{i=1}^{k} \mathbf{u}_i \times \left(\mathbf{u}_i^\top \cdot \mathbf{G}\right)$, and a larger value of k means including more $\mathbf{u}_i$ modes, those which are more oscillatory. This makes it easier to construct an averaging kernel that is a close fit to a narrower target function, but at the cost of larger coefficient amplitudes which amplify $\boldsymbol{\varepsilon}$. The pink curve in Figure 2.5 plots the minimum target function width within a fixed value of the L1 norm of the difference between $\mathbf{A}_\mathrm{T}$ and $\mathbf{G}$. With a larger rank k we can construct narrower averaging kernels at a given depth location.

To summarize, there are two opposing aims. We want to use smaller rank k so that the coefficient amplitudes are smaller and prevent potential error amplification. At the same time, a larger rank k allows us to construct narrower averaging kernels that lead to inversion solutions that are more localized, with lesser spatially averaged inverted $\left\langle \frac{\Delta \mathrm{T}}{\mathrm{T}}(\tau_i) \right\rangle$, making it closer to the underlying $\frac{\Delta \mathrm{T}}{\mathrm{T}}(\tau_i)$. Without accurate error estimates, it is a non-trivial challenge to determine what k leads to an optimal inversion, the one that is the best balance between these opposing aims. In Section 2.2.4, we follow up with an iterative scheme to determine the 'optimal' rank k for the near optimal OLA inversion. In the next section we more generally discuss how OLA inversions are carried out for a given depth τ_i assuming that rank k is known.

2.2.2 OLA inversion at a given depth location

To obtain the most localized inversion at τ_i, we need to find the minimum width target function $\mathbf{G}$ at that depth, that can be reasonably fit by an averaging kernel. To do this, we define a range of target function widths (on the log τ grid), which span from 0.05 to 0.5, in steps of 0.05 $\Delta \log \tau$ (model grid spacing). Starting with the minimum width target function, we solve for

coefficients (Equation 2.13) and the averaging kernel ($\mathbf{R}_{\mathrm{T}} \cdot \mathbf{C}$) and check if the averaging kernel fits this target function within a specified limit. We chose the fit measure based on the L1 norm of the difference between the two. Given that the area under the target functions is normalized to 1, this fit measure can be approximately interpreted as a % difference. If the difference norm is below a specified upper-limit, we conclude that the averaging kernel approximately represents the target function and use the coefficients to compute the inverted $\left\langle \frac{\Delta \mathrm{T}}{\mathrm{T}}(\tau_i) \right\rangle = \mathbf{C}^{\top} \cdot \Delta\mathbf{I}$, and further $\Delta \mathrm{T}(\tau_i)$ $= \left\langle \frac{\Delta \mathrm{T}}{\mathrm{T}}(\tau_i) \right\rangle \times \mathrm{T}(\tau_i)$. The inversion is then complete at that location.

When deciding on the fitting parameter, it is important to not make it too stringent (value is too small) so that it becomes impossible (for a given rank k) to construct the averaging kernel at all, while also not making the condition too relaxed (value is too large) so that the averaging kernel does not resemble target function at all. Empirically, we find that 0.2 (20% error) works well in general. It is possible that none of the target functions within the width range examined can be reasonably approximated using the given spectral response functions, in which case we conclude that, for given rank k, OLA inversion can not be achieved at that location. Because spectral sensitivity is not uniformly distributed with depth, failure often occurs above and below a limit range of depths. These non-invertible regions pose a particular challenge when iteration (multiple inversion cycles) is required for the final solution, even in the regions where we can construct kernels and do inversions (see Section 2.2.5).

The averaging kernel construction scheme outlined gives the OLA scheme an advantage as an inversion method. The width of the averaging kernel achieved represents the spatial resolution of the inverted solution, and that resolution depends on the response function set employed. Even before performing an inversion, kernel construction allows direct quantitative assessment of spectral line combinations and their potential utility in inversions for a given variable at a given depth. While that assessment also depends on the starting guess-model (via the response functions) and the rank k used, it serves as a starting point for line-combination determination. This is discussed in more detail in Chapter 5.

2.2.3 OLA inversion at multiple depth locations

So far we discussed how OLA inversion is carried out at a given depth location (assuming rank k is known). In order to invert at 'all possible' depths, we repeat the process in last section at each depth. We use the same rank *pseudo-inverse* matrix at all depths. The depth dependent inversion solution obtained corresponds to an 'inversion cycle'. Figures 2.6 show the results from our test case (Figure 2.1) after one inversion cycle for two different rank choices: $k = 5$ (top plot) and $k = 10$ (middle plot). These demonstrate the effect of using too small and too large a rank value. In each plot, the red curve corresponds to the difference between the actual and guess $\mathbf{T}$, that the inversion aims to recover. The green curve corresponds to the inverted $\mathbf{\Delta T}$ (inverted − guess $\mathbf{T}$) and the yellow curve corresponds to the error contribution of the higher order truncation error to the solution.

A lower rank $k = 5$ can only achieve wider $\mathbf{A}_\mathrm{T}$ averaged inversion solution (orange curve in the bottom plot of Figure 2.6). The solution corresponds to an 'average' of the underlying perturbation and has smaller error contribution, but it is achieved only over a smaller depth range (the inversion window). With higher rank $k = 10$, inversion is achieved over a wider range of depths with narrower averaging kernels (blue curve in the bottom plot of Figure 2.6), but the corresponding inversion solution does not resemble the underlying perturbation and is error dominated. It is important to emphasize that the solution ($\mathbf{C}^\top \cdot \mathbf{\Delta I}$) at each depth is a sum of desired solution ($\mathbf{A}_\mathrm{T}^\top \cdot \frac{\mathbf{\Delta T}}{\mathbf{T}}$) and the 'unknown' error contribution ($\mathbf{C}^\top \cdot \boldsymbol{\varepsilon}$). While the desired solution ($\mathbf{A}_\mathrm{T}^\top \cdot \frac{\mathbf{\Delta T}}{\mathbf{T}}$) is bounded and depends on the magnitude of the underlying perturbation ($\frac{\mathbf{\Delta T}}{\mathbf{T}}$), the error contribution is not and can overwhelm the solution when the solution becomes error dominated.

It is evident from these figures that the error contribution is oscillatory with depth. This reflects the oscillatory behavior of the magnitude of the coefficients with depth. This is depicted by the blue-dashed curve in top and middle plot in Figure 2.6 which corresponds to the L1 norm of the coefficients ($\sum_i |c_{\lambda_i}|$) with depth. The coefficient vector $\mathbf{C}$, computed using Equation 2.13 at a given depth, is a linear combination of the eigenvectors $\mathbf{v}_i$ with $\frac{\mathbf{u}_i^\top \cdot \mathbf{G}}{s_i}$ as the multiplier. The

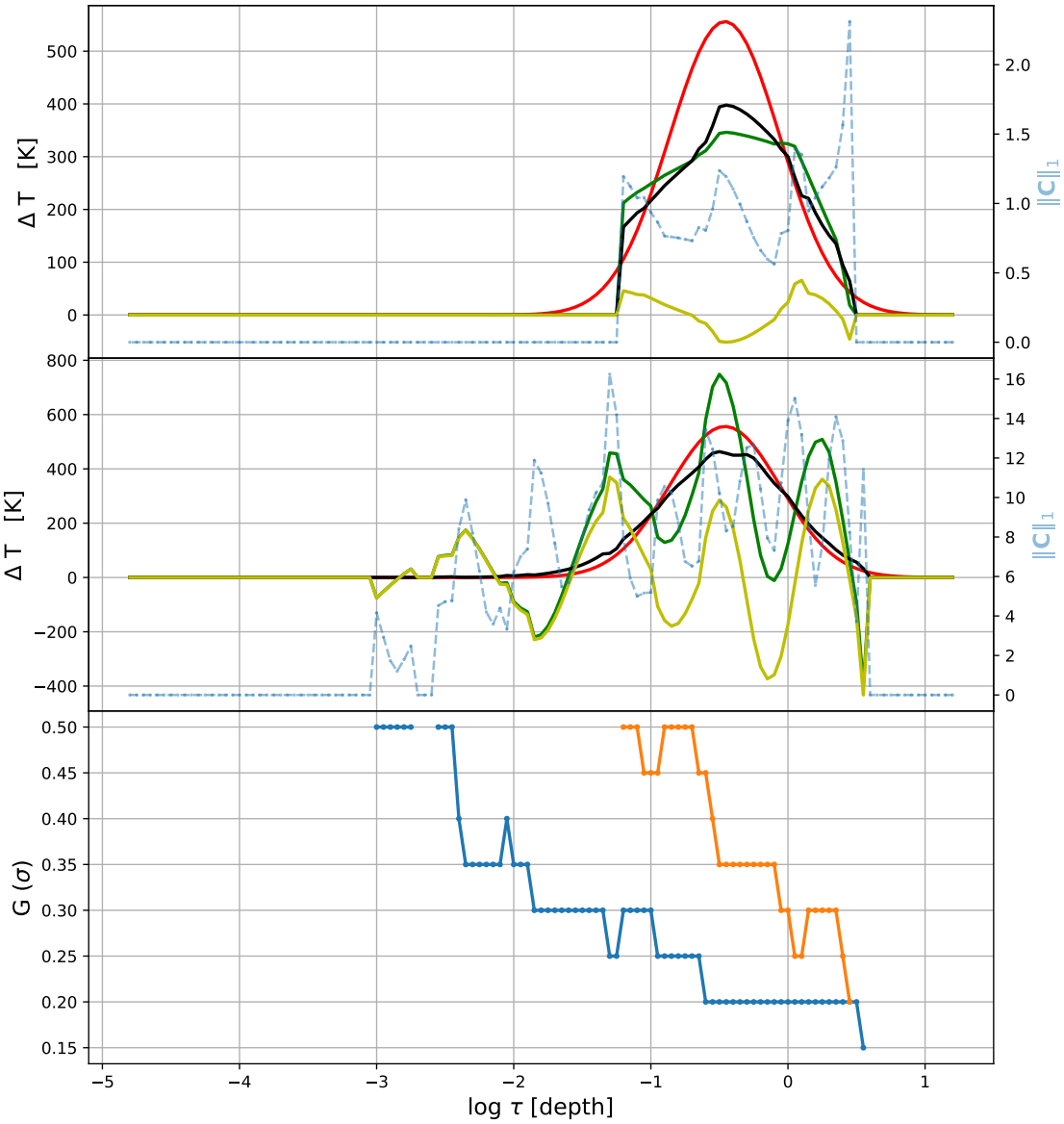

Figure 2.6: OLA inversion result of the test case in Figure 2.1 after 1 inversion cycle for rank $k = 5$ (top-plot), and $k = 10$ (middle-plot). In both panels, red curve corresponds to the underlying perturbation, green curve corresponds to OLA inverted $\Delta\mathbf{T}$, yellow curve corresponds to the error contribution in those inversions $(\mathbf{C}^\top \cdot \boldsymbol{\varepsilon}) \times \mathbf{T}$ and black curve corresponds to the 'desired' inversion solution (OLA solution without error contribution) i.e. $(\mathbf{A}_\mathrm{T}{}^\top \cdot \frac{\Delta\mathbf{T}}{\mathbf{T}}) \times \mathbf{T} = (\mathbf{C}^\top \cdot \Delta\mathbf{I} - \mathbf{C}^\top \cdot \boldsymbol{\varepsilon}) \times \mathbf{T}$. In blue-dashed we plot the L1 norm of the $\mathbf{C}$. (Bottom-plot) Corresponding target function width as a function of depth for rank $k = 5$ (orange) and $k = 10$ (blue).

vectors $\mathbf{v}_i$ are orthonormal and the linear multipliers determine the overall contribution of $\mathbf{v}_i$ to the coefficients. For illustration, assume that a single eigenmode, that for which the multiplier has the largest magnitude, ultimately dictates the coefficient magnitude. Since the linear multiplier depends on $\mathbf{G}$ and $\mathbf{u}_i$, with $\mathbf{G}$ a positive Gaussian and $\mathbf{u}_i$ oscillatory, as the target function peak location is moved from one depth to another (to invert at multiple depths) the magnitude of the multiplier $\left(\frac{\mathbf{u}_i^\top \cdot \mathbf{G}}{s_i}\right)$ oscillates in sign. The real variation of coefficient norms $\|\mathbf{C}\|_1$ with depth is more complex than this simple illustration. The target function width varies with depth and there are contributions from multiple eigenmodes, but the error contribution none-the-less reflects their oscillatory nature with higher spatial frequency (and higher amplitude) for higher k.

The above example illustrates the importance of determining the 'optimal' *pseudo-inverse* matrix rank to employ. The rank determines the spatial resolution of the solution, the range of depths over which the OLA inversion can be successfully undertaken, and the overall error contribution to those inversions. Determining the 'optimal' rank is one of the hardest tasks when doing OLA inversions (and any inversion problem in general). In the next section we discuss how we tackled this issue.

2.2.4 Iterative OLA method

As mentioned in Section 2.2.1, it is non-trivial to find the rank that would lead to an inversion solution that is an optimal balance between the inversion resolution, inversion depth range, and the error contribution to the solution after an inversion cycle. This is due to the inherent flaw in the spectral difference measure ($\Delta\mathbf{I}$) which is employed to assess the quality of our inversion, i.e. how close is the inverted model to the observed model. The difference between the observed and the guess-model spectra ($\Delta\mathbf{I}$) does not uniquely determine the solution. That flaw is a combined result of the fact that the problem is ill-posed (steep decay rate of singular values) and that there is non-zero error $\boldsymbol{\varepsilon}$ in the linear system of equations that are being solved. These two properties limit the largest rank k that can be used when solving the 1st order system of equations 2.5 (or

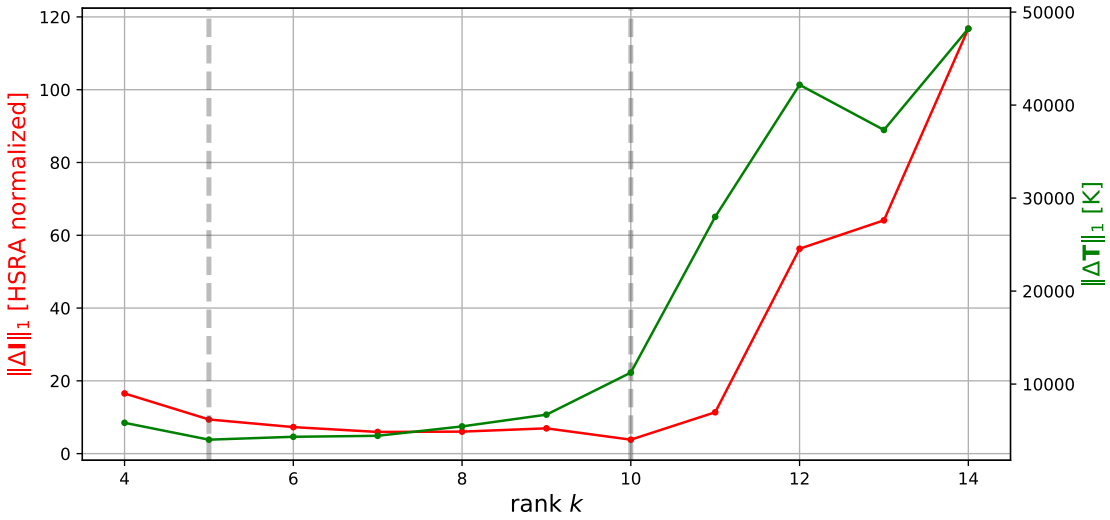

Figure 2.7: Parameters obtained from the OLA inversion of the test case in Figure 2.1 (after 1 inversion cycle) for different ranks to demonstrate the underdetermined nature of the inverse problems. Green curve corresponds to L1 norm of the difference between the underlying and inverted $\mathbf{T}$ and red curve corresponds to the L1 norm of the corresponding spectral differences from these models.

when solving for coefficients in Equation 2.9) and convert even a 'seemingly' overdetermined system (number of equations larger than the number of unknowns i.e. when solving Equation 2.5, number of rows > number of columns), into an 'effectively' underdetermined one ('actual' number of linearly independent equations $\ll$ number of unknowns). The system of equations is poorly constrained and multiple solutions $\frac{\Delta \mathbf{T}}{\mathbf{T}}$ exist that could account for $\Delta \mathbf{I}$. The OLA inversion method keeps the inversion solution stable by finding solutions only at those locations where a 'localized' averaging kernel can be constructed, but it does not eliminate the underlying non-uniqueness issue.

We illustrate this mismatch between solutions that achieve best spectral fitting and those which yield best model matching with Figure 2.7. There we plot the L1 norm of the difference between the observed spectra and that derived from the inverted model (red), and L1 norm of the difference between the actual (observed) and inverted $\mathbf{T}$ (green) as a function of rank k. The solution where inverted $\mathbf{T}$ is closest to actual $\mathbf{T}$ (lowest model difference) corresponds to $k = 5$, while that which we would pick based on the least spectral difference measure corresponds to

$k = 10$. Note that outside these test cases (in the real world) only the latter measure is available. The underlying inversion solutions after 1 cycle for these two ranks are those shown in Figure 2.6. It is evident from these plots that the inversion solutions are drastically different, and that that based on the best spectral fit are strongly error dominated. This is a consequence of the inherent underdetermined nature of the problem, and illustrates that the 'best' spectral fit solution doesn't necessarily corresponds to the 'best' model fit solution.

When inverting spectropolarimetric data, the $\frac{\Delta \mathbf{T}}{\mathbf{T}}$ obtained by inversion usually does not match the underlying $\frac{\Delta \mathbf{T}}{\mathbf{T}}$ after a single inversion cycle. This is because underlying perturbation magnitudes are usually large i.e. the actual solar atmosphere lies far from the initial guess. The neglected higher order terms in Equation 2.5 are not insignificant and the relationship between $\Delta \mathbf{I}$ and $\frac{\Delta \mathbf{T}}{\mathbf{T}}$ is not linear. Multiple inversion cycles are needed to get around this issue.

After each inversion cycle, the inverted model from the previous cycle is used as a starting guess-model in the next. Since the starting guess-model changes with each cycle, so do the response functions. Further, if the iteration is convergent, as the perturbation amplitude decreases, so do the non-linear errors, and higher rank *pseudo-inverse* matrix can be employed to refine the solution. Motivated by SIR to increase the number of nodes as inversion proceeds, we preferentially use smaller rank in the starting cycles, to obtain coarse resolution inversions which are less likely to be error dominated, and higher rank in subsequent cycles, as the inverted model gets closer to the observed atmosphere (i.e. $\frac{\Delta \mathbf{T}}{\mathbf{T}}$ is getting smaller). If $\boldsymbol{\varepsilon}$ decreases with iteration (when iterative updates are in the 'right' direction), the system can tolerate larger magnitude coefficients with lower total error, allowing this increased rank in the later cycles and higher resolution inversions.

The issues are then, how to determine the maximum rank k to be used at the end of the inversion cycle series, which ultimately determines the quality of the final inversion (in SIR one sets this manually in terms of the number of nodes), and how to scale up to it from a lower rank early in the iteration cycle. It is the overall balance between $\mathbf{A}_{\mathrm{T}}{}^{\top} \cdot \frac{\Delta \mathbf{T}}{\mathbf{T}}$ and $\mathbf{C}^{\top} \cdot \boldsymbol{\varepsilon}$, that determines the maximum rank beyond which the inversion solutions are error dominated. The aim is that the iterative algorithm itself determines the maximum rank that can be tolerated without knowing

the actual solution to be achieved. The 'hope' is that, as the system gets closer to the largest tolerable rank, if inversion solutions start to get error dominated, that will be reflected in the spectral difference measure, so that, when the spectral fitting starts to get worse, we can conclude that we have arrived at the best solution and that any further inversion cycles would lead to a worse solution. In reality, this hope might not always be met and there may be a lag between when the solution is error dominated and when it is reflected in the spectral fit measure, as indicated by the example of Figure 2.7 and discussion above.

It is a bit counter-intuitive to understand why the spectral fit could get worse with increasing rank k as using a larger rank should result in a smaller residual $\Delta\mathbf{I}$. The answer lies in the disconnect between $\Delta\mathbf{I}$ in the Equation 2.5, and one computed from the difference between observed and $\frac{\Delta\mathbf{T}}{\mathbf{T}}$ updated inverted-model spectra. While, using a large rank would result in $\mathbf{R_T}^\top \bullet \frac{\Delta\mathbf{T}}{\mathbf{T}}$ to be close to $\Delta\mathbf{I}$ (in Equation 2.5), the inverted $\frac{\Delta\mathbf{T}}{\mathbf{T}}$ may be error dominated and could thus result in an inverted $\mathbf{T}$ that is away from the underlying $\mathbf{T}$. The problem is that, because of the underdetermined nature of the problem, $\Delta\mathbf{I}$ from the updated model may not readily reflect this 'bad' inversion.

2.2.4.1 Iterative OLA method: implementation

In this section we discuss the implementation of the iterative OLA method i.e. inversion over multiple cycles. Starting with mean MURaM as the guess-model we compute guess $\mathbf{I}$, $\Delta\mathbf{I}$ and the corresponding response functions $\mathbf{R_T}$. Given that the error magnitudes are larger at the starting cycles, we initially employ smaller rank k (safest bet) when constructing the *pseudo-inverse* matrix. The intention is to compute coefficients that would (most likely) not result in an error dominated solutions even though it comes at the expense of inverting with wider averaging kernels at fewer total depth locations.

From trial and error, we find that a safe value for k can be determined using k most dominant

singular values s_i that add up to 95% of the total sum i.e. starting cycle k is given so that it satisfies

$$\frac{\sum_{i=1}^{k} s_i}{\sum_{i=1}^{n} s_i} \times 100 \quad \approx \quad 95.0\ \% \tag{2.14}$$

For our starting response function matrix, $k = 5$ meets this criterion. Using this k, we obtain initial inversion solutions $\frac{\Delta \mathbf{T}}{\mathbf{T}}$, and thus $\Delta \mathbf{T}$ ($= \mathbf{T} \times$ inverted $\frac{\Delta \mathbf{T}}{\mathbf{T}}$). At those depths where kernels cannot be constructed with this limited eigenmode set, $\Delta \mathbf{T}$ is set to 0. Note, whether or not kernel can be constructed at a given depth is determined based on the criteria discussed in Section 2.2.2. An example of an inverted solution $\Delta \mathbf{T}$ after the 1st cycle is shown in green-dashed in the top plot in Figure 2.8. It is the same as that shown in the upper panel of Figure 2.6. As evident from the figure, the solution is jagged and has sharp edges at the boundaries of the region over which OLA inversion is possible. These irregularities result because the OLA method does not aim to find a globally smooth solution but, on the contrary, produces localized solutions independently at each depth. Moreover, the averaging kernel width varies with depth and in some cases there may be gaps in the OLA inversion window where kernels can't be constructed. The inversion solution obtained by adding this inverted $\Delta \mathbf{T}$ to the guess $\mathbf{T}$, similarly shows these defects. This is problematic because the irregular/jagged inverted $\Delta \mathbf{T}$ is not a final solution, and the irregularities in the inverted $\mathbf{T}$ pose difficulties when it is used as a guess-model for the next iteration cycle. For each iteration a new set of spectra and response functions must be computed from the input model atmosphere and, if the underlying model is irregular, the resulting response functions are also irregular. This is illustrated by Figure 2.8 (middle plot) where abrupt changes in the response functions are clearly apparent. With such irregular response functions, it gets increasingly harder to construct smooth-Gaussian averaging kernels with successive iterations.

A simple fix to this issue is to smooth the inverted $\Delta \mathbf{T}$ at the end of the inversion cycle before adding it to guess $\mathbf{T}$ to obtain a smooth inverted $\mathbf{T}$. In implementation, we linearly interpolate to fill any gaps in inverted $\Delta \mathbf{T}$, and smooth it with a Gaussian kernel. The width of the smoothing kernel is equal to the narrowest averaging kernel that we were able to constructed during that

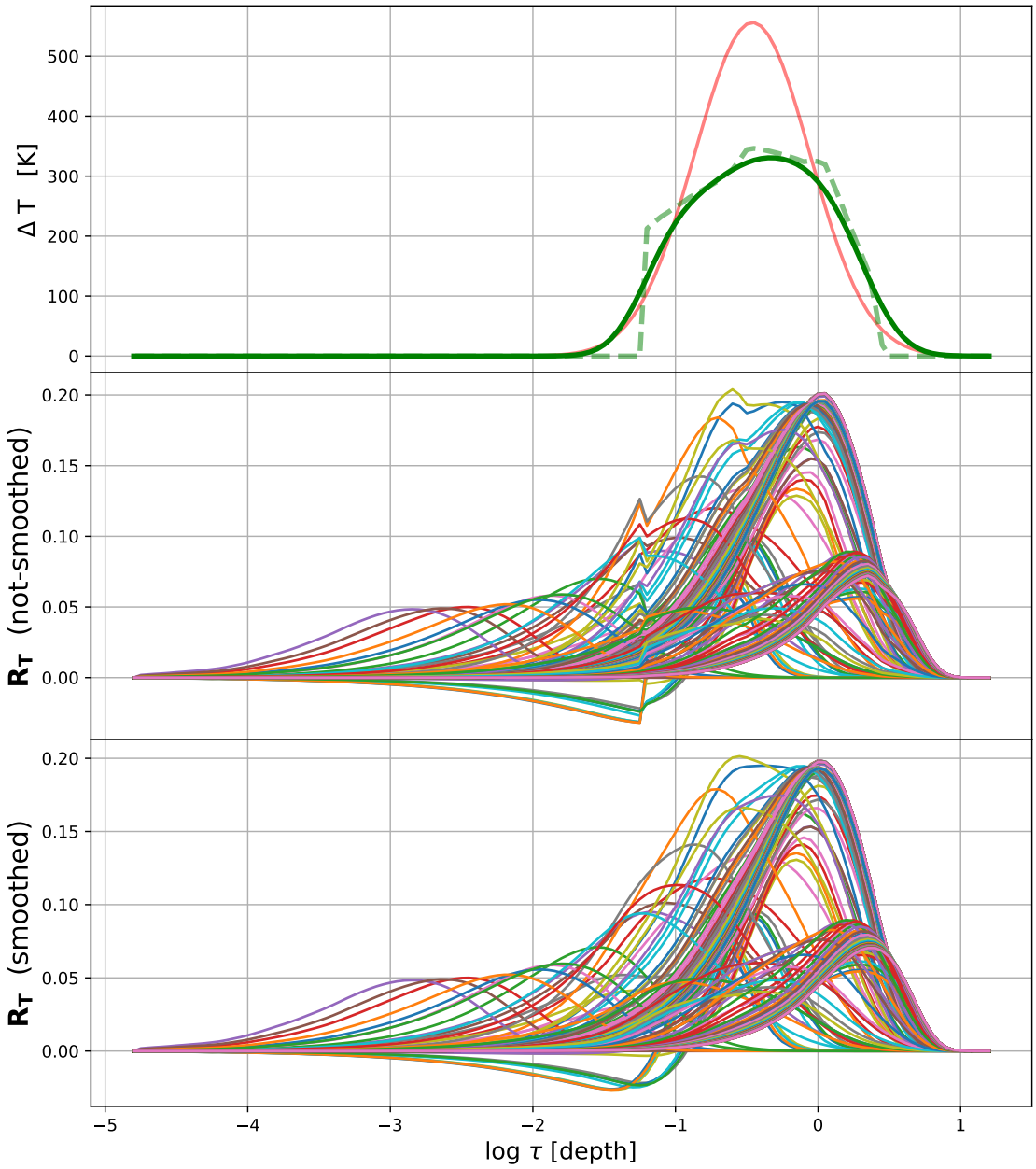

Figure 2.8: (Top plot) OLA inversion result for the test case in Figure 2.1 after 1 inversion cycle with *pseudo-inverse* computed using rank $k = 5$. The OLA inversion solution (green-dashed curve) is irregular. $\mathbf{R}_{\mathrm{T}}$ computed using the irregular $\mathbf{\Delta T}$ updated model is also irregular (middle panel). Bottom panel shows the smooth $\mathbf{R}_{\mathrm{T}}$ obtained when the model is updated using smoothed inverted $\mathbf{\Delta T}$ (green-solid curve in top plot).

cycle. It is important to note that we smooth $\Delta\mathbf{T}$ at all depths including the regions outside the OLA inversion boundary, i.e. where $\Delta\mathbf{T} = 0$, resulting in a smeared $\Delta\mathbf{T}$ at the edges of the OLA inversion window. This smoothing thus helps with another issue, the 'edge-effect', inherent to the iterative OLA method that we will discuss further in Section 2.2.5. The smoothed inverted $\Delta\mathbf{T}$ obtained is shown by the green curve in the top plot of Figure 2.8. The spatial resolution of this smoothed solution no longer corresponds to the averaging kernel width employed at each depth, but is instead approximately given by the convolution between the averaging kernel and the Gaussian smoothing kernel.

Before moving on to the next inversion iteration cycle, a decision is required on whether to continue doing inversions using the same rank, increase the rank or stop inverting altogether. This decision is based on three spectral difference L1 norm measures:

- Inverted $\|\Delta\mathbf{I}_\lambda\|_1^l$ = L1 norm of the difference between the observed spectra and the inverted-model spectra after cycle l.
- Guess $\|\Delta\mathbf{I}_\lambda\|_1^l$ = L1 norm of the difference between the observed spectra and the guess-model spectra after cycle l.
- Best $\|\Delta\mathbf{I}_\lambda\|_1^l$ = L1 norm of the spectral difference between the observed and that corresponding to the inverted model for which inverted $\|\Delta\mathbf{I}_\lambda\|_1^l$ has been minimum so far after cycle l. We take this model to also correspond to the best inverted model after cycle l. Note that the best $\|\Delta\mathbf{I}_\lambda\|_1^0$ (before the very first inversion cycle) is initialized to guess $\|\Delta\mathbf{I}_\lambda\|_1^0$ (L1 norm of the spectral differences between observed and mean MURaM guess-model spectra).

The decision on what rank to use for the next cycle or stop inverting altogether, depends on which of the following categories the above mentioned spectral norm measures fall into (in the given order):

- Case 1 (good inversion): inverted $\|\Delta\mathbf{I}_\lambda\|_1^l <$ best $\|\Delta\mathbf{I}_\lambda\|_1^l$
- Case 2 (stagnant inversion): inverted $\|\Delta\mathbf{I}_\lambda\|_1^l \approx$ guess $\|\Delta\mathbf{I}_\lambda\|_1^l$

- Case 3 (bad inversion): inverted $\|\Delta\mathbf{I}_\lambda\|_1^l >$ best $\|\Delta\mathbf{I}_\lambda\|_1^l$

In the starting cycles, given that rank k is small, the inversion solutions are most likely not error dominated, which implies that the inverted models get closer to the underlying atmosphere with iteration, and thus the spectral differences fall into Case 1 i.e. inverted $\|\Delta\mathbf{I}_\lambda\|_1^l$ is smaller compared to the last best $\|\Delta\mathbf{I}_\lambda\|_1^l$. In this case, we update the best-model with the inverted model (and the best $\|\Delta\mathbf{I}_\lambda\|_1^l$) and continue using the same rank in the next inversion cycle with the updated guess-model. The intention is to employ the low rank as long as the solution is improving to avoid error amplification.

When using the same rank over multiple inversion cycles, the subsequent inversion update gets smaller. This is because the guess $\Delta\mathbf{T}^l$ (observed $\mathbf{T}$ − guess $\mathbf{T}^l$), to be inverted for, gets smaller in magnitude (inverted model getting closer to underlying atmosphere) and more oscillatory with cycle. The oscillatory nature is a result of the fact that inverted $\Delta\mathbf{T}^l$ is smoother than the guess $\Delta\mathbf{T}^l$ and the guess $\Delta\mathbf{T}^{l+1}$ for the next cycle is given by the difference between guess $\Delta\mathbf{T}^l$ and inverted $\Delta\mathbf{T}^l$. While the underlying response functions get updated as we update the guess-model in each cycle, the averaging kernel widths do not change noticeably when using the same rank. These 'similarly wide' kernels are unable to resolve the underlying oscillatory differences (guess $\Delta\mathbf{T}^l$) and the inverted $\Delta\mathbf{T}^l$ magnitudes get successively smaller. The resulting inverted $\mathbf{T}^l$ is similar to the guess $\mathbf{T}^l$ and so are the spectral difference measures i.e. inverted $\|\Delta\mathbf{I}_\lambda\|_1^l \approx$ guess $\|\Delta\mathbf{I}_\lambda\|_1^l$. This is shown in Figure 2.9 where both the successive model updates ($\|$inverted $\mathbf{T}^l$ − guess $\mathbf{T}^l\|_1$) (shown in green) and the successive changes in the spectral differences norms (shown in red), as given by left hand side of Equation 2.15, get smaller with increasing inversion cycle number, holding k constant. When these values stop changing, we arrive at Case 2. We call this the 'stagnancy stage' when no more information can be extracted using the same rank *pseudo-inverse*. Practically, we determine when the system has reached stagnancy stage by the following criterion:

$$\frac{\text{inverted } \|\Delta\mathbf{I}_\lambda\|_1^l - \text{guess } \|\Delta\mathbf{I}_\lambda\|_1^l}{\text{guess } \|\Delta\mathbf{I}_\lambda\|_1^0} \times 100 \quad < \quad p_1 \tag{2.15}$$

where p_1 is user-specified parameter and the criterion must be met for a few successive cycles (p_2).

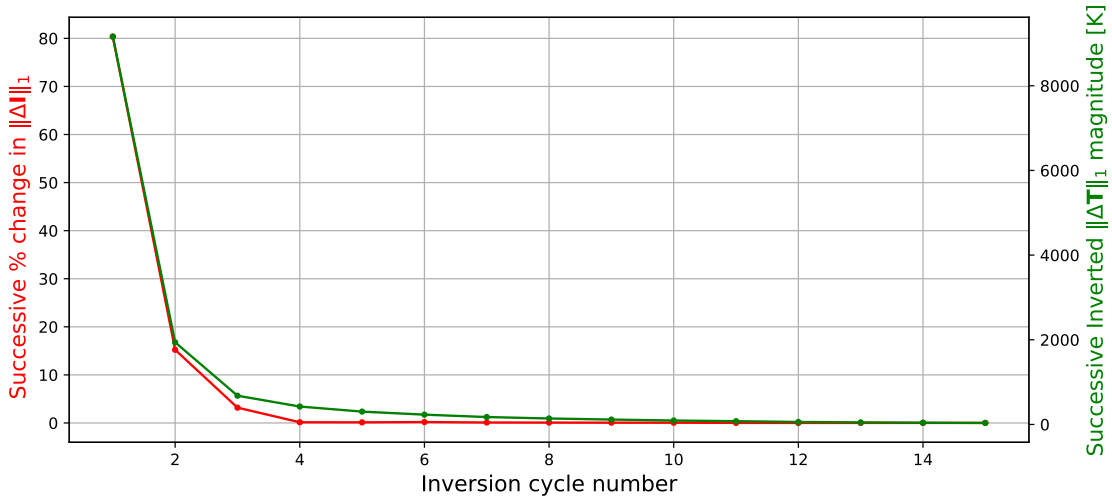

Figure 2.9: Quantities obtained when inverting perturbation in Figure 2.1 using OLA. In red, we plot the successive changes in the spectral differences with iteration using the same rank $k = 5$ (term on the left side in Equation 2.15). In green, we plot the L1 norm of inverted−guess $\mathbf{T}^l$, which corresponds to the magnitude of the successive updates when inverting using the same rank.

The latter criterion ensures that the criterion of Equation 2.15 is not met spuriously.

To obtain better inversions in subsequent cycles, we need to increase the *pseudo-inverse* rank k to allow us to construct narrower kernels to better resolve underlying perturbations and to construct kernels at a larger number of depth points. Parameters p_1 and p_2 determine how quickly the rank gets changed with cycle. Using a smaller value for p_1, combined with a larger value for p_2 is the safest bet. This extracts all information that can possibly be extracted for a given rank, making it safer to move on to the next larger rank in the subsequent cycle. But this choice comes with the cost of many inversion iterations at fixed rank. On the other hand, choosing a larger p_1 (and/or smaller p_2) can lead to error dominated unstable solutions. For our work, we set $p_1 = 0.5\%$ and conclude that the system is in stagnancy stage if it stays there for $p_2 = 3$ consecutive cycles. After establishing that the system is indeed in the stagnancy stage, we increase the rank by 2 and proceed as for previous cycles. Please note that instead of fixed rank change, we also tried changing rank based on a fixed singular value percentage difference (similar to that given by Equation 2.14) but it turns out that that approach generally results in an error dominated solutions in the later

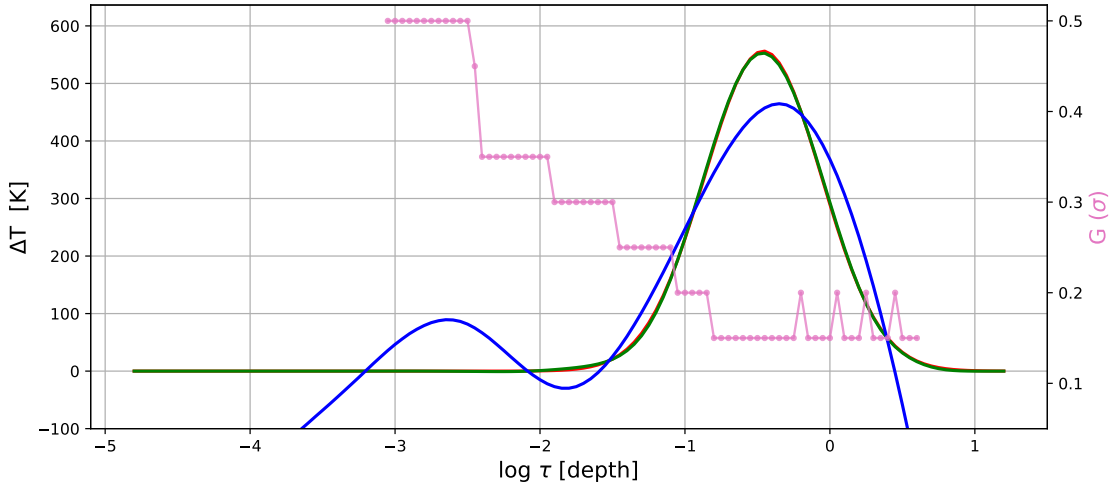

Figure 2.10: Inversion results for the perturbation in Figure 2.1 is shown here. Underlying perturbation (red) is almost perfectly covered by the iterative OLA inverted solution (green). The vertical resolution of the OLA inversions (based on the target function width) is shown by pink-dotted curve. Note that 'true' vertical resolution is slightly wider than this, and is approximately given by the convolution between the target function width and the width of the Gaussian smoothing kernel. For comparison, inversion solution obtained using SIR is shown in blue.

inversion cycles. This is because a fixed singular value percentage difference corresponds to a bigger change in k in later cycles.

Inversion iteration proceeds by successive stages of rank increase and stagnancy. If the solutions are not dominated by error, the magnitude of the higher order truncation error $\boldsymbol{\varepsilon}^l$ gets smaller with each inversion cycle as $\Delta\mathbf{T}^l$ decreases. As discussed, the rank beyond which the inversion solutions become error dominated depends on the relative magnitudes of $\mathbf{A}_{\mathrm{T}}^{\top}\bullet\ \frac{\Delta\mathbf{T}}{\mathbf{T}}^l$ and $\mathbf{C}^{\top}\bullet\ \boldsymbol{\varepsilon}^l$ over multiple depth locations. Unlike $\mathbf{A}_{\mathrm{T}}^{\top}\bullet\ \frac{\Delta\mathbf{T}}{\mathbf{T}}^l$, $\mathbf{C}^{\top}\bullet\ \boldsymbol{\varepsilon}^l$ typically does not have an upper bound, and unless $\boldsymbol{\varepsilon}^l$ is decreasing faster than the rate at which coefficient magnitudes are increasing, the inversion solution will eventually enter an error dominated regime. A scheme is needed to recognize this.

Ideally, once the inversion solutions become error dominated, this would be promptly reflected in the spectral signatures i.e. inverted $\|\Delta\mathbf{I}_\lambda\|_1^l$ gets consistently larger (fit worse) compared to the best $\|\Delta\mathbf{I}_\lambda\|_1^l$ over subsequent cycles. For such cases, the OLA inversion scheme would converge

on the optimal solution and iteration could be terminated without difficulty. But, due to the underdetermined nature of the inverse problems, it is possible that there is some lag between when the underlying model fit gets worse and when the error amplification is reflected in the spectral difference. From this work, we find cases where the inverted $\|\Delta\mathbf{I}_\lambda\|_1^l$ stays close to the best $\|\Delta\mathbf{I}_\lambda\|_1^l$, but the underlying inverted model gets significantly worse. Updating the best-model (based on minimum $\|\Delta\mathbf{I}_\lambda\|_1^l$) only when the new best inverted $\|\Delta\mathbf{I}_\lambda\|_1^l$ is significantly smaller than the last best $\|\Delta\mathbf{I}_\lambda\|_1^{l-1}$ mitigates this issue to some extent. We thus update the best-model only when the following criteria is met:

$$\left|\frac{\text{inverted } \|\Delta\mathbf{I}_\lambda\|_1^l - \text{best } \|\Delta\mathbf{I}_\lambda\|_1^{l-1}}{\text{guess } \|\Delta\mathbf{I}_\lambda\|_1^0}\right| \;>\; 0.2\ \%\ \text{ (user-defined).} \tag{2.16}$$

Once inverted $\|\Delta\mathbf{I}_\lambda\|_1^l$ is consistently larger than best $\|\Delta\mathbf{I}_\lambda\|_1^l$, we conclude that we are in the error dominated regime and we take the best-model so far as the final inversion solution. The final inversion using this iterative OLA method for the test case (shown in Figure 2.1) is plotted in Figure 2.10. The OLA inverted solution (green) recovers the underlying perturbation (red) quite well. The corresponding target function widths are shown in pink. We note that the actual width is slightly coarser than these plotted as the inverted $\Delta\mathbf{T}$ gets smoothed at the end of each inversion cycle. For comparison, SIR inversion results are shown in blue using the standard parameters stated in Appendix B.

2.2.5 Iterative OLA method: "edge-effect" issue

The Gaussian-shaped perturbation that we inverted using the OLA method in the last section, while of large amplitude, is highly idealized and localized (see Figure 2.10). The perturbation was placed in the region where averaging kernels can be readily constructed favoring successful inversion. Other more realistic perturbations present greater challenge. In particular, there may be large-scale offsets in addition to localized differences between the guess model and the real Sun (or what we call the observed/actual/underlying model in our test cases). A simple example is shown in Figure 2.11 where there is a constant offset of 300 K between the observed and the initial guess-model. This

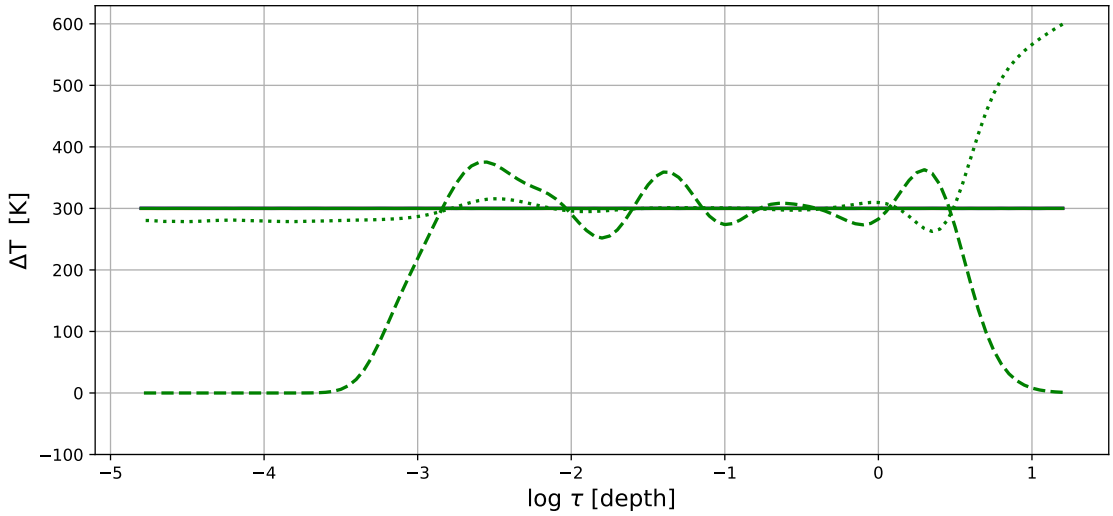

Figure 2.11: Curves for the underlying 300 K constant offset (red), SIR-only inverted solution (blue) and HOLA inverted solution (green) lie on top of each other. HOLA inverted solution, with flat kernel approach of Section 2.2.5, is shown by green-dotted line, and that obtained using iterative OLA-only method is shown by the green-dashed curve.

constant offset perturbation is trivial for SIR to recover, as the global nodal solution readily matches large-scale trends. Iterative OLA method (green-dashed), on the other hand, struggles to arrive at a suitable solution. It displays large oscillations throughout the inversion window.

The failure of OLA to invert for large-scale perturbations has two underlying and intertwined causes: the OLA inversions are confined to a well defined inversion window outside of which no inversion updates are made and the averaging kernels are not delta functions, they have finite widths, so the iterative solution near those edges is effected by $\Delta\mathbf{T}$ from the non-updated regions. As a global solver SIR extrapolates the solution to regions where there is little spectral information. Iterative OLA instead contaminates the solution within the inversion window by $\Delta\mathbf{T}$ outside this window. This is only partially mitigated by the solution smoothing we employ between iterations.

To illustrate this, assume that as we iterate we do not smooth inverted $\Delta\mathbf{T}$ and keep the rank fixed. This means that the OLA inversion window doesn't change much with iteration and only the region inside this window gets updated. After a few inversion cycles, the guess $\Delta\mathbf{T}^l$ inside this window would get smaller, while that outside the inversion window remains unchanged. The results

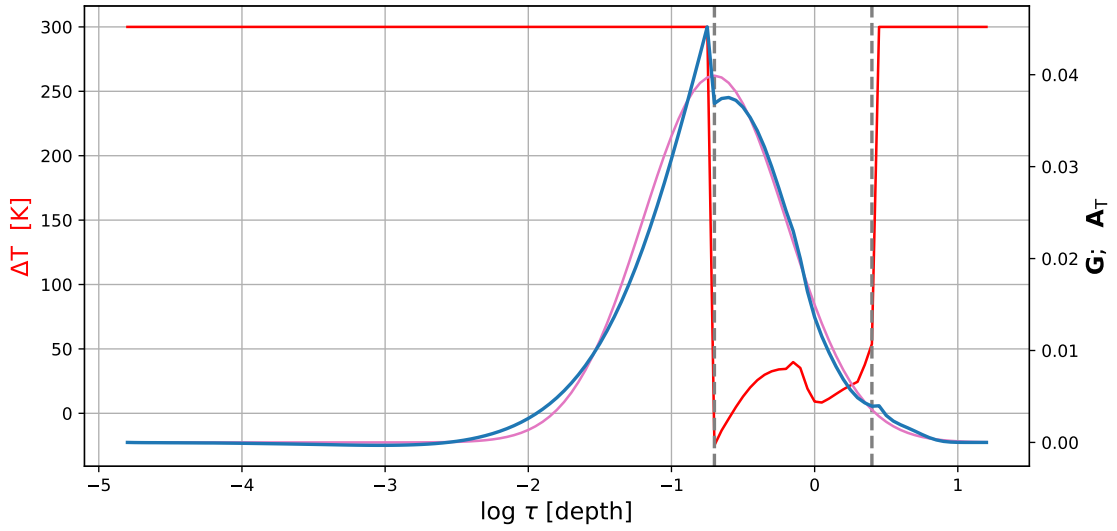

Figure 2.12: This plot demonstrates the 'edge-effect' issue when iteratively inverting 300 K constant offset using OLA. Guess $\Delta\mathbf{T}$ in the 2nd inversion cycle is shown in (red). Vertical dashed lines mark the OLA inversion boundary. Blue and pink curves correspond to the target function and averaging kernel constructed near the left edge of the inversion window.

of such an inversion are plotted in Figure 2.12 with the inversion window marked by the vertical dashed lines. In the subsequent inversion cycles, the inversion solutions within the inversion window but close to either boundary disproportionately respond to $\Delta\mathbf{T}^l$ outside the inversion window. The contribution of the averaging kernel acting on $\Delta\mathbf{T}^l$ outside the window contributes an increasingly larger amount to the update compared to that inside the window, with each iteration. This means that as we iterate, there is a leakage of information from the outside of the inversion window to the inside. This defeats the very purpose/strength of OLA, a method that aims to prevent such leakage by focusing on keeping the information where it belongs.

To get around this 'edge-effect' issue, we tried using non-symmetrical target functions e.g. part of the target functions outside the inversion window is set to 0 so that the target function is only half-Gaussian; skewed target function to have more sensitivity to regions inside the window. But given that it is usually not possible to construct kernels that 'perfectly' fit these target functions, the issue of information leakage remained. We realized that it might be favorable to approach this issue from the other direction i.e. make inversion updates in the regions outside the OLA

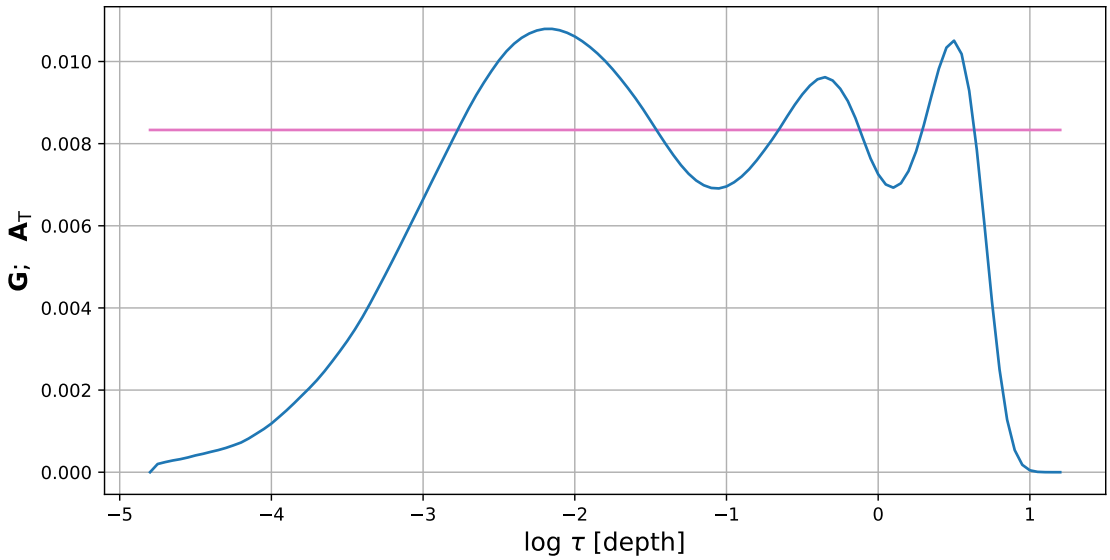

Figure 2.13: Flat target function with area normalized to 1 is plotted in pink and the corresponding 'flat' averaging kernel is shown in blue. Note that rank $k = 5$ is used when constructing the kernel.

inversion window, in any given cycle. This can be done by making large-scale inversion updates (at all locations) along with the localized OLA inversions. For this, we initially came up with a scheme within the OLA framework where we used flat/constant (normalized) target functions (shown by the pink curve in Figure 2.13) to construct flat averaging kernels that are approximately equally sensitive to all depth locations. If we could construct such a perfectly flat averaging kernel, then $\mathbf{C}^{\top}\bullet\ \mathbf{\Delta I}$ would correspond to a large-scale average fractional value given by $\left\langle \frac{\mathbf{\Delta T}}{\mathbf{T}} \right\rangle = \mathbf{A}_{\mathrm{T}}^{\top}\bullet\ \frac{\mathbf{\Delta T}}{\mathbf{T}} \equiv \frac{1}{N_\tau}\sum_{\tau}\frac{\Delta \mathrm{T}}{\mathrm{T}}(\tau)$, where N_τ is the number of optical depth points (assuming error contribution is negligible). Even though the flat averaging kernels constructed (Figure 2.13 for rank $k = 5$, blue) are approximate only, not perfectly flat, this method showed promise. We interleaved large-scale inversion updates, computed using flat kernels, between the high-resolution localized OLA inversions during iteration. The final inversion solution for the 300 K perturbation from this combined effort is shown in Figure 2.11 (green-dotted). The inversion is significantly improved.

Some difficulties remain however. The main issue is that the large scale inversion component is a fractional average $\left\langle \frac{\mathbf{\Delta T}}{\mathbf{T}} \right\rangle$ from which we compute the the actual inverted $\Delta \mathrm{T}(\tau_i)$ at each depth

using $\Delta T(\tau_i) = \left\langle \frac{\Delta \mathbf{T}}{\mathbf{T}} \right\rangle \times T(\tau_i)$. Since $T(\tau_i)$ in the deeper regions is about 3-5 times larger than the shallower region temperatures, the large-scale inversion corresponds to over-corrected solution in the deeper regions and under-corrected in the shallower regions (see Figure 2.11). Moreover, because of this bias, it is harder for this approach to recover large-scale perturbations that get more negative with increasing depth (perturbation slope is negative). It might make more sense to use normal non-fractional response functions instead, to compute constant inverted $\mathbf{\Delta T}$ directly. But, depending on the perturbation shape, these suffer similar issues. No one method that we have yet tried that worked well in all cases.

2.2.6 Preliminary hybrid OLA (HOLA) method: SIR + OLA

Instead we pursued a hybrid SIR+OLA approach. To recover any large-scale constant and linear trend, we employ SIR with limited temperature nodes (see Appendix B). Given that OLA method excels in doing high-resolution localized inversions while SIR excels in recovering large-scale offsets, a combined inversion method leads to a much better inversion solution. We called this combined inversion method the HOLA (hybrid-OLA) method. Note that we assumed that the large-scale trends are mostly linear with log τ and letting SIR invert this linear trend should be sufficient. The underlying perturbations in real world scenario do not have to be linear in which case HOLA using SIR large-scale inversion may struggle (see Chapter 3 and 4 for details). What we present here is not the final solution and we suggest possible future extensions in Chapter 6.

In implementation, each HOLA inversion iteration cycle has two subparts: we first use SIR to make large-scale linear updates to the 'starting' guess-model (for a given cycle) and then use this large-scale updated inverted-model as input for the OLA method (in the same cycle) to do high-resolution inversions. The assessment of which spectral difference case (see Section 2.2.4.1) the inversion solution falls into and whether to update the rank or not is based on the combined effort of SIR+OLA in each cycle. To be consistent with a single variable inversion, when inverting a variable using SIR, even when the cross-talk variables may have non-zero inverted value, we manually set

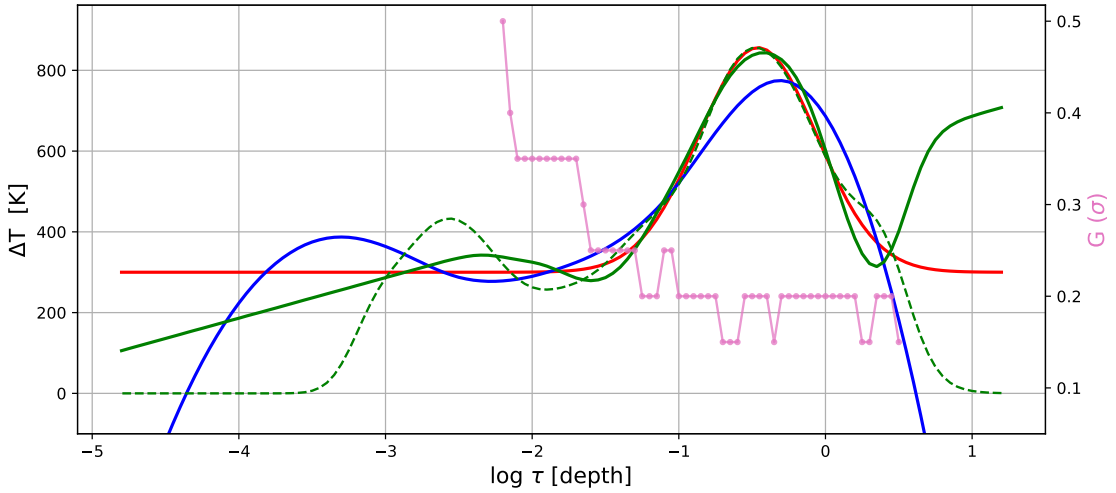

Figure 2.14: Inversion results for Gaussian shaped localized perturbation + constant 300 K offset. The underlying perturbation is shown in red, HOLA inverted solution in green, iterative OLA-only inverted solution in green-dashed and SIR-only inverted solution in blue. The width of the target function vs. depth of the OLA inverted solution (within HOLA framework) is shown in pink.

this update to 0 e.g. when inverting temperature, we also have to invert for $\mathbf{P}_e$ (otherwise SIR assumes *hydrostatic equilibrium*) which might lead to non-zero inverted $\Delta\mathbf{P}_e$. So, to be consistent with a single variable $\mathbf{T}$ inversion, we set this $\Delta\mathbf{P}_e$ to 0 in the inverted solution.

The inversion result using HOLA for the constant 300 K offset is shown in green in Figure 2.11. Given SIR can perfectly recover a linear perturbation in temperature by itself, the HOLA results overlay the SIR results exactly. Inversion results for a more complicated case are shown in Figure 2.14. The underlying perturbation is a sum of the two test cases discussed above and has both, a large-scale trend and a localized perturbation. None of these inversions are fully satisfactory. While SIR (blue) can robustly recover large-scale atmospheric structure, it has trouble with small-scale perturbations. Conversely, HOLA (or iterative OLA by itself), shown in green and green-dashed, does an excellent job recovering small-scale structures but struggles with large-scale offset. The full potential of HOLA requires a more robust solution to the edge-effect. We outline what that might look like in Chapter 6.

2.2.7 OLA Inversion in the presence of observational noise

The error $\boldsymbol{\varepsilon}$ in 1st order equation 2.5 discussed so far corresponds to the omitted higher order contributions to the spectral response as we assume linear relationship between $\Delta\mathbf{I}$ and $\Delta\mathbf{T}$. These are significant when the perturbation magnitudes are not small. Real-world observations are additionally corrupted by the uncertainties in measurements. These uncertainties (sources of noise) can be due to photon noise, sky background noise, and detection noise [23, p. 96]. In addition to these 'random' noise sources, systematic error also occurs. We do not consider the later.

To investigate its effect we model random noise at each wavelength as a Gaussian distribution, centered at 0 and with width based on the noise level (1/signal-to-noise ratio) of the instrument. This mimics continuum measurements (real-world observations) which are approximately Gaussianly distributed. For a given noise-level σ_c (continuum intensity noise-level) and observed intensity I_λ (HSRA normalized, [18]), the noise-level σ_λ for a given wavelength λ is given by $\sigma_\lambda = \sqrt{I_\lambda} \times \sigma_c$. An example case is shown in Figure 2.15 where we plot the SIR synthesized 'observed' intensity, for the test case model in Figure 2.10, with added random noise $\sigma_c = 1\%$. The random noise is shown in blue and for comparison, the higher-order error term is overplotted in yellow. It is clear that the higher order error varies smoothly with wavelength while the random noise is erratic. Both, in this example, have similar amplitudes.

These errors are collectively represented with $\boldsymbol{\varepsilon}$ in the 1st order equation 2.5 even though they have completely different origins. The higher order error is implicit to the system and comes in because the unknown perturbations we are solving for has finite amplitude (1st order equation is not perfect), while the random photon noise is explicit and is a part of the observed spectra (and the spectral differences $\Delta\mathbf{I}$). Our goal here is to demonstrate that spectral noise leads to a worse quality inversion, as compared to when no spectral noise is present. For this we invert the Gaussian perturbation test case (Figure 2.10) in the presence of noise level $\sigma_c = 1\%$ using the iterative OLA method. Note that here we chose iterative OLA, and not HOLA, because to demonstrate the effect of observational noise on inversion result, it is important to pick a case where the spectral noise is

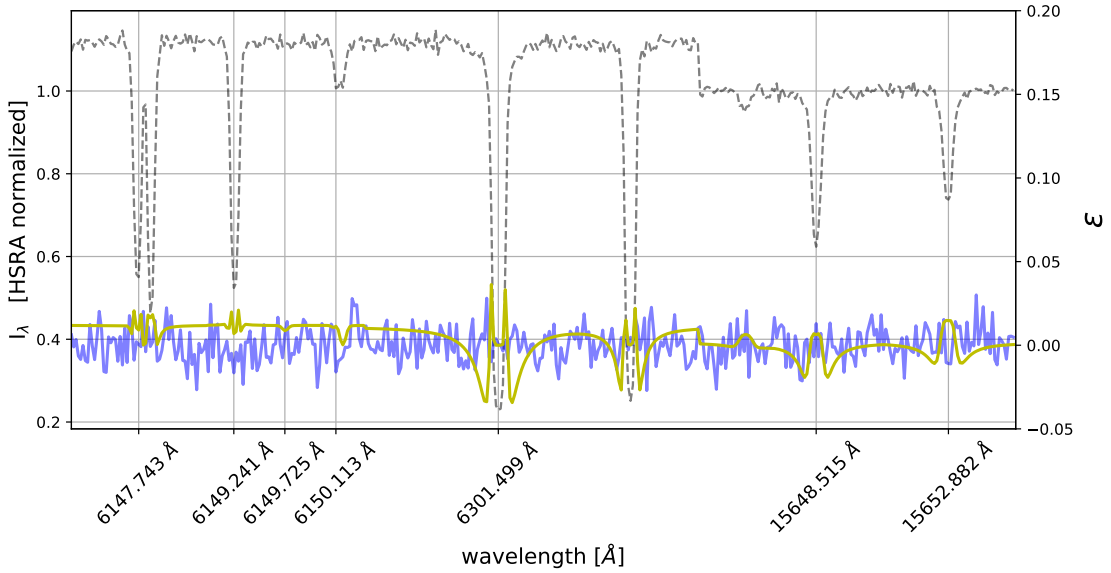

Figure 2.15: Synthetic Stokes **I** through the artificially constructed test case in Figure 2.1, with added spectral noise (noise-level = 1%), is shown in gray-dashed. The underlying spectral noise is shown in blue and error from the neglected higher order terms is shown in yellow. Note that the scaling on the right side of the figure correspond to the errors terms.

the limiting factor in determining the quality of inversion. The current version of the HOLA method is to some extent limited by the 'edge-effect' issue and is thus not suitable for this demonstration.

When carrying out iterative OLA inversions in the presence of spectral noise, $\Delta\mathbf{T}$ gets smaller with each subsequent inversion cycle (assuming inversion updates are in the 'right' direction). This results in a decrease in the magnitude of the higher order terms, while the spectral noise magnitude remains constant. Thus the overall magnitude of $\boldsymbol{\varepsilon}$ is getting smaller allowing us to use larger rank k for a higher resolution inversion in subsequent cycles. The iteration finally stops when the difference between the spectra from the observed and the inverted model approximates the spectral noise. This means that we have arrived at the spectral noise floor and that no further information can be extracted. Any attempt to better fit the spectra by using larger rank k would likely result in an error dominated solution fitting the spectral noise.

Mathematically, as already mentioned, it is the balance between $\mathbf{C}^\top \cdot \boldsymbol{\varepsilon}$ and $\mathbf{A}_\mathrm{T} \cdot \frac{\Delta\mathbf{T}}{\mathbf{T}}$ that ultimately decides the largest k (and the best resolution) achievable by the system and when the

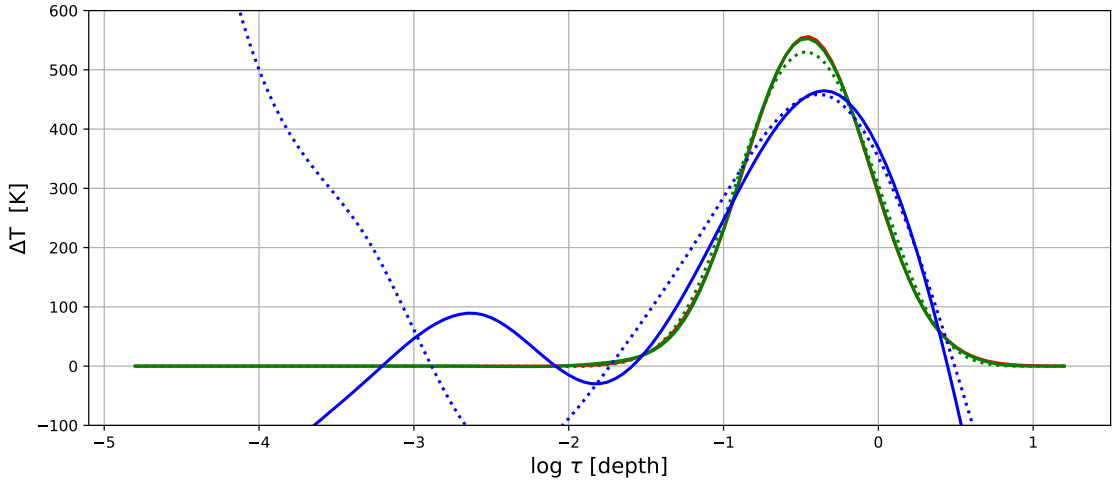

Figure 2.16: Iterative OLA inversion results for the perturbation in Figure 2.1. Green-solid curve corresponds to inversion in the presence of no spectral noise and overlays the underlying perturbation (red). Corresponding result with 1% noise-level is shown by the green-dotted line. For comparison, SIR inversion results for the corresponding cases are plotted in blue.

inversion enters error dominated regime. With added spectral noise, the system enters a noise dominated regime at a smaller rank k compared to if there were no spectral noise. The larger the noise-level, the larger is the amplitude of $\boldsymbol{\varepsilon}$ and the smaller the value of k beyond which solution will be noise dominated. Thus the presence of spectral noise can degrade the quality of the inversion that would be otherwise achievable when no noise is present. Nonetheless, high quality inversions are possible. This is shown in Figure 2.16 where we plot iterative OLA inversion results in the presence of varying noise-levels: σ_c = no noise (green) and 1 % (green-dotted). It is evident from the plots that the overall inversion quality is somewhat degraded in the presence of noise.

2.3 Summary

In this chapter, we applied the OLA inversion method to the spectroscopic data. We discussed the basic methodology, challenges faced and how we met those challenges. To keep things simple, we restricted the discussion to single variable temperature inversions.

We started with discussing how inversions are carried out in general. As discussed in Sec-

tion 2.1, the basic approach is to start with an initial guess-model and solve for the depth dependent model differences ($\Delta\mathbf{T}$ or $\frac{\Delta\mathbf{T}}{\mathbf{T}}$), between the underlying model (that we intend to recover) and the guess-model, that accounts for the corresponding spectral differences $\Delta\mathbf{I}$. Spectral differences $\Delta\mathbf{I}$ and model differences $\Delta\mathbf{T}$ are related to each other by linear response functions $\mathbf{R}_{\mathrm{T}}$. For a set of wavelengths (that makes up the spectral lines) the relationship can be written as a 1st order linear system of Equations 2.5. This system is approximate and has error $\boldsymbol{\varepsilon}$ contributions from the omitted higher order sensitivity terms (and spectral noise, if present).

In order to solve this system of equations for $\frac{\Delta\mathbf{T}}{\mathbf{T}}$, we need to compute the inverse of the response function matrix $\mathbf{R}_{\mathrm{T}}$. This is a highly non-trivial task as the matrix equation belongs to a severely ill-posed category. This is due to redundancy in the spectral line formation which results in the response functions (that make up the matrix) to have 'similar' sensitivity information. Ill-posedness of the system, combined with non-zero error (mathematically means that $\Delta\mathbf{I}$ is not in the range of $\frac{\Delta\mathbf{T}}{\mathbf{T}}$), results in the actual number of linearly independent equations to be much smaller than the total number of unknowns ($\frac{\Delta\mathbf{T}}{\mathbf{T}}$). The system is underdetermined and it is not possible to uniquely solve for $\frac{\Delta\mathbf{T}}{\mathbf{T}}$. Ill-posedness further means that the numerical rank of the matrix is ill-determined and naively using the normal equations method to compute its *pseudo-inverse* (approximate inverse) will likely result in an inverse matrix with large amplitudes that amplify the error $\boldsymbol{\varepsilon}$, resulting in error dominated solutions. These error dominated solutions are in general highly oscillatory and lack physical meaning.

In order to obtain a physically meaningful solution, we rely on regularization, employing a lower rank *pseudo-inverse* to compute $\frac{\Delta\mathbf{T}}{\mathbf{T}}$. Lower rank *pseudo-inverse* matrix doesn't have contributions from smaller magnitude singular values (of the $\mathbf{R}_{\mathrm{T}}$ matrix) which otherwise lead to larger magnitude terms in *pseudo-inverse*. The caveat here is that the 'amount' of regularization dictates the 'quality' of solution achievable. Regularizing 'too much' by removing too many smaller singular values (or eigenmodes) results in smoother solutions which might fail to recover sharp gradients in the underlying perturbation (if present). On the other hand, solutions obtained be regularizing 'too little' by keeping too many smaller singular values are better equipped to recover

sharp gradients, but are more likely to be error dominated. Determining the 'optimal' regularization parameter to balance resolution vs. error amplification is one of the hardest tasks when carrying out inversions. This is because the spectral difference metric with which we assess how close the inverted solution is to the underlying perturbation is degenerate. Different regularization parameters lead to widely varying solutions with similarly 'good' fit observed spectra.

In the current state of the art spectropolarimetric inversion method SIR, globally smooth solutions are obtained by inverting at a limited number of user-defined node locations. This ensures that the inverted solutions are non-oscillatory below nodal scales. The number of nodes is decided based on user experience and dictates the resolution (in depth) of the inverted solution. In MURaM simulations of the Sun, we find atmospheric columns with sharp gradients at scales much smaller than those that can be recovered using the standard SIR node values. Further, it is likely that SIR inverted solutions do not correspond to the 'true resolution limit' achievable using spectral data that will be provided by the upcoming DKIST. Determining the 'best/true' inversion resolution limit that is achievable at each depth (given the data), and be able to invert at that resolution is critical.

We introduced the general methodology of the OLA method in Section 2.2 in context of inverting for single variable temperature perturbations for artificially constructed test cases. The method aims to find the most localized inversion solution at 'each' depth location. This is achieved by solving for linear coefficients $\mathbf{C}$ (using Equation 2.9) such that the linear combination of response functions (in $\mathbf{R}_{\mathrm{T}}$) using these coefficients leads to averaging kernel ($\mathbf{A}_{\mathrm{T}}$) that is 'most' localized at that depth. The inner product of the linear coefficients with $\mathbf{\Delta I}$ then gives the desired inversion solution at this depth and corresponds to the depth averaged value of $\frac{\mathbf{\Delta T}}{\mathbf{T}}$, weighted by $\mathbf{A}_{\mathrm{T}}$ (assuming solution is not dominated by error). Thus, the width of the kernel dictates the spatial resolution (vertical) of the obtained solution at that depth. The process is then repeated for each depth to invert at 'all' depth locations.

OLA inversion is usually not achievable at all depths as the 'amount' of orthogonal sensitivity information in the response function matrix is non-uniformly distributed across depths. Failure

usually occurs above and below a limit range of depths, defining the 'OLA inversion window'. The width of this window and the corresponding kernel widths (resolution) depends on the rank used when solving Equation 2.9. A smaller rank will result in a narrower inversion window (with wider kernel widths at each depth), while a larger rank would result in a wider inversion window (with narrower kernel widths at each depth) with the caveat that solutions are now more likely to be dominated by error contributions. Thus the inherent question of what rank to use (or how much to regularize) still remains.

In Section 2.2.4, we developed an iterative-OLA method that gets around the above issue by 'slowly' arriving at the most optimal rank achievable given the data. This also allows us to invert non-linear (large-amplitude $\frac{\Delta \mathbf{T}}{\mathbf{T}}$) perturbations using linear response functions, extending the inversion capability of the traditional OLA method. Iterative-OLA struggles to recover perturbations that have large-scale offsets. This has to do with the fact that OLA inversion window does not span the entire depth domain, and that averaging kernels are not δ-functions. Iteratively updating regions inside the inversion window eventually results in a 'leakage' of information ($\frac{\Delta \mathbf{T}}{\mathbf{T}}$) from outside the window to inside which may corrupt the entire OLA inversion solution. We called this the 'edge-effect' issue. This issue defeats the very strength of OLA which aims to prevent such leakage by minimizing cross-talk error from other depth locations by trying to construct narrow width averaging kernels.

In Section 2.2.6, we discussed a preliminary workaround to the 'edge-effect' issue by employing a hybrid SIR+OLA approach (HOLA method). The edge-effect is a result of our inability to make updates outside the OLA inversion window for which there might be non-zero $\frac{\Delta \mathbf{T}}{\mathbf{T}}$ perturbations. We mitigated this issue by interleaving SIR large-scale updates (constant/linear) at all depths, in between OLA high-resolution small-scale updates. This works well if the underlying large-scale offset is constant/linear with depth, but may fail otherwise. In MURaM simulations we find atmospheres that differ from this assumption. Finding a more robust solution to the edge-effect issue to successfully invert non-linearly shaped large-scale perturbations is future endeavor. We suggested a few ways in which this might be accomplished in Chapter 6.

Chapter 3

Statistical assessment of single variable HOLA inversions using MURaM atmospheres

In this chapter we statistically assessed the capability of the HOLA method to do single variable $\mathbf{T}$, $\mathbf{P_e}$ and $\mathbf{V_{los}}$ inversions and compared them to that obtained using SIR method. Given the underdetermined nature of the inverse problems, it is hard to assess the 'true' inversion quality solely based on the spectral difference measures, as multiple, widely differing atmospheres exist that can lead to similarly good-fit observed spectra. A true assessment should be based on how well the inverted model matches the underlying model. Given that this is not possible in real-world scenario, as the underlying atmosphere is not available, we inverted for simulated MURaM atmospheres [51, 52, 63] which reproduce many properties of the solar photosphere [13, 14, 40].

MURaM is a radiative magnetohydrodynamics (MHD) numerical code that simulates upper solar convection zone and photosphere. The code solves the MHD equations i.e. continuity equation, momentum equation, energy equation and the induction equations in three dimensions, and solves the radiative transfer equation under LTE assumptions. The simulation data used in this thesis corresponds to small-scale dynamo quiet-Sun simulation (run *O16b*, as described in [51]). The overall domain size of the simulation is $6 \times 6 \times 4$ Mm^3 with 16 km grid spacing, and has vertical domain size extending to 1.7 Mm above the photosphere. It spans about 1 hour solar time with about 2 second cadence time series yielding a total of 1801 data cubes for each atmospheric variable.

A statistical assessment of the inversion quality requires inverting a 'sufficiently' large number of widely differing atmospheres. Here, in order to satisfy this criteria and be able to invert the

atmospheres in a reasonable amount of time, we obtained widely differing atmospheres from a MURaM 3D data cube, at a single time. For simplicity, we picked the atmospheres that correspond to the central row and column (those passing through the central horizontal pixel) in the data cube, a total of 767 atmospheres. The intention was to analyze a representative sample.

3.1 Converting MURaM atmospheric columns into SIR compatible format

MURaM atmospheres are computed on a geometrical depth scale i.e. constant Δz grid [km]. Given that we used forward solving capabilities of SIR to synthesize spectra (and compute response functions), and SIR capabilities are used in HOLA to recover large-scale perturbations, we first need to convert MURaM atmospheres from a constant Δz grid to SIR compatible constant $\Delta \log \tau$ grid. To facilitate this, we used a subroutine within the SIR framework, which, under LTE assumptions, uses the local values of T and P_e (at a given z) to compute the level populations and thus $\lambda = 500$ nm opacity at each depth. Then, starting at the top of the atmosphere, where we assume $\tau = 0$, we integrate down to compute the optical depth $\tau(z)$ at each depth. Using this non-uniform $\tau(z)$, we interpolate the value of each of the MURaM atmospheric variable to SIR compatible, uniformly spaced $\Delta \log \tau$ grid. In this work, we took $\log \tau \in [-4.8, 1.2]$ as representative of the solar photosphere. We used a standard SIR grid-spacing of $\Delta \log \tau = 0.05$, resulting in a total of 121 $\log \tau$ depth points.

Using the above mentioned approach, we converted each of the 767 MURaM atmospheres to SIR compatible format. From these, we computed depth-dependent mean (on constant $\log \tau$ grid) for each variable to get mean MURaM atmosphere, which is used as the starting guess-model in this thesis. Note that this mean atmosphere is assumed to be stationary i.e. $\mathbf{V_{los}}$ in this model is manually set to 0.

3.2 Statistical assessment of the inversions results: Basic approach

The assessment of the capabilities of HOLA (and SIR) for single variable inversion goes as follows: before inverting a given MURaM atmospheric column (in SIR compatible format), we first

set the cross-talk variable difference between the underlying atmosphere and the guess-model to 0 e.g. if we intend to invert $\mathbf{T}$, then the value for $\mathbf{P_e}$ and $\mathbf{V_{los}}$ for the given atmosphere is set to that of the guess-model. This is done to make sure that the observed and guess-model spectral differences are only due to differences in the given variable being inverted, consistent with single variable inversions. We then use SIR forward solver to compute the observed spectra from the given atmosphere and invert it using the HOLA method as described in previous chapter (see Section 2.2.6). Note that inversions here are done in the absence of spectral (photon) noise.

Inversions are done for each of the 767 MURaM atmospheres. Using these, we computed depth dependent statistics - the mean and standard deviation of the absolute difference between the underlying and inverted variable at each depth. Depths with small mean (and small standard deviation) correspond to locations where the inversion methods, on average, do a good job at recovering the underlying perturbation. On the contrary, depths were mean (or standard deviation) is large, corresponds to locations where the method struggles. This approach allows us to assess the capabilities of the methods to recover individual MURaM columns from the mean MURaM starting guess-model. For comparison, we obtained similar statistics for SIR-only inversion results (see Appendix B for the SIR node values used for different cases).

3.3 Inverting MURaM Atmospheres

3.3.1 MURaM T inversion results

In Figure 3.1 we show the statistical assessment plot for temperature inversions. Here, HOLA inversion statistics is shown in green, with the mean shown by green-solid curve, while the boundary of the green-shaded region mark the ± 1 standard-deviation region around the mean curve. For comparison, similar plot is shown for SIR inverted solutions in blue.

Statistically, both methods do well in the $\log \tau \in [-1.5, 0.75]$ region. The mean and standard deviation of the difference in this region correspond to 1% of the local T value. Good performance is expected in this depth range as there the temperature response functions have the most orthogonal

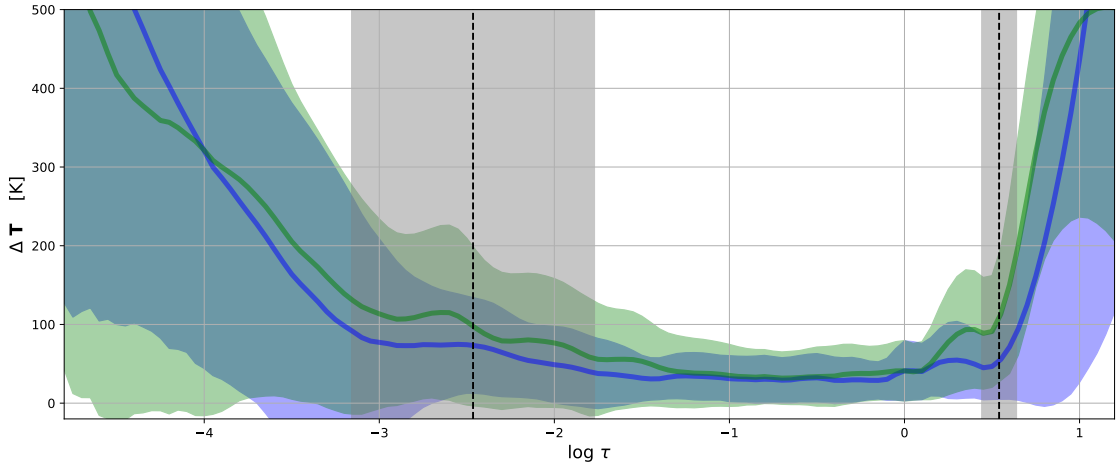

Figure 3.1: Statistical assessment plot for MURaM **T** inversion done using HOLA (green) and SIR (blue). The green-solid line correspond to the depth dependent mean of the absolute value of the difference between HOLA inverted and underlying MURaM **T**, while the boundary of the shaded region signify the ±1 standard-deviation around the mean. Similar plot computed for SIR is shown in blue. The black vertical dashed lines mark the mean location of the edge of the OLA inversion window (in final cycle, within HOLA framework) and the gray shaded region mark the ±1 standard-deviation spread of this edge around the mean location.

sensitivities of the spectral range we are using. As we move away from of this region (both towards deeper and shallower regions), the quality of inversion deteriorates because of the lack of spectral line sensitivity to these regions. Further, the HOLA method additionally struggles with the 'edge-effect' as, unlike our test cases where we assumed linear large-scale perturbation shapes, the shape of the large-scale perturbations in MURaM atmospheres can be non-linear with log τ. The vertical dashed lines mark the average boundary location of the OLA inversion window in the final inversion cycle (within HOLA framework). The gray shaded region mark its ±1 standard deviation spread. These locations are where we would expect the "edge-effect" error to affect (on average) HOLA inversion results the most. We note that error from the 'edge-effect' is not confined around this boundary but may affect the entire inversion solution.

In Figure 3.2 we show inversion results for a few handpicked cases to demonstrate the strengths and weaknesses of the HOLA (and SIR) inversion methods. In these plots, the red curve corresponds to the underlying $\Delta\mathbf{T}$ perturbation we intend to recover, the green corresponds

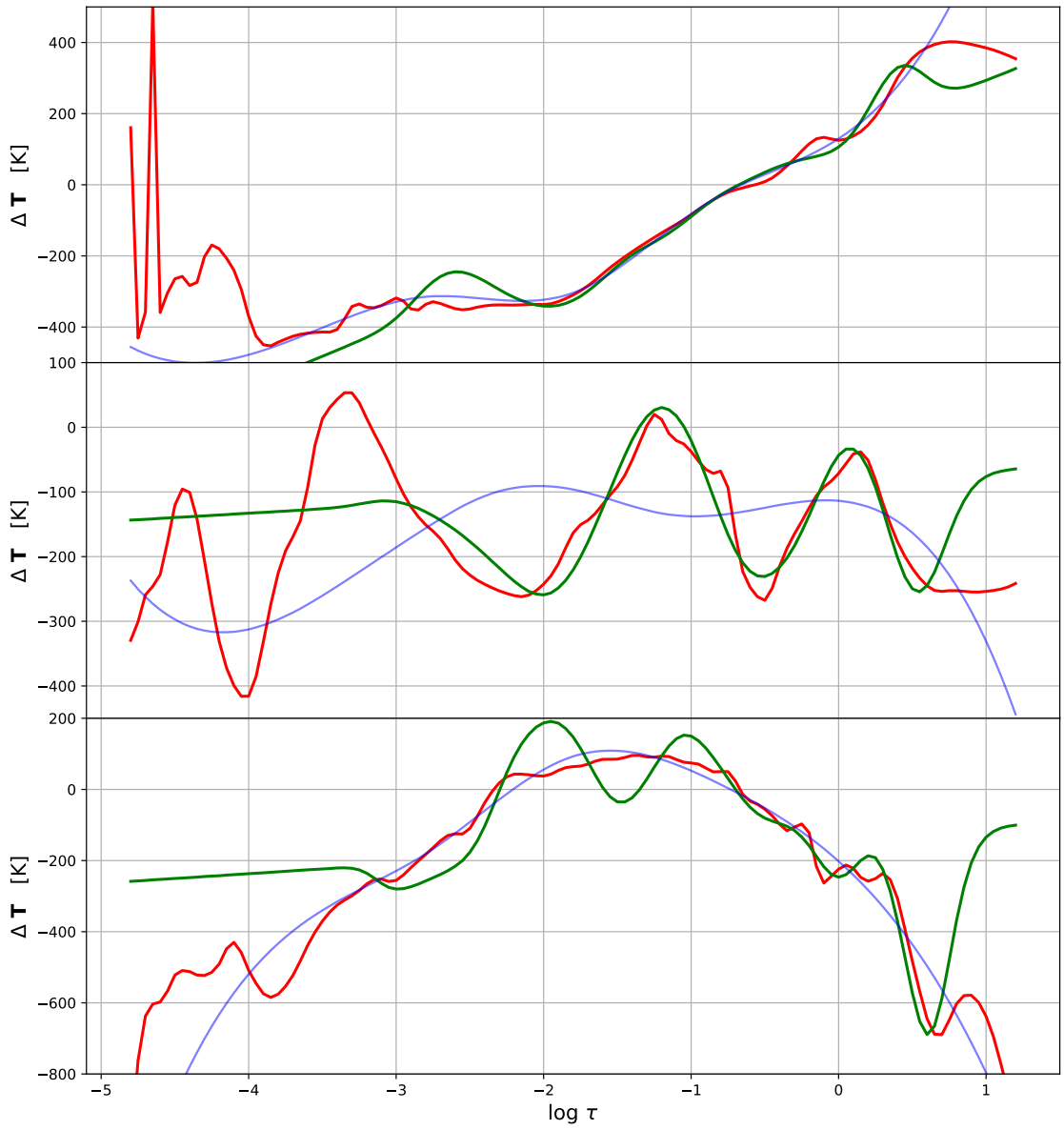

Figure 3.2: $\Delta\mathbf{T}$ inversion results for three handpicked MURaM cases. In each plot, underlying perturbation is shown in red, HOLA inverted solution is shown in green, and SIR-only inverted solution is shown in blue.

to HOLA inverted $\Delta\mathbf{T}$ and the blue corresponds the SIR-only inverted $\Delta\mathbf{T}$. The closer the HOLA (or SIR) solutions are to the underlying perturbations, better is the inversion solution. The top plot corresponds to an approximately linear perturbation where both HOLA and SIR do a good job at recovering the perturbation. The true strength of the HOLA method is demonstrated in the middle plot where the method is able to recover the large-scale constant offset and the higher spatial frequency perturbation. The bottom plot demonstrates the case where the HOLA inversion solution is dominated by the edge-effect error because of the current design limitations. The large-scale perturbation is approximately quadratic in shape which cannot be recovered by SIR linear updates (within HOLA framework). On the other hand, SIR-only inversion method successfully recovers a smoother version of the underlying perturbation.

It might be reasonable to consider that recovering large-scale perturbation of any order using SIR (within HOLA framework), by using larger node values, might fix the edge-effect issue. The problem with that approach is that SIR tends to find solutions that minimize the spectral difference, and once we arrive at a solution for which $\Delta\mathbf{I} \rightarrow 0$, it is difficult to make further updates to the inversion solution. This means that given the underdetermined nature of the inverse problems, the path taken is of great importance e.g. whether we aim to obtain a globally smooth solution or an optimally localized solution, both approaches could lead to a well fit observed spectra but the underlying solutions may be very different, and it is impossible to know which is correct in any given case.

3.3.2 MURaM $\mathbf{V_{los}}$ inversion results

In this section, similar to temperature inversions, we discuss inversion results for the line-of-sight velocity ($\mathbf{V_{los}}$) using the HOLA and SIR-only methods. The 1st order equation when inverting $\Delta\mathbf{V_{los}}$ is given by

$$\Delta\mathbf{I} \;=\; \mathbf{R}^{\top}_{\mathrm{V_{los}}} \cdot \frac{\Delta\mathbf{V_{los}}}{\mathbf{c_s}} \;+\; \boldsymbol{\varepsilon} \tag{3.1}$$

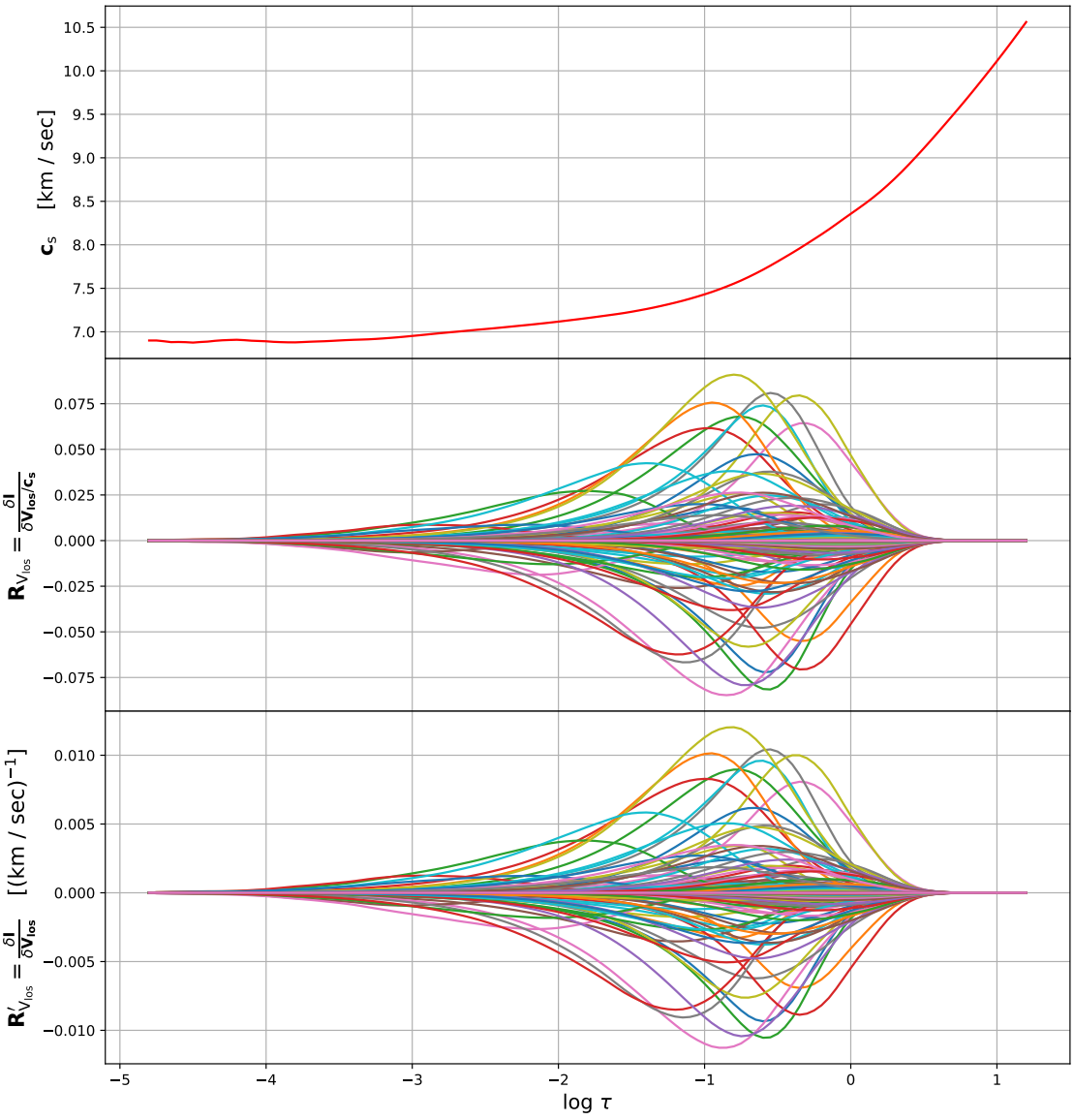

Figure 3.3: (Top plot) Sound-speed $\mathbf{c_s}$ vs log τ. (Middle plot) Fractional $\mathbf{V_{los}}$ response functions: $\mathbf{R}_{\mathrm{V_{los}}} = \frac{\delta \mathbf{I}}{\delta \mathbf{V}_{\mathrm{los}}/\mathbf{c_s}}$. (Bottom plot) Dimensional $\mathbf{V_{los}}$ response functions: $\mathbf{R}'_{\mathrm{V_{los}}} = \frac{\delta \mathbf{I}}{\delta \mathbf{V}_{\mathrm{los}}}$.

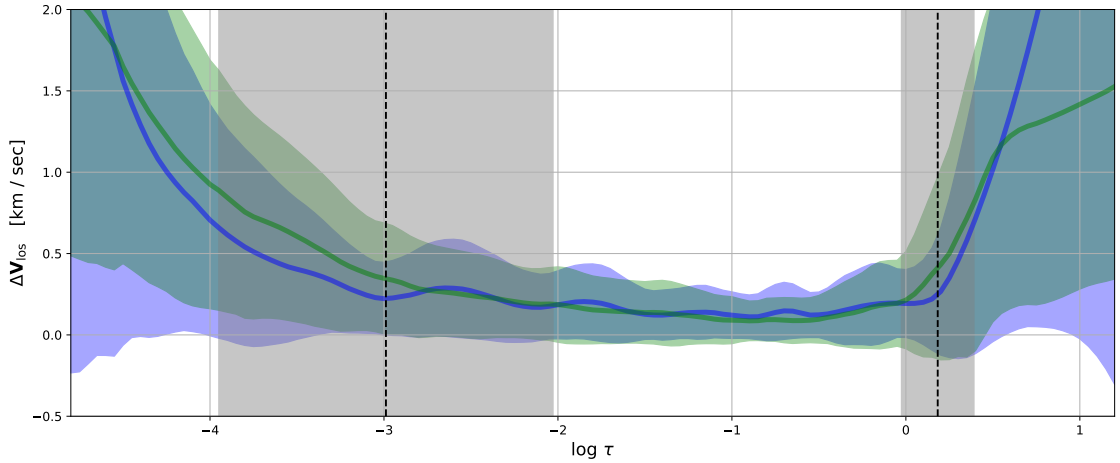

Figure 3.4: Statistical assessment plot for MURaM $\mathbf{V_{los}}$ inversion done using HOLA (green) and SIR (blue). The green-solid line correspond to the depth dependent mean of the absolute value of the difference between HOLA inverted and underlying MURaM $\mathbf{V_{los}}$, while the boundary of the shaded region signify the ± 1 standard-deviation around the mean. Similar plot computed for SIR is shown in blue. The black vertical dashed lines mark the mean location of the edge of the OLA inversion window (in final cycle, within HOLA framework) and the gray shaded region mark the ± 1 standard-deviation spread of this edge around the mean location.

Here, $\Delta \mathbf{V_{los}}$ is the difference between the underlying atmosphere and the guess-model $\mathbf{V_{los}}$, while $\mathbf{R}_{\mathrm{V_{los}}}$ corresponds to the fractional response functions for $\mathbf{V_{los}}$ (middle plot in Figure 3.3). The adiabatic sound speed $\mathbf{c_s}$ is used to compute non-dimensional $\mathbf{V_{los}}$ fractional response functions, as $\mathbf{V_{los}}$ can be 0.

Single variable HOLA inversion for $\mathbf{V_{los}}$ is done similar to that described for temperature in Section 2.2.6, with the SIR node values chosen accordingly (see Appendix B). The statistical inversion results for $\mathbf{V_{los}}$ using HOLA (and SIR) is shown in Figure 3.4. Similar to the temperature case in Figure 3.1, HOLA and SIR do similarly well in the depth range $\log \tau \in [-2.5, 0.0]$, and are able to recover velocity perturbations with mean differences less than $\approx$ 0.3 km/sec. Outside this region, inversion results from both, HOLA and SIR-only methods, have larger absolute mean difference (and spread) due to lower orthogonal sensitivity.

In Figure 3.5, we show the $\mathbf{V_{los}}$ inversion results for a few handpicked cases. In the top plot, the perturbation is approximately linear which HOLA and SIR methods are able to recover well,

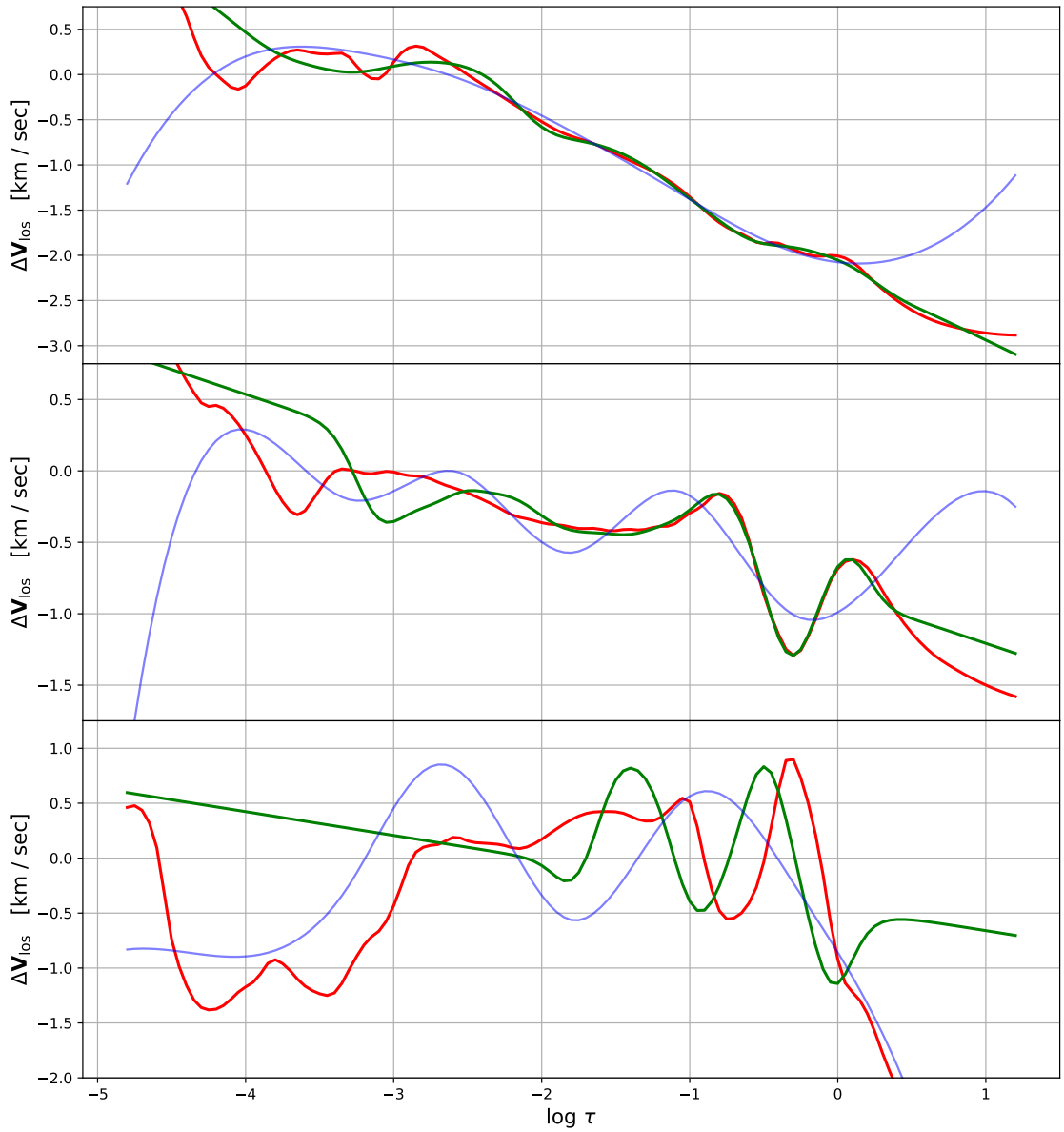

Figure 3.5: $\Delta\mathbf{V_{los}}$ inversion results for three handpicked MURaM cases. In each plot, underlying perturbation is shown in red, HOLA inverted solution is shown in green, and SIR-only inverted solution is shown in blue.

with HOLA being somewhat better at recovering the underlying, slightly higher spatial frequency perturbations. The middle plot is approximately linear with oscillatory shape at around log τ = −0.5. While SIR approximately recovers the large-scale trend, HOLA additionally does a better job at recovering this higher spatial frequency perturbation. The bottom plot corresponds to the case where the HOLA inversion result is dominated by the edge-effect error. Both HOLA and SIR struggle to recover the underlying perturbation.

3.3.3 MURaM $\mathbf{P_e}$ inversion results

In this section we discuss $\mathbf{P_e}$ inversion results obtained using HOLA and SIR methods. The 1st order equation for $\mathbf{\Delta P_e}$ inversion is given by

$$\mathbf{\Delta I} \;=\; \mathbf{R}_{\mathrm{P_e}}^{\top} \cdot \frac{\mathbf{\Delta P_e}}{\mathbf{P_e}} \;+\; \boldsymbol{\varepsilon} \tag{3.2}$$

Unlike, $\mathbf{T}$ and $\mathbf{V_{los}}$ (or $\mathbf{c}_s$), $\mathbf{P_e}$ varies by a few orders of magnitude over photospheric depths (see top plot in Figure 3.6). This variation in $\mathbf{P_e}$ results in the fractional response functions to be significantly different from its dimensional counterpart (see middle and bottom plot in Figure 3.6). Using dimensional response functions when inverting $\mathbf{P_e}$ results in an incorrect inversion solution. This is due to the fact that the averaging kernels are not δ-functions, resulting in the inverted solution at a given depth (in a given inversion cycle) to have cross-talk error contributions from 'nearby' depth locations. When inverting for $\mathbf{P_e}$ using dimensional response functions, these cross-talk errors can be very large, especially in the shallower regions. This is because the underlying perturbation $\mathbf{\Delta P_e}$ (not $\frac{\mathbf{\Delta P_e}}{\mathbf{P_e}}$) magnitude, on average, also increases exponentially as we go deeper and thus the inverted $\mathbf{\Delta P_e}$ are likely to be dominated by the cross-talk errors from the 'nearby' deeper regions. Using fractional response functions mitigates this issue (for the most part) as the underlying fractional perturbation $\frac{\mathbf{\Delta P_e}}{\mathbf{P_e}}$ doesn't show this exponential variation.

It is important to note that fractional response function amplitudes for $\mathbf{P_e}$ are about 30 times smaller than that for $\mathbf{T}$ (Figure 2.2) and about 3 times smaller than that for $\mathbf{V_{los}}$ (Figure 3.3, middle plot). This relatively smaller spectral sensitivity makes it very hard to invert for $\mathbf{P_e}$ when carrying

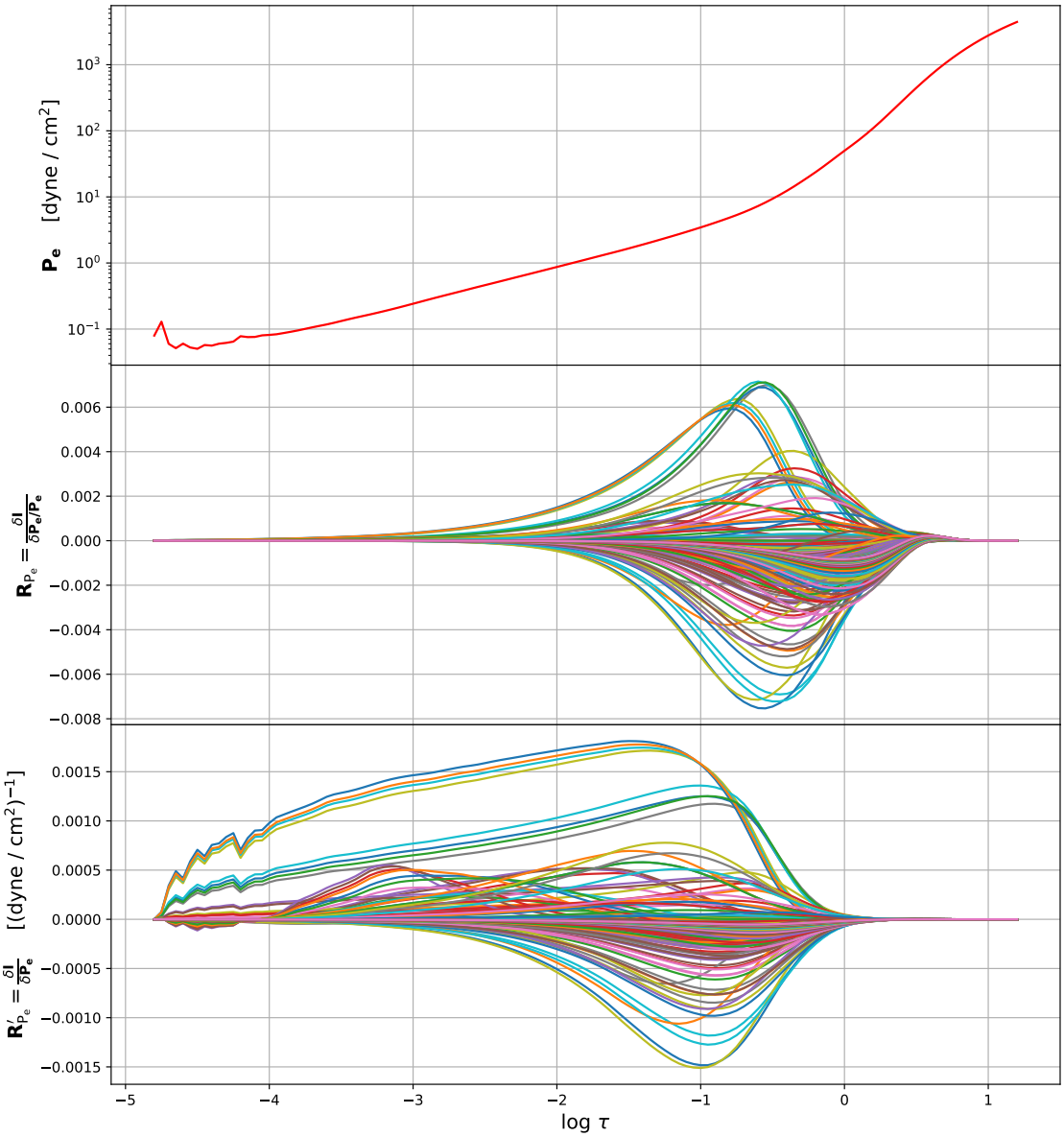

Figure 3.6: (top plot) $\mathbf{P_e}$ vs log τ, (middle plot) fractional $\mathbf{P_e}$ response functions: $\mathbf{R}_{\mathrm{P_e}} = \frac{\delta \mathbf{I}}{\delta \mathbf{P_e}/\mathbf{P_e}}$, (bottom plot) dimensional $\mathbf{P_e}$ response functions: $\mathbf{R}'_{\mathrm{P_e}} = \frac{\delta \mathbf{I}}{\delta \mathbf{P_e}}$. Note that the shape of the fractional and dimensional response functions for $\mathbf{P_e}$ are very different from each other because of drastic variation of $\mathbf{P_e}$ magnitudes over photospheric depths.

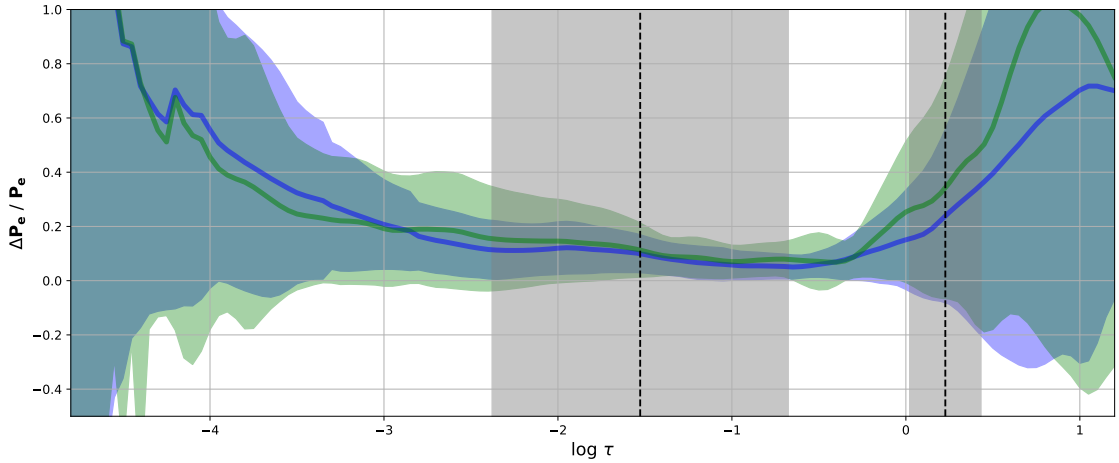

Figure 3.7: Statistical assessment plot for MURaM $\mathbf{P_e}$ inversion done using HOLA (green) and SIR (blue). The green-solid line correspond to the depth dependent mean of the absolute value of the fractional difference between HOLA inverted and underlying MURaM $\mathbf{P_e}$, while the boundary of the shaded region signify the ± 1 standard-deviation around the mean. Similar plot computed for SIR is shown in blue. The black vertical dashed lines mark the mean location of the edge of the OLA inversion window (in final cycle, within HOLA framework) and the gray shaded region mark the ± 1 standard-deviation spread of this edge around the mean location.

out multivariable inversions in the presence of more sensitive $\mathbf{T}$ and $\mathbf{V_{los}}$ (see Chapter 4 for more details).

Single variable HOLA inversion for $\mathbf{P_e}$ is similar to that described for temperature in Section 2.2.6. The appropriate SIR node values are stated in Appendix B. The statistical plot to demonstrate the single variable $\mathbf{P_e}$ inversion capabilities of the HOLA and SIR methods is shown in Figure 3.7. Both methods, on average, are able to recover the underlying perturbation within 20% mean differences in $\log \tau \in [-2.5, -0.25]$ region. Outside of this region, solutions suffer from the limited response function sensitivities.

In Figure 3.8, we show $\mathbf{P_e}$ inversion results for a few handpicked cases. In the top plot, HOLA is able to recover the sharp gradient perturbation shape around $\log \tau = -0.25$. In the middle plot, while HOLA struggles, SIR is able to recover the smoother version of the underlying perturbation. In the bottom plot, both HOLA and SIR struggle to recover the underlying perturbation.

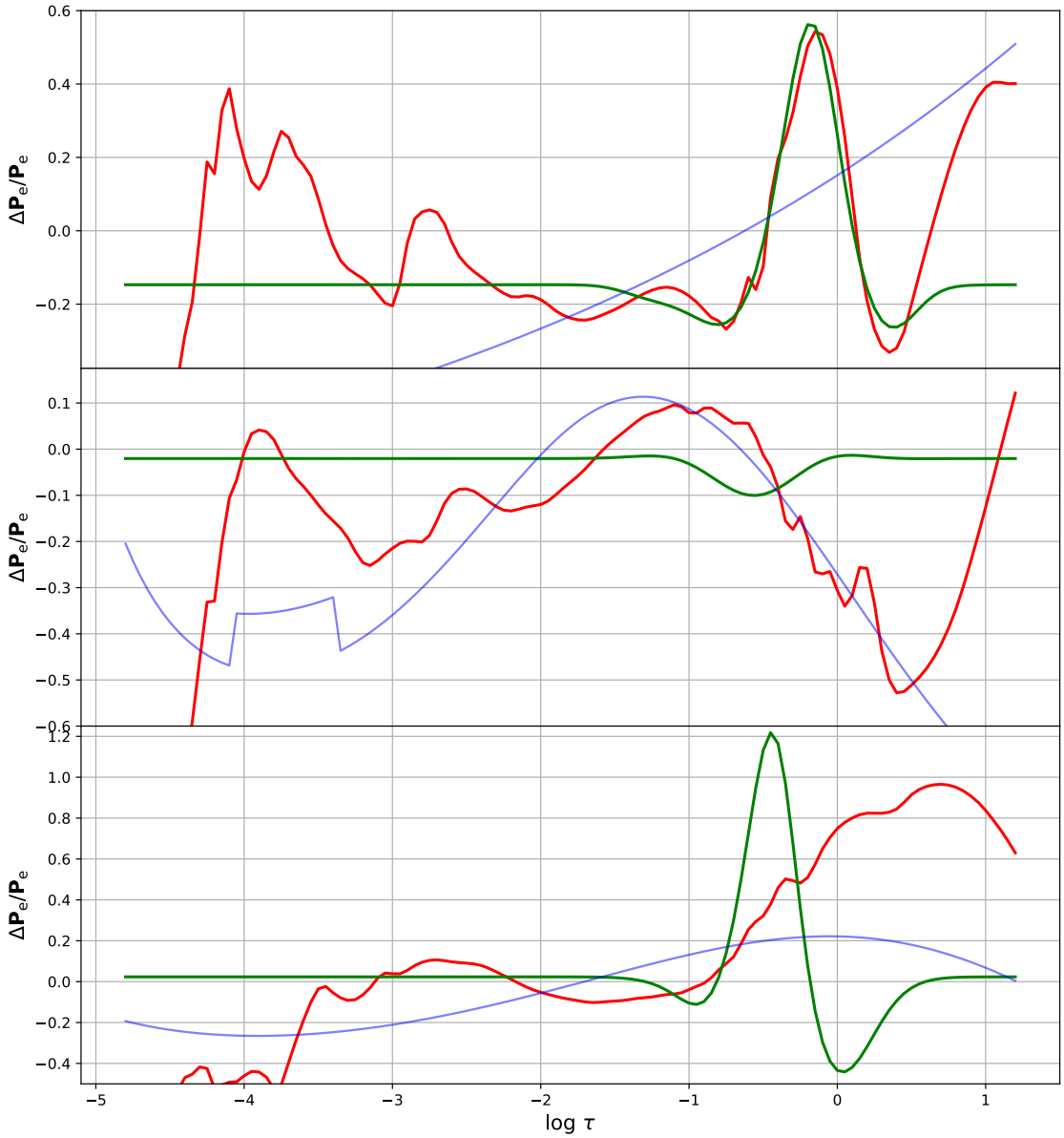

Figure 3.8: Fractional $\frac{\Delta \mathbf{P_e}}{\mathbf{P_e}}$ inversion results for three handpicked MURaM cases. In each plot, underlying fractional perturbation is shown in red, HOLA inverted solution is shown in green, and SIR-only inverted solution is shown in blue.

3.4 Summary

In this chapter, we statistically assessed single variable inversion capabilities of the HOLA method, and compared it with SIR. For this, we inverted a representative sample of MURaM atmospheres. The goal here is to figure out, using the mean MURaM as the starting guess-model, how well individual atmospheres can be recovered using HOLA and SIR. For each of the HOLA and SIR inverted MURaM columns, we computed the difference between the underlying atmosphere and the inverted model (for the given variable). Using this, we computed the depth dependent mean and standard deviation of the absolute value of the differences. These metrics give an insight into how well (on average) HOLA (or SIR) recover the underlying model.

We find that both inversion methods are able to achieve good inversion result over the range $\log \tau \in [-2, 0]$. Even though the overall average inversion quality is very similar for these methods, the underlying cause of error is much different. SIR, by design, is unable to recover sharp gradients due to limited number of nodes, while the current version of HOLA struggles with the edge-effect issue when underlying perturbations have large-scale non-linear shaped offsets. We expect that once the edge-effect issue is mitigated, the inversion capability of HOLA will significantly improve.

Chapter 4

Hybrid-OLA multivariable inversion

In Section 2.2.6, we introduced the HOLA (hybrid-OLA) method using single-variable inversions, for which one assumes that the spectral differences are a consequence of differences between the underlying (actual) and guess-models for a given single variable only i.e. the atmospheric models differ for one variable only. In general, the underlying and guess-models differ for all variables and thus the resulting spectral differences are a combined contribution from all variable differences. In this chapter, we extend the HOLA method to a more general multivariable inversion case. We assume that $\mathbf{T}$, $\mathbf{P_e}$ and $\mathbf{V_{los}}$ completely define the atmosphere. HOLA inversions for magnetic field remain for the future.

4.1 HOLA multivariable inversion: Methodology

4.1.1 1st order equation for a multivariable system

The 1st order equation for a multivariable system can be written as

$$\Delta\mathbf{I} \;=\; \mathbf{R}_{\mathrm{T}}^{\top} \cdot \frac{\Delta\mathbf{T}}{\mathbf{T}} \;+\; \mathbf{R}_{\mathrm{V_{los}}}^{\top} \cdot \frac{\Delta\mathbf{V_{los}}}{\mathbf{c_s}} \;+\; \mathbf{R}_{\mathrm{P_e}}^{\top} \cdot \frac{\Delta\mathbf{P_e}}{\mathbf{P_e}} \;+\; \boldsymbol{\varepsilon} \tag{4.1}$$

Here, the net spectral difference $\Delta\mathbf{I}$ between the underlying and guess-model spectra corresponds to the depth dependent model differences for all variables (i.e. $\frac{\Delta\mathbf{T}}{\mathbf{T}}$, $\frac{\Delta\mathbf{V_{los}}}{\mathbf{c_s}}$ and $\frac{\Delta\mathbf{P_e}}{\mathbf{P_e}}$) weighted by their respective response functions. We use $\boldsymbol{\varepsilon}$ to collectively represent error from the missing higher order terms from all variables and spectral noise in the observational data (if present).

4.1.2 Averaging kernel construction

With a RLS/SIR solver one simultaneously inverts for all variables, at all depth locations, to obtain a globally smooth solution. The basic approach with multivariable OLA inversions is similar to its single-variable counterpart. We invert for a given variable at each depth location individually/independently, with the intention to find inversion solutions that are most localized (minimize error contribution from other depth locations corresponding to the variable we intend to invert for) and simultaneously least contaminated by the contribution from variables other than the one we want to invert for (cross-talk variables). This is accomplished by computing linear coefficients $\mathbf{C}$ such that the linear combination of the response functions for the variable we want to invert for add up to a narrow averaging kernel, while the linear combination of the response functions (using the same linear coefficients $\mathbf{C}$) for the cross-talk variables add up to nearly 0. This is mathematically achieved by solving a linear system of equations such as those shown by the example Equation 4.2.

$$\begin{pmatrix} \mathbf{R}_{\mathrm{T}} \\ \mathbf{R}_{\mathrm{V_{los}}} \\ \mathbf{R}_{\mathrm{P_e}} \end{pmatrix} \cdot \mathbf{C} \quad = \quad \begin{pmatrix} \mathbf{G}\ (\tau_i, \sigma) \\ 0 \\ 0 \end{pmatrix} \tag{4.2}$$

Equation 4.2 aims to construct averaging kernel for temperature at depth τ_i, while minimizing the contributions from cross-talk variables $\mathbf{V_{los}}$ and $\mathbf{P_e}$. To reiterate mathematically, we aim to compute coefficients $\mathbf{C}$ such that $\mathbf{R}_{\mathrm{T}} \cdot \mathbf{C} = \mathbf{A}_{\mathrm{T}}(\tau_i) \approx \mathbf{G}(\tau_i, \sigma)$, while the cross-terms sensitivities at all depths are minimized i.e. $\mathbf{R}_{\mathrm{V_{los}}} \cdot \mathbf{C} = {}^{c}\mathbf{A}_{\mathrm{V_{los}}} \approx 0$ and $\mathbf{R}_{\mathrm{P_e}} \cdot \mathbf{C} = {}^{c}\mathbf{A}_{\mathrm{P_e}} \approx 0$. The super-script '$c$' in ${}^{c}\mathbf{A}_{\mathrm{V_{los}}}$ and ${}^{c}\mathbf{A}_{\mathrm{P_e}}$ mark that these are cross-talk variable kernels and signify the residual sensitivities of the respective cross-talk variables when the kernel construction is not exactly 0. Equation 4.2 is graphically illustrated by Figure 4.1.

Taking the dot product of $\mathbf{C}^{\top}$ with the 1st order Equation 4.1 and recognizing different kernel terms yields:

$$\mathbf{C}^{\top} \cdot \Delta\mathbf{I} \quad = \quad \mathbf{A}_{\mathrm{T}}^{\top}(\tau_i) \cdot \frac{\Delta\mathbf{T}}{\mathbf{T}} \ + \ {}^{c}\mathbf{A}_{\mathrm{V_{los}}}^{\top}(\tau_i) \cdot \frac{\Delta\mathbf{V_{los}}}{\mathbf{c_s}} \ + \ {}^{c}\mathbf{A}_{\mathrm{P_e}}^{\top}(\tau_i) \cdot \frac{\Delta\mathbf{P_e}}{\mathbf{P_e}} \ + \ \mathbf{C}^{\top} \cdot \boldsymbol{\varepsilon} \tag{4.3}$$

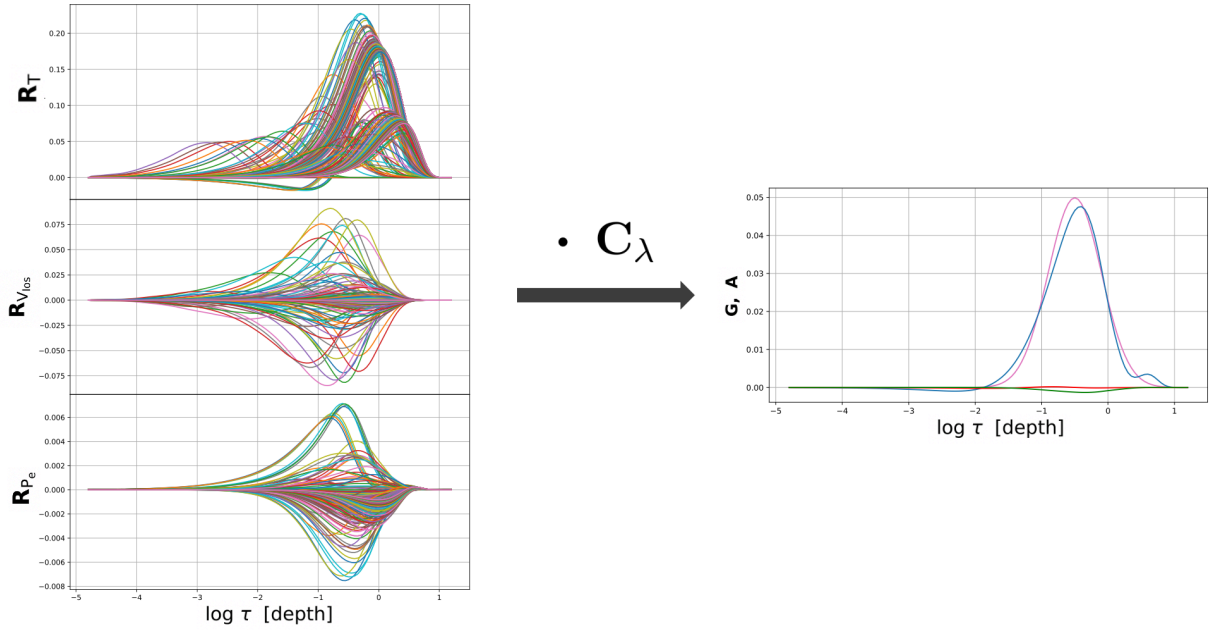

Figure 4.1: Graphical representation of Equation 4.2. Response functions for all variables are shown on the left (top panel = $\mathbf{R}_{\mathrm{T}}$, middle panel = $\mathbf{R}_{\mathrm{V_{los}}}$, and bottom panel = $\mathbf{R}_{\mathrm{P_e}}$), while in the right plot, we show $\mathbf{G}$ (pink), $\mathbf{A}_{\mathrm{T}}$ (blue), ${}^{c}\mathbf{A}_{\mathrm{V_{los}}}$ (red), and ${}^{c}\mathbf{A}_{\mathrm{P_e}}$ (green). We intend to compute $\mathbf{C}$ such that $\mathbf{R}_{\mathrm{T}} \cdot \mathbf{C} = \mathbf{A}_{\mathrm{T}}$ (blue) $\approx \mathbf{G}$, while $\mathbf{R}_{\mathrm{V_{los}}} \cdot \mathbf{C} = {}^{c}\mathbf{A}_{\mathrm{V_{los}}} \rightarrow 0$ and $\mathbf{R}_{\mathrm{P_e}} \cdot \mathbf{C} = {}^{c}\mathbf{A}_{\mathrm{P_e}} \rightarrow 0$.

In Equation 4.3, $\mathbf{C}^{\top}\cdot\,\mathbf{\Delta I}$ is the inversion solution and the right hand side is its interpretation. Ideally, if we could perfectly solve Equation 4.2 such that ${}^{c}\mathbf{A}_{\mathrm{V_{los}}}$ and ${}^{c}\mathbf{A}_{\mathrm{P_e}}$ are exactly 0 at all depths, then the corresponding ${}^{c}\mathbf{A}^{\top}_{\mathrm{V_{los}}}\cdot\,\frac{\mathbf{\Delta V_{los}}}{\mathbf{c_s}}$ and ${}^{c}\mathbf{A}^{\top}_{\mathrm{P_e}}\cdot\,\frac{\mathbf{\Delta P_e}}{\mathbf{P_e}}$ would also be 0. In this case, $\mathbf{C}^{\top}\cdot\,\mathbf{\Delta I}$ would correspond to the desired $\mathbf{A}_{\mathrm{T}}$ averaged inversion solution i.e. $\left\langle \frac{\Delta \mathrm{T}}{\mathrm{T}}(\tau_i) \right\rangle$ (assuming that the error contribution $\mathbf{C}^{\top}\cdot\,\boldsymbol{\varepsilon}$ is negligible). The solution thus obtained would not be contaminated by the error from the cross-talk variable contributions. This also means that the cross-talk variable contribution to $\mathbf{\Delta I}$, in case $\frac{\mathbf{\Delta V_{los}}}{\mathbf{c_s}}$ and/or $\frac{\mathbf{\Delta P_e}}{\mathbf{P_e}} \neq 0$, does not erroneously contribute to the $\left\langle \frac{\Delta \mathrm{T}}{\mathrm{T}}(\tau_i) \right\rangle$ solution (through $\mathbf{C}^{\top}\cdot\mathbf{\Delta I}$), ensuring that the 'source of the spectral difference is preserved'.

In reality, because $\boldsymbol{\varepsilon}$ is not negligible and Equation 4.2 is ill-posed, it can only be approximately solved by inverting a lower-rank version of response function matrices for all variables using the *pseudo-inverse* approach (see section 2.2.1 for details). Since ${}^{c}\mathbf{A}_{\mathrm{V_{los}}}$ and ${}^{c}\mathbf{A}_{\mathrm{P_e}}$ usually cannot be completely suppressed, their contributions in Equation 4.3 act as an additional error source

(unless fortuitously $\frac{\Delta \mathbf{V_{los}}}{\mathbf{C_s}}$ and $\frac{\Delta \mathbf{P_e}}{\mathbf{P_e}}$ are 0). This limits the quality of the inversion that would be otherwise achievable if cross-talk variables were not present. In a multivariable system, there is an additional inherent issue that dictates how 'actively' the 'portions' of the equations corresponding to different variables get solved. As discussed in more detail below, this constrains the minimum averaging kernel width that can be constructed for a given variables and how well the cross-talk variable sensitivities can be suppressed.

4.1.3 Issue with drastically different $\mathbf{R_T}$, $\mathbf{R_{V_{los}}}$ and $\mathbf{R_{P_e}}$ magnitudes

Spectra have varying levels of sensitivity to different atmospheric variables i.e. it is usually more responsive to the temperature perturbations $\frac{\Delta \mathrm{T}}{\mathrm{T}}(\tau_i)$, than electronic pressure $\frac{\Delta \mathrm{P_e}}{\mathrm{P_e}}(\tau_i)$ or line-of-sight velocity $\frac{\Delta \mathrm{V_{los}}}{\mathrm{c_s}}(\tau_i)$ perturbations. This is reflected in the typical magnitudes of the response functions i.e. $\mathbf{R}_{\mathrm{T}}$ peak amplitude is about 30 times larger than $\mathbf{R}_{\mathrm{P_e}}$, and about 3 times larger than $\mathbf{R}_{\mathrm{V_{los}}}$(see Figure 4.1). These differing response function sensitivities mean that, when solving Equation 4.2 (or when directly solving Equation 4.1 in SIR/RLS), the system is biased toward solving temperature related portions of the equations. When solving Equation 4.2, computed coefficients would more 'actively' satisfy $\mathbf{R}_{\mathrm{T}} \cdot \mathbf{C} = \mathbf{G}$, compared to $\mathbf{R}_{\mathrm{P_e}} \cdot \mathbf{C} = 0$ (or $\mathbf{R}_{\mathrm{V_{los}}} \cdot \mathbf{C} = 0$).

The mathematical reasoning for this is explained as follows. When solving Equation 4.2, we first need to compute the *pseudo-inverse* of the 'full' response function matrix (comprised of response functions for all variables) using the singular value decomposition (SVD), which results in $\mathbf{U}$, $\mathbf{S}$ and $\mathbf{V}$ matrices (see section 2.2.1 for details). The resulting individual $\mathbf{u}_i$ eigenvectors (that make up the $\mathbf{U}$ matrix) contain depth dependent orthogonal sensitivity information for all variables. This is illustrated by Figure 4.2. In a given plot row, individual $\mathbf{u}_i$ stretches across different blocks with each block representing the part of the eigenvector that is sensitive to a given variable e.g. the green colored eigenvector (e.g. in the top row) extends across the three blocks with its top-left block portion depicting T sensitivity, while the top-middle and top-right corresponds to $\mathrm{V_{los}}$ and $\mathrm{P_e}$ sensitivities, respectively.

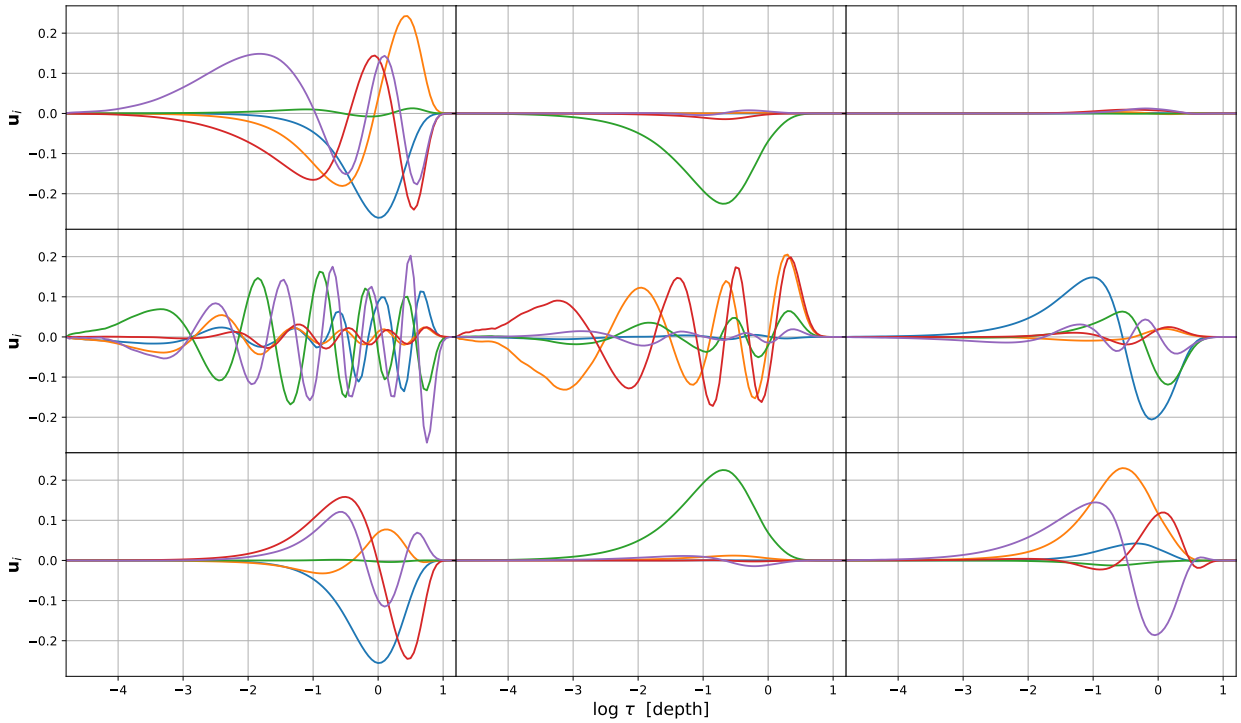

Figure 4.2: Here we show $\mathbf{u}_i$ eigenvectors obtained from the SVD of the 'full' matrix composed of individual variable response functions. Each eigenvector spans across the entire row, while each column corresponds to the part of the vector that is sensitive to a given variable. Left column corresponds to T sensitive portion, middle column corresponds to V_{los} and right column corresponds to P_e sensitive portion.
(Top row) $\mathbf{u}_i$ corresponding to the five largest singular values for the response function matrix used in Equation 4.2.
(Middle row) $\mathbf{u}_i$ corresponding to the 16^{th} through 20^{th} largest singular values for the response function matrix used in Equation 4.2.
(Bottom row) $\mathbf{u}_i$ corresponding to the five largest singular values for the 'amplified' response function matrix used in Equation 4.5.
Note that even with amplification factors, the dominant eigenmodes are not similarly sensitive to all variables and reflect the difference in the distribution of different 'types' of response functions within the matrix, for each variable. For example, the most dominant eigenmode (blue in bottom row) is still mostly sensitive to the temperature response functions, while green is dominantly sensitive to V_{los}.

It is evident that the eigenvectors corresponding to the five largest singular values (shown in the top row) are more sensitive to $\mathbf{R}_{\mathrm{T}}$ than $\mathbf{R}_{\mathrm{P_e}}$ (or $\mathbf{R}_{\mathrm{V_{los}}}$). The sensitivity to $\mathbf{R}_{\mathrm{P_e}}$ and $\mathbf{R}_{\mathrm{V_{los}}}$ is captured by eigenvectors associated with smaller singular values. This is shown in the middle row in Figure 4.2 where we plot the $\mathbf{u}_i$ vectors corresponding to 16^{th} through 20^{th} largest singular values. This fact is a direct consequence of the differing response function magnitude and it becomes a problem when solving Equation 4.2 (or when directly solving Equation 4.1 in SIR/RLS).

As discussed in Section 2.2.1, when solving Equation 4.2, in order to avoid large-amplitude coefficients, which lead to an error dominated inverse solution (i.e. $\mathbf{C}^{\top}\cdot \Delta\mathbf{I} \approx \mathbf{C}^{\top}\cdot \boldsymbol{\varepsilon}$), we compute *pseudo-inverse* matrix of a lower-rank k version of the matrix i.e. the *pseudo-inverse* matrix is computed using only a limited number of eigenmodes corresponding to the largest magnitude singular values. If this limited set of eigenvectors do not carry $\mathbf{R}_{\mathrm{P_e}}$ (or $\mathbf{R}_{\mathrm{V_{los}}}$) sensitivities, then the computed coefficients will be biased to satisfy $\mathbf{R}_{\mathrm{T}} \cdot \mathbf{C} = \mathbf{G}$, as compared to $\mathbf{R}_{\mathrm{P_e}} \cdot \mathbf{C} = 0$. The computed coefficients do not 'actively' reflect the constraints on $\mathbf{P_e}$ in Equation 4.2. This means that ${}^{c}\mathbf{A}_{\mathrm{P_e}}$ is not actively suppressed and the temperature inversions can 'eat-up' $\Delta\mathbf{P_e}$ contribution to the spectral difference $\Delta\mathbf{I}$.

In practice, even though the system doesn't actively solve for $\mathbf{R}_{\mathrm{P_e}} \cdot \mathbf{C} = 0$, the overall amplitude of $\mathbf{R}_{\mathrm{P_e}} \cdot \mathbf{C}$ is approximately 0, as the terms in $\mathbf{R}_{\mathrm{P_e}}$ itself are small, and the temperature inversions are little affected. This is shown in the top-left plot in Figure 4.3 where we plot the narrowest width target function $\mathbf{G}$ (pink) that is reasonably fit by $\mathbf{A}_{\mathrm{T}}$ (blue) when using dominant singular values that add up to 95 % of the total sum (rank $k = 7$). As evident from the plot, the amplitude of the cross-talk kernels ${}^{c}\mathbf{A}_{\mathrm{V_{los}}}$ and ${}^{c}\mathbf{A}_{\mathrm{P_e}}$, shown in red and green, are small, so the $\Delta\mathbf{T}$ inversion is little affected. However, biased sensitivity of the *pseudo-inverse* matrix becomes a critical issue when we intend to construct $\mathbf{A}_{\mathrm{P_e}}$ (and invert for $\frac{\Delta\mathbf{P_e}}{\mathbf{P_e}}$) and suppress the contribution

of $\frac{\Delta \mathbf{T}}{\mathbf{T}}$. This requires the solution of:

$$\begin{pmatrix} \mathbf{R}_{\mathrm{T}} \\ \mathbf{R}_{\mathrm{V_{los}}} \\ \mathbf{R}_{\mathrm{P_e}} \end{pmatrix} \cdot \mathbf{C} \quad = \quad \begin{pmatrix} 0 \\ 0 \\ \mathbf{G}(\tau_i, \sigma) \end{pmatrix} \tag{4.4}$$

The negligible $\mathbf{R}_{\mathrm{P_e}}$ sensitivity in the *pseudo-inverse* matrix prevents us from fitting even the widest allowed target function width, as the coefficients dominantly solve for $\mathbf{R}_{\mathrm{T}} \cdot \mathbf{C} = 0$. This is shown in the top-right in Figure 4.3, where the $\mathbf{A}_{\mathrm{P_e}}$ (green) does not match the widest target function $\mathbf{G}$ (pink), while cross-talk sensitivities ${}^{c}\mathbf{A}_{\mathrm{T}}$ and ${}^{c}\mathbf{A}_{\mathrm{V_{los}}}$ are minimized. In order to successfully construct $\mathbf{A}_{\mathrm{P_e}}$ we would have to use a larger rank so that the corresponding eigenmodes carry $\mathbf{R}_{\mathrm{P_e}}$ sensitivities. This is shown in the middle-right curve in Figure 4.3 where we used rank $k = 22$, based on dominant singular values that they add up to 99.9 % of the total sum. As mentioned before, larger rank k solutions are typically error dominated. Thus, the widely differing $\mathbf{R}_{\mathrm{T}}$ and $\mathbf{R}_{\mathrm{P_e}}$ magnitudes imply that it is hard to invert for $\frac{\Delta \mathbf{P_e}}{\mathbf{P_e}}$ in the presence of $\frac{\Delta \mathbf{T}}{\mathbf{T}}$ (or $\frac{\Delta \mathbf{V_{los}}}{\mathbf{c_s}}$).

4.1.4 Workaround to differential response function amplitudes

There is a solution to this problem. Building on Equation 4.4, we solve the following modified system of equations:

$$\begin{pmatrix} \alpha_1 \cdot \mathbf{R}_{\mathrm{T}} \\ \alpha_2 \cdot \mathbf{R}_{\mathrm{V_{los}}} \\ \mathbf{R}_{\mathrm{P_e}} \end{pmatrix} \cdot \mathbf{C} \quad = \quad \begin{pmatrix} 0 \\ 0 \\ \mathbf{G}(\tau_i, \sigma) \end{pmatrix} \tag{4.5}$$

Here, α_1 and α_2 are the response function amplification factors which we use to manually amplify/de-amplify the cross-talk variable response functions to make their amplitudes 'similar' to those of the variable we are trying to construct averaging kernel for. This mathematical operation is similar to multiplying both sides of an equation by a constant factor, and does not change the original Equation 4.4. But, they do change the 'required' *pseudo-inverse*, helping to retain information about lower sensitivity variables in the system. The amplification factor modified matrix raises the

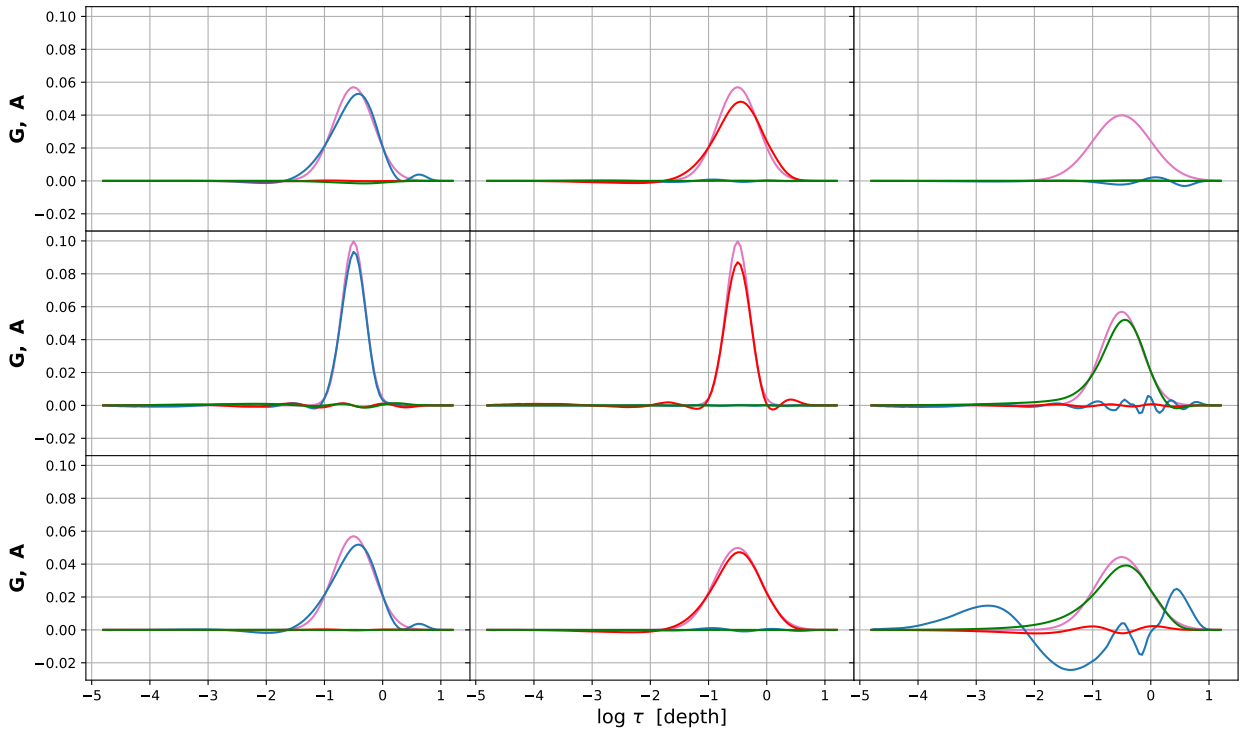

Figure 4.3: Here we show how well averaging kernel for a given variable can be constructed, while simultaneously minimizing cross-talk kernel sensitivities. In all plots, pink curve corresponds to the narrowest width target-function (pink) that we can fit at $\log \tau = -0.5$ for different variables, while kernels (averaging or cross-talk) for T is shown in blue, for $\mathrm{V_{los}}$ is shown in red, and for $\mathrm{P_e}$ is shown in green. Plots in the left column is where we construct $\mathbf{A}_\mathrm{T}$, while middle and right column correspond to $\mathbf{A}_{\mathrm{V_{los}}}$ and $\mathbf{A}_{\mathrm{P_e}}$ kernel construction.
(Top-row) Averaging kernel construction and cross-talk kernel minimization done by solving Equation 4.2 (appropriate version for different variables) using rank $k = 7$ (based on largest singular values that add up to 95 % of the total sum). While, it is possible to construct kernels for $\mathbf{A}_\mathrm{T}$ and $\mathbf{A}_{\mathrm{V_{los}}}$, $\mathbf{A}_{\mathrm{P_e}}$ do not fit even the widest allowed target function (top-right plot).
(Middle-row) Averaging kernels constructed by solving the equations as above, but with rank $k = 22$ (based on largest singular values that add up to 99.9 % of the total sum). Using a larger number of eigenmodes result in averaging kernels that fit a narrower width $\mathbf{G}$ while cross-talk kernels are better minimized. Further, this also allows construction of $\mathbf{A}_{\mathrm{P_e}}$. The caveat of using larger rank k is that it leads to error dominated inversion solutions.
(Bottom-row) Averaging kernels constructed by solving Equation 4.5 (appropriate version for different variables) using rank $k = 10$ (based on largest singular values that add up to 95 % of the total sum). Using this approach, we can maintain $\mathbf{R}_{\mathrm{P_e}}$ sensitivity in the *pseudo-inverse* matrix even with a smaller rank, which allows us to construct $\mathbf{A}_{\mathrm{P_e}}$ in the presence of more spectrally sensitive variables. Given that amplification factors have to be eventually factored out, the corresponding ${}^c\mathbf{A}_\mathrm{T}$ is not minimized well.

sensitivity to the lower magnitude response functions, yielding the eigenvectors of the dominant singular values with 'similar' sensitivity across all variables. This is illustrated in the bottom row in Figure 4.2, where we show the $\mathbf{u}_i$ eigenvectors corresponding to the five largest singular values obtained from the SVD of the matrix in Equation 4.5 after amplification. These eigenvectors are more sensitive to $\mathbf{R}_{\mathrm{P_e}}$ compared to the those in the top row, where no amplification factors were used.

The question now is what amplification factors to use. If the factors are large, then the *pseudo-inverse* matrix are more sensitive to the cross-talk variables and if the factors are small then the cross-talk variable sensitivity might not get actively suppressed. To determine 'optimal' amplification factors we tried the ratio of the total sum of the absolute response function matrix for the variable we intend to invert and cross-talk variables, ratio of the dominant singular value of the respective response function matrices. We settled on factors obtained by taking the ratio of the maximum of the absolute value response functions i.e. in Equation 4.5, $\alpha_1 = \frac{max(|\mathbf{R}_{\mathrm{P_e}}|)}{max(|\mathbf{R}_{\mathrm{T}}|)}$ and $\alpha_2 = \frac{max(|\mathbf{R}_{\mathrm{P_e}}|)}{max(|\mathbf{R}_{\mathrm{V_{los}}}|)}$. For our response function matrices (obtained for the mean MURaM guess-model) these ratios come out to be $\alpha_1 \approx 0.03$ and $\alpha_2 \approx 0.08$. Note that these factors are less than 1 because the amplitudes of $\mathbf{R}_{\mathrm{T}}$ and $\mathbf{R}_{\mathrm{V_{los}}}$ is larger than $\mathbf{R}_{\mathrm{P_e}}$. It is always the cross-talk variable response functions to which the amplification factors get applied to e.g. if we are constructing averaging kernels for temperature, then the corresponding amplification factors will be applied to $\mathbf{R}_{\mathrm{V_{los}}}$ and $\mathbf{R}_{\mathrm{P_e}}$. This removes the additional step of factoring out the amplification factors from the coefficients before computing the inverse solution $\mathbf{C}^{\top}\bullet\,\Delta\mathbf{I}$.

Given that the dominant $\mathbf{u}_i$ eigenvectors are now sensitive to $\mathbf{R}_{\mathrm{P_e}}$, we can 'actively' solve for the $\mathrm{P_e}$-related equations in Equation 4.5 and construct $\mathbf{A}_{\mathrm{P_e}}$ in the presence of T and $\mathrm{V_{los}}$ without being required to use too many eigenmodes. This is shown in the bottom-right plot in Figure 4.3 where we show the narrowest width $\mathbf{A}_{\mathrm{P_e}}$ (green) that reasonably matches the target function (pink), when computing *pseudo-inverse* using singular values that add up to 95 % of the total sum (rank $k = 10$).

We note that when constructing $\mathbf{A}_{\mathrm{P_e}}$, the cross-talk ${}^{c}\mathbf{A}_{\mathrm{T}}$ sensitivity is not entirely suppressed.

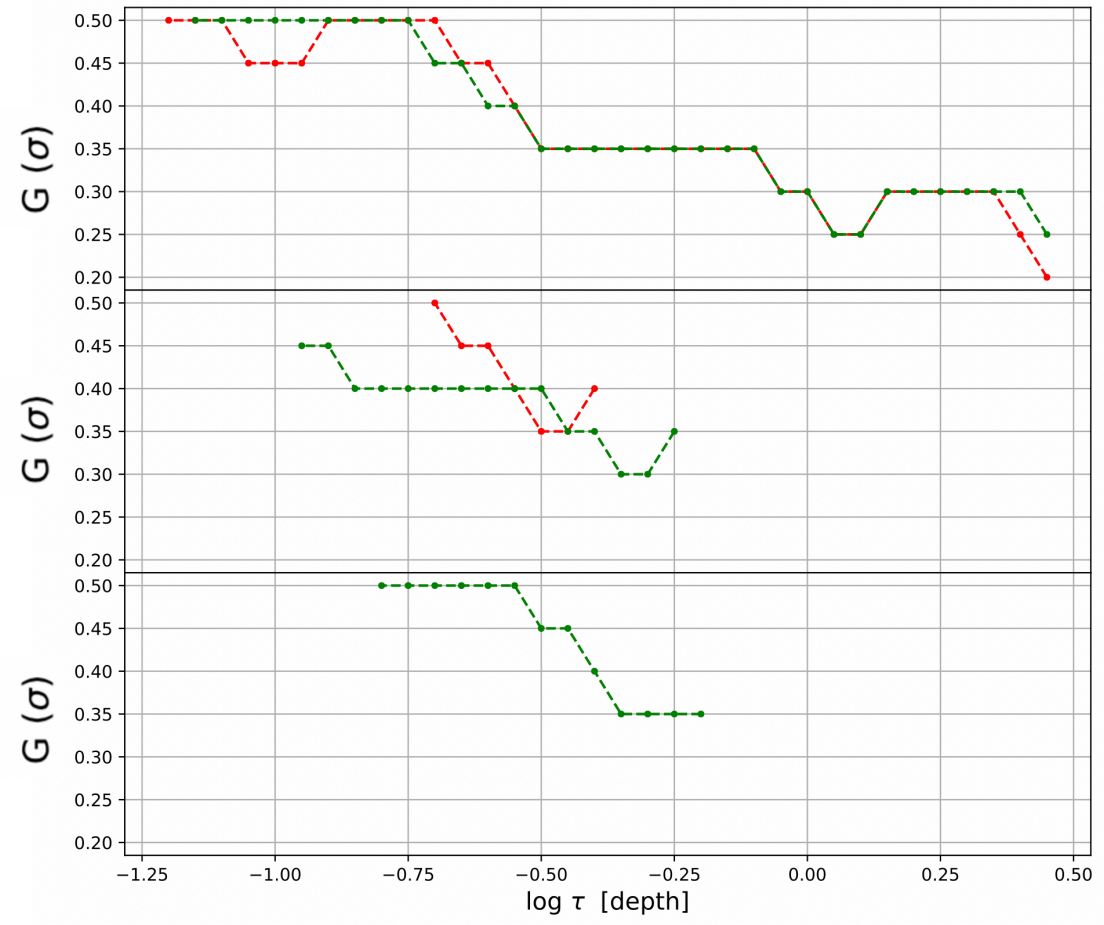

Figure 4.4: Minimum target function width vs. depth curve, with (green) and without (red) response function amplification factors. Top panel corresponds to when constructing temperature kernels, while middle and lower panels correspond to when constructing V_{los} and P_e kernels, respectively. Out of the three, temperature has the widest depth range over which inversion can be done (given the rank). In all cases, *pseudo-inverse* matrix is computed using rank k such that dominant singular values add up to 95% of the total sum. This corresponds to $k = 10$ (with) and $k = 7$ (without) amplification factors.

This is because using amplification factors gets around the inherent sensitivity bias but does not remove it. Due to the inherent sensitivity bias and the finite information in the limited number of eigenmodes used, one usually cannot construct narrow averaging kernels for P_e while simultaneously minimizing cross-talk kernel sensitivity to other variables. Mathematically, this can be understood as follows. Using amplification factors and solving Equation 4.5 results in the computed coefficients

to actively minimize cross-talk $\alpha_1 \times (\mathbf{R}_\mathrm{T} \cdot \mathbf{C}) = 0$. But the 'true/actual' cross-talk kernel is given by ${}^c\mathbf{A}_\mathrm{T} = \mathbf{R}_\mathrm{T} \cdot \mathbf{C}$. The artificial amplification factors need to be ultimately factored out when computing ${}^c\mathbf{A}_\mathrm{T}$. When constructing $\mathbf{A}_{\mathrm{P_e}}$, α_1 is usually small ($\ll 1$), so once α_1 is factored out, the 'actual' cross-talk kernel ${}^c\mathbf{A}_\mathrm{T}$ may have large amplitudes and may not be completely suppressed. The large cross-talk sensitivities poses a risk when inverting $\frac{\Delta \mathbf{P_e}}{\mathbf{P_e}}$ as the inversion solution would most likely be corrupted by the cross-talk errors, unless underlying perturbations $\frac{\Delta \mathbf{T}}{\mathbf{T}}$ (and $\frac{\Delta \mathbf{V_{los}}}{\mathbf{c_s}}$) are small. Given that we invert for one variable at a time when doing OLA inversions, this determines the order in which different variables get inverted. This is discussed in detail in Section 4.2.

In Figure 4.4, we demonstrate how using amplification factors helps when constructing kernels for lesser sensitive variables. Here, we show the narrowest kernel width, as a function of depth, that can be constructed with (green) and without (red) amplification factors (in the presence of corresponding cross-talk terms). The results are obtained using *pseudo-inverse* matrix computed using dominant singular values that add up to 95 % of the total sum. For the non-amplified response function matrix used in Equation 4.2 (or 4.4), rank $k = 7$, while for the amplified/de-amplified matrix of Equation 4.5, $k = 10$. The increase in rank for the same cumulative singular value percentage (when using amplified matrix) means that the using amplification factor improves the overall ill-posedness of the system.

The top plot corresponds to averaging kernel widths for temperature inversions and has the largest depth range (out of all variables) over which inversion can be done. Using the amplification factors (green curve) when doing temperature inversions can lead to wider kernels as compared to when no amplification factor is used (red curve). This is because, without amplification factors, it is the temperature related equations $\mathbf{R}_\mathrm{T} \cdot \mathbf{C} = \mathbf{G}(\tau, \sigma)$ that dominate because of the inherent spectral sensitivity towards temperature perturbations. When using amplification factors, the system has to now simultaneously minimize cross-talk sensitivities, making it harder to fit narrower width target functions for temperature. This can also be understood as follows. Using amplification factors lead to the dominant $\mathbf{u}_i$ vectors that are similarly sensitive to all variables. Given the constraint

that these eigenvectors are orthonormal, the overall amplitude of the temperature components of $\mathbf{u}_i$ is relatively smaller, as the eigenvectors now also preserve $\mathbf{R}_{\mathrm{P_e}}$ sensitivities, making it relatively harder to construct narrower width target functions.

The middle and bottom plot in Figure 4.4 corresponds to the narrowest width averaging kernel when constructing $\mathbf{A}_{\mathrm{V_{los}}}$ and $\mathbf{A}_{\mathrm{P_e}}$, respectively. It is evident from these plots that using amplification factors helps when construct averaging kernels for lesser sensitive variables. Given the rank and fitting constraints, $\mathbf{A}_{\mathrm{P_e}}$ construction (and $\frac{\mathbf{\Delta P_e}}{\mathbf{P_e}}$ inversions) is only possible when using amplification factors.

4.2 Multivariable HOLA inversion method: Implementation

In this section we discuss how the HOLA method is implemented to carry out multivariable inversions. The approach is similar to its single variable counterpart (see Section 2.2.6) where inversion is done over multiple inversion cycles, with each cycle made up of two sub-pieces: SIR to make large-scale updates and OLA to make high-resolution small-scale updates for a given variable. The difference here is that the single variable OLA averaging kernel construction Equation 2.9 is replaced with its 'appropriate' multivariable counterpart (as described in Section 4.1.4) e.g. when inverting for $\frac{\mathbf{\Delta P_e}}{\mathbf{P_e}}$ in the presence of $\frac{\mathbf{\Delta T}}{\mathbf{T}}$ and $\frac{\mathbf{\Delta V_{los}}}{\mathbf{c_s}}$, Equation 4.5 is used. The goal here is to invert a given variable while simultaneously preserving the spectral contributions of the cross-talk variable perturbations. Preserving spectral contribution is critical as it minimizes cross-talk errors and allows us to invert for all variables. Given OLA (within HOLA framework) inverts for only one variable at a time, we need to iterate over each variable in order to do multivariable inversion. Given that there is an inherent sensitivity bias issue that dictates how well kernels can be constructed for a given variable and how well cross-talk sensitivities can be simultaneously minimized, it is critical to follow a specific order in which different variables get inverted. We start with inverting the largest spectrally sensitive variable ($\frac{\mathbf{\Delta T}}{\mathbf{T}}$ in our case) as it is relatively easier to construct averaging kernels for it and simultaneously suppress cross-talk sensitivities. Once the HOLA inversion for $\frac{\mathbf{\Delta T}}{\mathbf{T}}$ is complete, we update guess-model $\mathbf{T}$ with the inverted $\mathbf{T}$, and repeat the inversion process

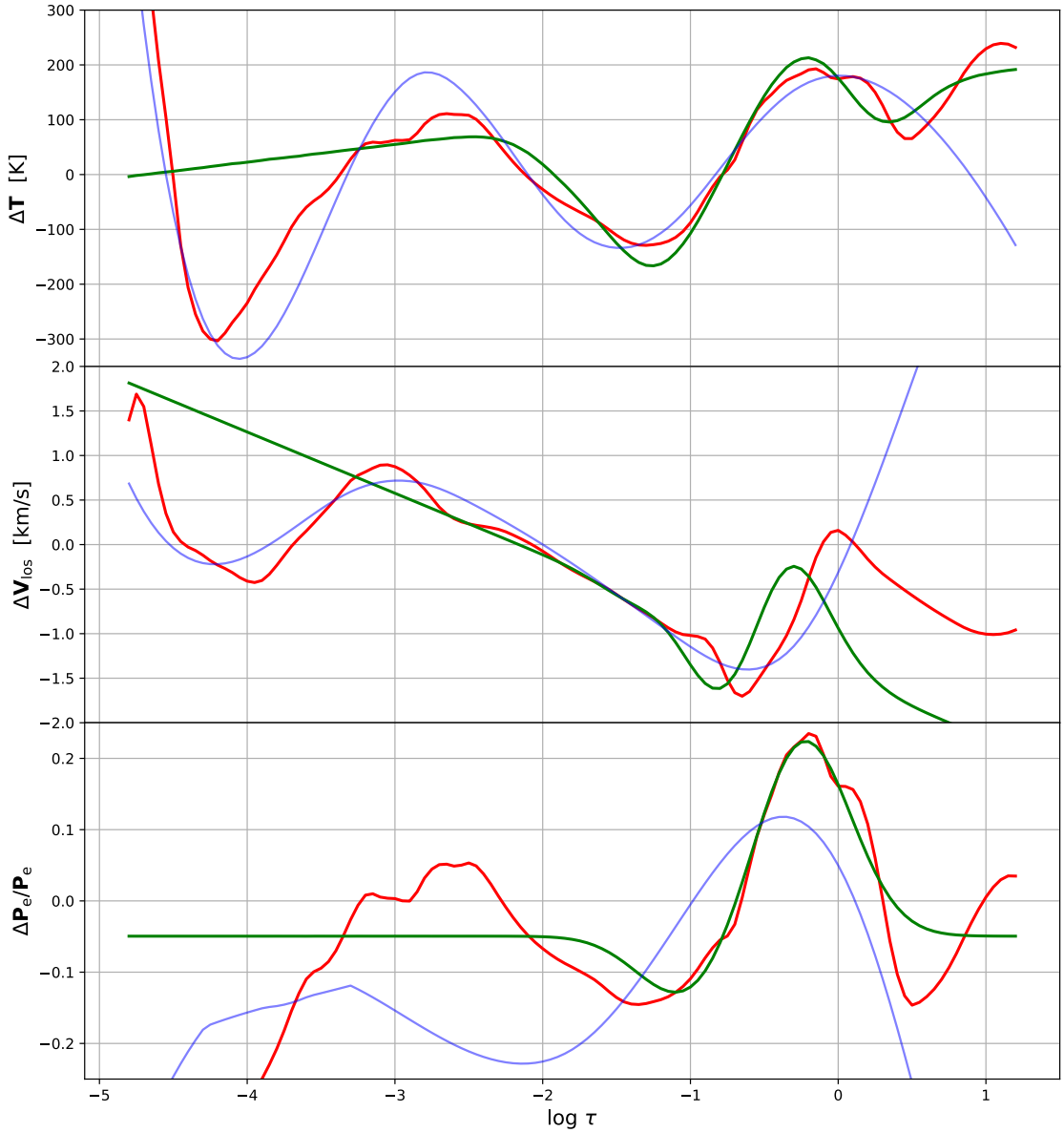

Figure 4.5: Multivariable inversion results obtained by inverting an arbitrary MURaM atmospheric column. In each plot, underlying perturbation is shown in red, HOLA inverted solution is shown in green, while SIR-only inverted solution is shown in blue. Top panel corresponds to temperature perturbations, middle panel corresponds to line-of-sight velocity perturbations and bottom panel corresponds to fractional electronic pressure perturbations.

for the next most dominantly sensitive variable ($\frac{\Delta \mathbf{V_{los}}}{\mathbf{c_s}}$ in our case) and ultimately, invert for $\frac{\Delta \mathbf{P_e}}{\mathbf{P_e}}$.

Using the dominant variable (e.g. $\mathbf{T}$, $\mathbf{V_{los}}$) inversion solution updated guess-model helps

improve our odds when inverting for $\frac{\Delta \mathbf{P_e}}{\mathbf{P_e}}$. This is because, even though the cross-talk kernel sensitivities (${}^{c}\mathbf{A}_{\mathrm{T}}$ and ${}^{c}\mathbf{A}_{\mathrm{V_{los}}}$) cannot not completely minimized, the cross-talk perturbation amplitudes are now smaller (assuming $\frac{\Delta \mathbf{T}}{\mathbf{T}}$ and $\frac{\Delta \mathbf{V_{los}}}{\mathbf{c_s}}$ updates are in the right direction), resulting in the overall cross-talk error contributions to $\frac{\Delta \mathbf{P_e}}{\mathbf{P_e}}$ to be smaller. In practice, cross-talk variables cannot be completely minimized and act as an additional error term.

Note that in a given HOLA inversion cycle, irrespective of the variable being inverted for (using OLA), we make SIR large-scale updates for all variables (see Appendix B for node values). Making large-scale updates for all variables helps improve the HOLA inversion quality as it lowers the magnitude of the higher order error terms (assuming updates are in the 'right' direction), especially from the cross-talk variables if their perturbation amplitudes are large. A reduced overall magnitude for higher order error (from all variables) implies that we can employ a larger rank k (beyond which solution gets error dominated), improving the OLA inversion resolution and thus the overall HOLA inversion quality.

In Figure 4.5 we show the multivariable inversion solution for an arbitrary MURaM atmospheric column. The top plot corresponds to $\mathbf{\Delta T}$ inversion, middle to $\mathbf{\Delta V_{los}}$ inversions and bottom plot corresponds to $\frac{\Delta \mathbf{P_e}}{\mathbf{P_e}}$ inversion. In each plot, the red curve corresponds to difference between the underlying and the guess-model, green curve corresponds to the HOLA inverted solution and the blue curve corresponds to the SIR-only inverted solution. The HOLA method is able to recover the overall shape of the underlying perturbations (even for $\frac{\Delta \mathbf{P_e}}{\mathbf{P_e}}$). The method by design cannot recover non-linear perturbation shapes in the deeper and shallower regions and struggles due to the edge-effect issue.

4.3 Summary

In this chapter, we extended the HOLA method to invert for more realistic multivariable system. We assumed that the multivariable system is completely defined by the thermodynamic parameters $\mathbf{T}$, $\mathbf{V_{los}}$ and $\mathbf{P_e}$. We discussed the modifications need to be made to the single variable kernel construction equation to do multivariable HOLA inversion of these variables. The 1st order

equation for a multivariable system given by Equation 4.1 states that the spectral differences $\mathbf{\Delta I}$ between the underlying and guess-model spectra corresponds to the model differences from all variables weighted by their respective response functions (with error contributions from the omitted higher order terms for each variable and spectral noise, if present). In multivariable OLA method (within HOLA framework), one inverts for one variable at one depth location at a time with the goal of obtaining solutions with minimized cross-talk error contributions from other depth locations (from the same variable perturbations) and from cross-talk variable perturbations. This is achieved by computing linear coefficients $\mathbf{C}$ that constructs narrow width averaging kernels at a given depth location (for the variable we intend to invert) and simultaneously minimizes cross-talk variable sensitivities.

There is an inherent issue faced when inverting variables in a multivariable system. This issue has to do with the fact that spectra is more sensitive to temperature perturbations, compared to electronic pressure (or line-of-sight velocity) perturbations. This bias results in the *pseudo-inverse* computed using dominant eigenmodes of the matrix (e.g. in Equation 4.2) to be mostly sensitive to $\mathbf{R}_{\mathrm{T}}$, as compare to $\mathbf{R}_{\mathrm{P_e}}$, and is likely to solve for temperature portions of the equation, compared to electronic pressure. This makes it harder to invert for $\frac{\mathbf{\Delta P_e}}{\mathbf{P_e}}$ in the presence of $\frac{\mathbf{\Delta T}}{\mathbf{T}}$.

We developed a workaround to this issue in Section 4.1.4 where we suggested that artificially amplifying/de-amplifying cross-talk variable response function matrices with the help of amplification factors may help remove this sensitivity bias. This would result in the dominant eigenmodes of the 'modified full' matrix to have sensitivity across all variables. We demonstrated that using amplification factors allows us to construct averaging kernels for $\mathbf{A}_{\mathrm{P_e}}$ (with smaller number of eigenmodes) and gives us a better chance at inverting electronic pressure in a multivariable system. It is important to note that using amplification factors gets around the inherent sensitivity bias but doesn't not eliminate it. This means that we cannot successfully construct kernels for electronic pressure and simultaneously minimize cross-talk kernel sensitivities for temperature. This forces us to employ a certain order in which different variables get inverted when using the OLA method (within HOLA framework).

We applied the developed multivariable HOLA inversion method to a MURaM column and the results are promising. The solution quality is limited by the edge-effect issue inherent to the OLA method. We expect that the overall inversion capability will significantly improve once this issue is mitigated. We expect that the idea of using amplification factors to maintain the lesser spectrally sensitive variables should also benefit other inversion methods (e.g. SIR/RLS) as well.

Chapter 5

Information within response function matrix and assessing its ability to do inversions

As mentioned in Section 2.1.2, inverse problems require us to solve the 1st order linear system of Equations 2.5 where the first step is to compute the inverse of the response function matrix. This is a non-trivial task as the system belongs to the ill-posed category. Further, the equations are not perfect (error ε is non-zero) which compels us to employ a lower-rank *pseudo-inverse* of the matrix to solve the system and obtain solutions that are not dominated by error. The caveat of using a lower rank *pseudo-inverse* is that the information belonging to smaller singular values get discarded. Depending on how sensitivity information is distributed in the matrix, these discarded singular values may contain critical information needed to invert at certain depths/variables. Removing these singular values degrades our ability to invert at these depths/variables. One such case is discussed in Section 4.1.3, in which, due to the inherent spectral sensitivity bias, dominant eigenmodes are more sensitive to temperature than electronic pressure. This makes it harder to invert for electronic pressure perturbations in the presence of temperature perturbations.

In this chapter we focus on another situation with similar sensitivity bias issue. The presence of a large number of 'almost identical/redundant' response functions (with non-zero amplitude) in the matrix, results in dominant eigenmodes with greater sensitivity in those regions where the redundant response functions peak, degrading the inversion capability in other regions. This issue can be mitigated by artificially removing some redundant response functions from the matrix.

We also demonstrated that once the redundancies are removed, the slope of the singular value

curve (log s_i vs. i^{th} mode) can be used as a metric to quantitatively compare different spectral line combinations and determine which combinations are likely to produce best inversion results. The goal is to find x 'best' spectral lines, out of n total lines, that would be most suitable for a particular scientific inquiry. We make an estimation of what this inversion potential looks like based on the averaging kernel width.

For simplicity, we limit the discussion here to single variable temperature inversions of artificially constructed Gaussian-shaped perturbations (similar to that discussed in Section 2.2), using mean MURaM as the starting guess-model. We invert these perturbations using iterative-OLA method i.e. HOLA inversion method without the large-scale SIR updated, as SIR large-scale updates can artificially introduce large-scale offsets which could lead to solutions dominated by the edge-effect. Additionally, all inversions are done in the absence of observational noise.

5.1 Redundant sensitivity in $\mathbf{R_T}$ matrix

A typical response function matrix (fractional or dimensional), computed for a given model and spectral line-set, usually contains disproportionately large number of response functions that are 'almost identical' to one another. These response functions typically correspond to continuum intensity wavelengths that makeup a large fraction of any spectrum, as a typical observed spectral range (bandwidth) is usually much larger than the width of the line itself. A broad spectral range is needed to accommodate spectral line shifts (non-zero $\mathbf{V_{los}}$). In Figure 5.1 (top panel), we plot the fractional response function computed for temperature (for mean MURaM model) that makeup the $\mathbf{R}_{\mathrm{T}}$ matrix, computed for all spectral lines mentioned in Table A.1. There is a cluster of similarly sensitive (redundant) response functions at $\log \tau \approx 0.0$ (for visible continuum wavelengths) and $\log \tau \approx 0.25$ (for infrared continuum wavelengths).

These redundant response functions are most sensitive to deeper regions of the atmosphere, and since they makeup a large fraction of $\mathbf{R}_{\mathrm{T}}$, they introduce a bias in the information captured by the matrix. This results in the dominant eigenmodes ($\mathbf{u}_i$ of $\mathbf{R}_{\mathrm{T}}$) that are most sensitive to deeper regions, and the lower rank *pseudo-inverse* is more capable of inverting in deeper regions, than

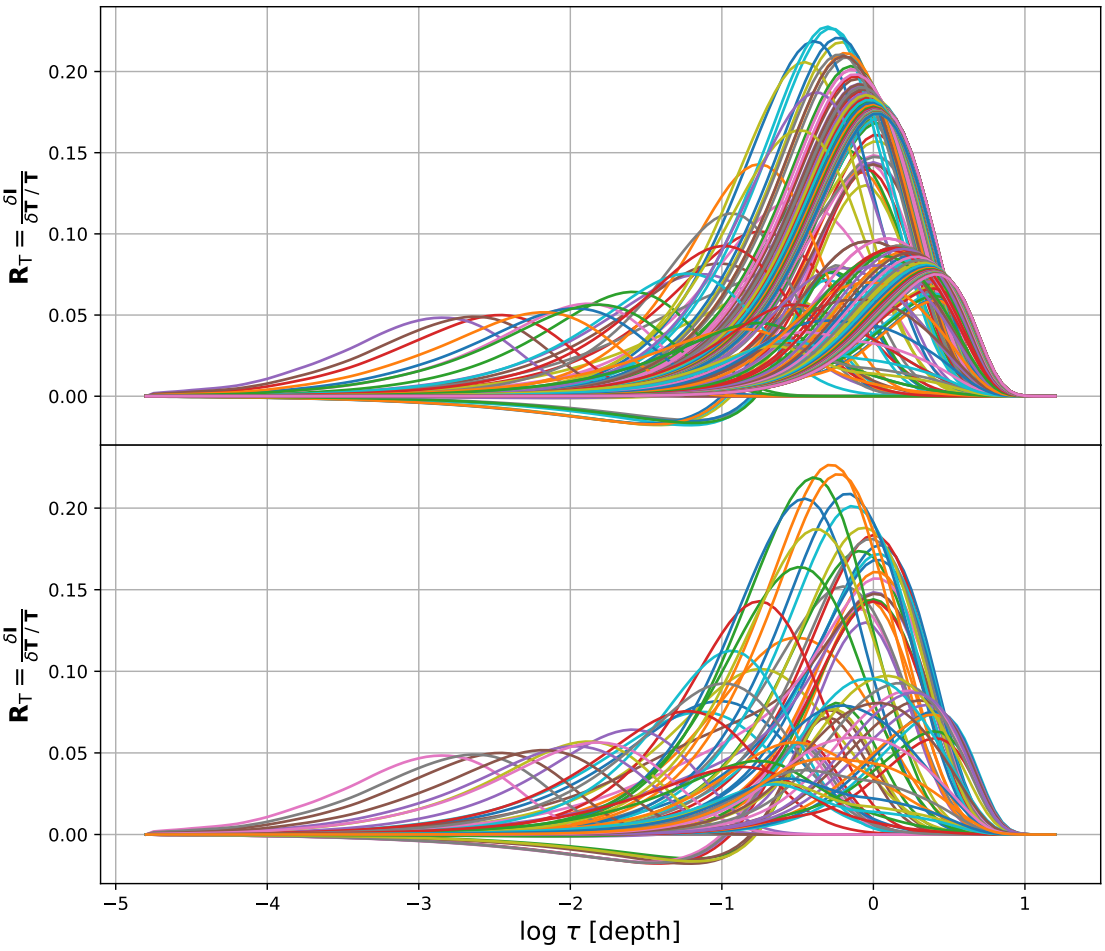

Figure 5.1: (top-plot) Fractional response functions for temperature computed using SIR for the mean MURaM model, for all spectral lines mentioned in Table A.1. (bottom-plot) Response functions left in $\mathbf{R}_\mathrm{T}$, after removing redundant response functions using $p_3 = 5\%$.

shallower regions. Though there are response functions that are sensitive to shallower regions they are small in number. A potential workaround is to artificially remove some redundant response functions. The dominant eigenmodes are then more 'similarly' sensitive to different regions of the atmosphere. By removing some redundant response functions we remove the sensitivity bias in the matrix. This then allows us to invert in the shallower regions using lower rank *pseudo-inverse*, improving the overall inversion capability. This is demonstrated in Figure 5.2 where we show the minimum averaging kernel width vs. depth that can be constructed using $\mathbf{R}_\mathrm{T}$ with (red) and without (blue) redundancies. The response functions are identified redundant (and removed)

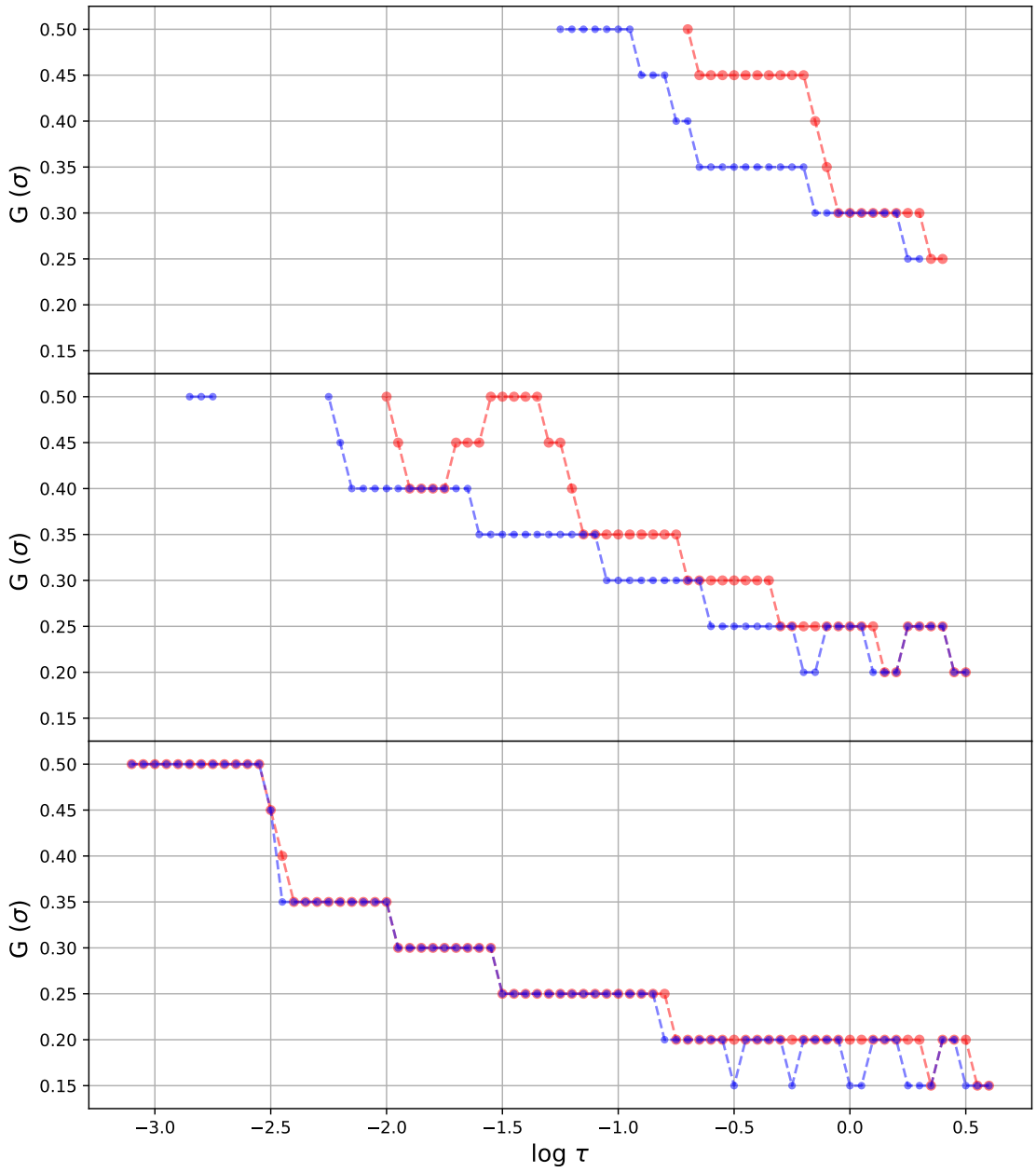

Figure 5.2: Minimum width target function vs. depth, that can be constructed, with (red) and without (blue, $p_3 = 5\%$) redundancy in $\mathbf{R}_{\mathrm{T}}$. The top plot corresponds to rank k such that the sum of the largest singular values add up to 95% of the total. The middle and bottom plot corresponds to cases when the cumulative sum is 99% and 99.9%, respectively.

based on an algorithm described in Appendix 5.5. The three panels shown correspond to kernels constructed using different rank *pseudo-inverse* matrices. The top plot corresponds to a rank such that the sum of the largest singular values add up to 95% of the total, while middle and bottom plot corresponds to cases when the sum is 99% and 99.9% respectively.

It is evident from these plots that removing the redundant response functions considerably improves the overall inversion capabilities, both in terms of spatial resolution (width of the kernel) and depth range. The improvement is most significant for smaller ranks (top and middle plots) as these include the most dominant eigenmodes only, and those are relatively less sensitive to shallower regions. The 'quality' of kernels when using larger rank (bottom plot) is very similar with and without redundancy, as eigenmodes corresponding to smaller singular values that carry shallower region sensitivities are also included.

Given that the inversion capabilities, with and without redundancy in $\mathbf{R}_{\mathrm{T}}$, are very similar when using larger rank, it might seem plausible to argue that the two approaches would eventually produce similar inversion results. This is not correct as the quality of the final inversion after iterations depends on incremental updates in the 'right direction' over multiple inversion cycles. Whether or not an inversion solution (in a given cycle) is in the 'right direction' in turn depends on the error contribution to the solution. As mentioned in previous chapters, solutions obtained using lower rank early in the iteration cycle are less likely to be error dominated. Depending on the amount of error in the system (from higher order terms and/or observational noise) the highest rank may not be realized, even in the final iteration. Thus, using $\mathbf{R}_{\mathrm{T}}$ with 'non-redundant' response functions can significantly improve the overall inversion quality.

5.2 Effect of $\mathbf{R_T}$ redundancy on inversion quality

In this section, we discuss the dependence of the quality of inversion on the redundancy in $\mathbf{R}_{\mathrm{T}}$. The goal here is to get an insight into what happens to the solution when we use matrix with incrementally less redundant response functions. For this experiment, we employed iterative-OLA method to invert artificially constructed Gaussian perturbation (red curve in Figure 5.3) using

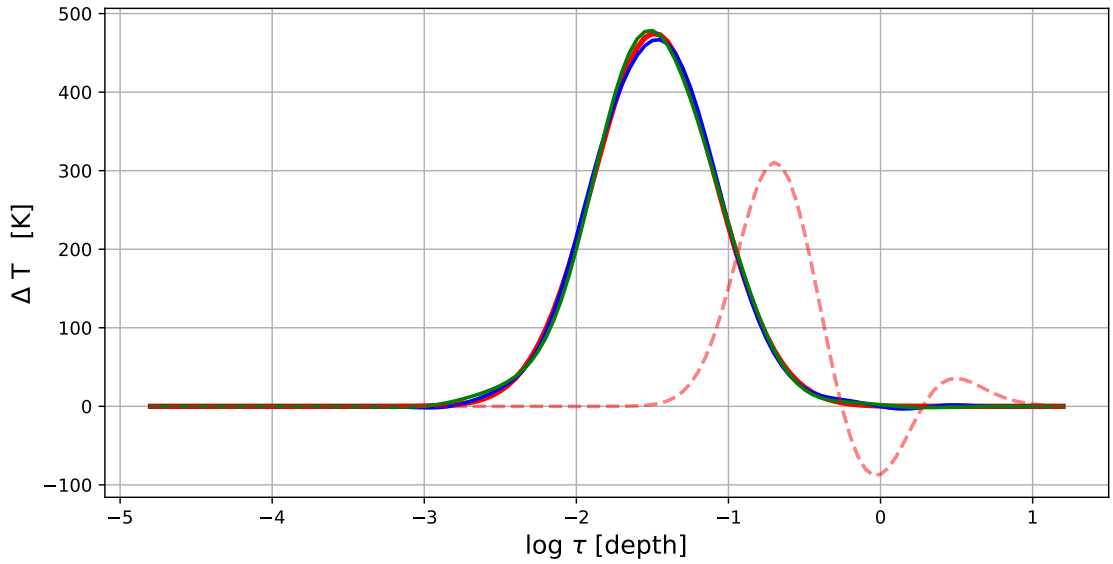

Figure 5.3: Underlying Gaussian shaped perturbation with peak location at log $\tau = -1.5$ and width $= 0.4$ Δlog τ, is shown in red. Iterative-OLA inversion result obtained using all spectral lines, with all the redundancies in $\mathbf{R}_{\mathrm{T}}$, is shown by the red-dashed curve. Inversion result obtained (using all spectral lines) after removing redundancy (using $p_3 = 5\%$) is shown by the blue curve. That obtained using the best 3 spectral line-set of Section 5.3 is shown by the green curve ($p_3 = 5\%$).

response function matrix with different levels of redundancy (computed based on the approach described in Appendix 5.5). Note, that a larger value for redundancy parameter p_3 (defined in Appendix 5.5) means that the 'new' $\mathbf{R}_{\mathrm{T}}$ matrix has lesser redundancy. It only includes response functions with normalized difference of at least p_3 %.

In implementation, for a given inversion cycle, we compute the response functions at all wavelengths and remove the redundant ones that comply with a prescribed p_3 value. Using this 'non-redundant' $\mathbf{R}_{\mathrm{T}}$, we construct kernels and invert at 'all possible' depths. We repeat the process and use the same p_3 value in the subsequent inversion cycles. Given that the guess-model (and the corresponding $\mathbf{R}_{\mathrm{T}}$) are different in each cycle, it is likely that the 'new' non-redundant $\mathbf{R}_{\mathrm{T}}$ (in each cycle) is comprised of a different set of wavelengths. After arriving at a final inversion solution, we compute the inversion quality metric based on the L1 norm of the difference between the actual (underlying) and inverted $\mathbf{T}$ i.e. $\|\text{actual} - \text{inverted } \mathbf{T}\|_1$.

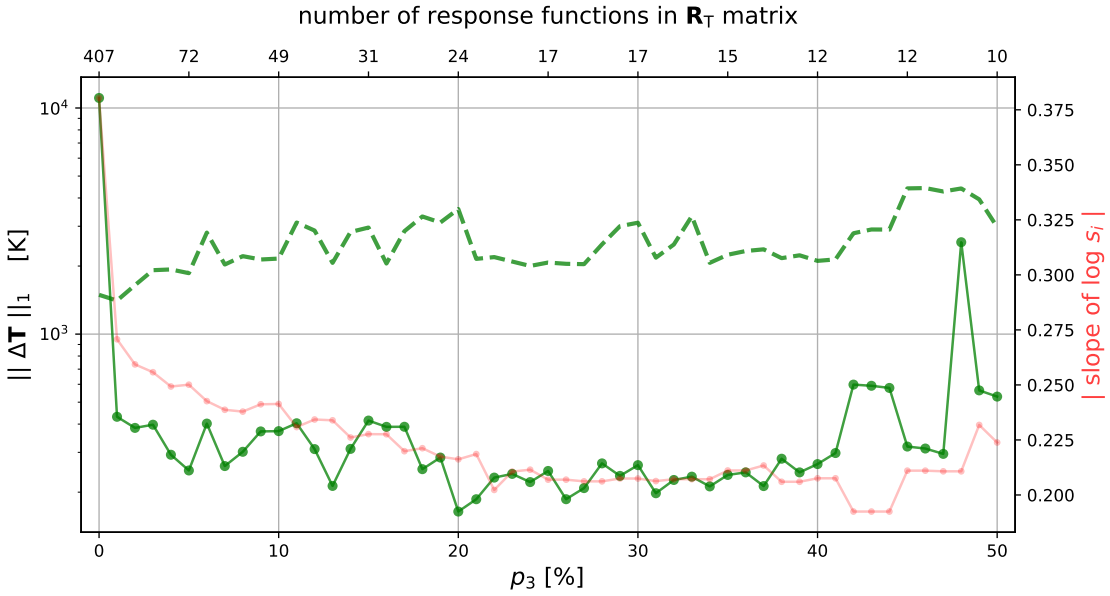

Figure 5.4: Inversion quality vs. redundancy parameter p_3, for the perturbation in Figure 5.3, is shown by green-dotted curve. Similar curve obtained for the Gaussian perturbation, with peak located at $\log \tau = 0.25$, perturbation width = 0.3 $\Delta \log \tau$, is shown by the green-dashed curve. For both perturbations, inversion results are obtained using all spectral lines. Red curve corresponds to absolute value of the slope of the singular value curve vs. p_3.

The relationship between inversion quality and p_3 is shown by the green-dotted curve in Figure 5.4. Note that $p_3 = 0$ means that redundancy is not removed from $\mathbf{R}_T$. It is clear that the inversion quality improves significantly when using non-redundant matrix to invert the perturbation in Figure 5.3. The drastic early improvement is expected as the underlying perturbation lies in the shallower region of the domain, and doesn't 'necessarily require' the redundant response functions which are mostly sensitive to deeper regions. For non-zero p_3 values, it is the deeper region sensitive redundant response functions that primarily get removed, resulting in the dominant eigenmodes that are more sensitive to shallower regions, improving the ability to invert there. In Figure 5.3, we show that the solution obtained using 'non-redundant' matrix (green, $p_3 = 5\%$) overlays the underlying perturbation, while that obtained without removing any redundancies (red-dashed, $p_3 = 0\%$) struggles to recover it.

Using too large value for p_3 eventually removes response functions that are dissimilar, which

degrades the overall inversion capability. This is evident from the worsening of the inversion quality for $p_3 > 40\%$. Thus, there is a trade-off. Using too small value for p_3 doesn't entirely remove the redundancies in $\mathbf{R}_{\mathrm{T}}$ while using too large value results in a matrix that contains lesser overall sensitivity, degrading its ability to do good inversions. The p_3 value at which we move from one limit to another depends on the underlying perturbation, particularly its depth. This is demonstrated by the green-dashed curve in Figure 5.4 which corresponds to the inversion quality metric vs. p_3 when inverting Gaussian perturbation located at $\log \tau = 0.25$. For this case, the inversion result only slightly improves for $p_3 = 1\%$ and worsens for larger values, as inverting this perturbation requires deeper sensitive response functions.

These behaviors make it difficult to determine the optimal response function set to use. Removing the sensitivity bias without removing 'needed' response functions should improve the overall inversion capability. Ongoing work aims to determine the optimal depth dependent strategy while accounting for multivariable dependencies and observational noise.

5.3 Determining best line combination based on singular value slope

The OLA methodology allows quantitative assessment of different line combinations for potential inversion. Given a set of n spectral lines, we aim to determine the best x line combination to produce best overall inversion. In Section 2.2.2, we suggested that spectral line combinations can be assessed based on the minimum width averaging kernel that can be constructed at a given depth for a given variable. It quickly becomes difficult to objectively compare the overall inversion capability over multiple depths using this metric, as different combinations may perform differently at different depths. So, unless there is a particular depth we are interested in, it is tricky to deduce which combination is good overall solely based on the kernel widths.

Here, we demonstrate that the slope of the $\mathbf{R}_{\mathrm{T}}$ matrix singular value curve ($\log s_i$ vs. i^{th} mode, see Figure 2.4) for different line combinations can be used as an objective metric to find the best line combination. This is motivated by the decreasing absolute slope of the singular value curve (red dotted in Figure 5.4) with decreasing redundancy in $\mathbf{R}_{\mathrm{T}}$ (increasing p_3 value). A matrix

with lower redundancy has a smaller singular value slope because the underlying response functions are dissimilar. It is expected that the line combinations with the most dissimilar response functions (smallest slope) are likely to be the most capable at doing inversions. The slope can thus be used as a metric to objectively compare line combinations.

In order to demonstrate that singular value slope can indeed be used to find best x line combinations out of n total lines, we use the spectral lines (including blends) listed in the Table A.1. Our goal is to find the best 3 line combination out of the 7 total. For the perturbation (red curve) plotted in Figure 5.3 we independently invert using all possible 3 line combinations using the approach mentioned above, with $p_3 = 5\%$. Once the inversion is done for a given line combination we compute the inversion quality metric based on the L1 norm of the difference between the actual and inverted $\mathbf{T}$ i.e. $\|\text{actual} - \text{inverted } \mathbf{T}\|_1$ (this metric is same as that used in previous section). We also compute the slope of the singular value curve for the corresponding response function matrix (for mean MURaM starting guess-model), using the largest singular values that add up to 95% of the total sum. Note that it is critical to compute the slope after removing the redundancy from the matrix. Without doing so, the slope is dominated by the matrix redundancy and does not reflect the orthogonality of the useful response functions.

The plot between the inversion quality metric and the absolute value of singular value slope is shown by green-dots in Figure 5.5. It is evident from the plot that the line combinations with smallest absolute slopes are able to produce best quality inversion solution. The line combination that could best recover the perturbation is comprised of Fe II 6147.7 Å, Fe II 6149.2 Å and Fe I 6301.5 Å, including corresponding blends (see Table A.1). The inversion solution $\Delta\mathbf{T}$ obtained using this 'best' line combination is shown in green in Figure 5.3 (and overlays the underlying perturbation). The larger symbols in the Figure 5.5 correspond to the inversion results obtained using all the 7 spectral lines, with (red) and without (blue, $p_3 = 5\%$) redundancy. We note that there is an outlier case which is not able to recover the perturbation at level similar to that achieved by other combinations in this slope range (see the green dot at slope of 0.25 and L1 norm of $\Delta\mathbf{T}$ around 6000 K in Figure 5.5). For this case, we found that after a few inversion cycles the OLA

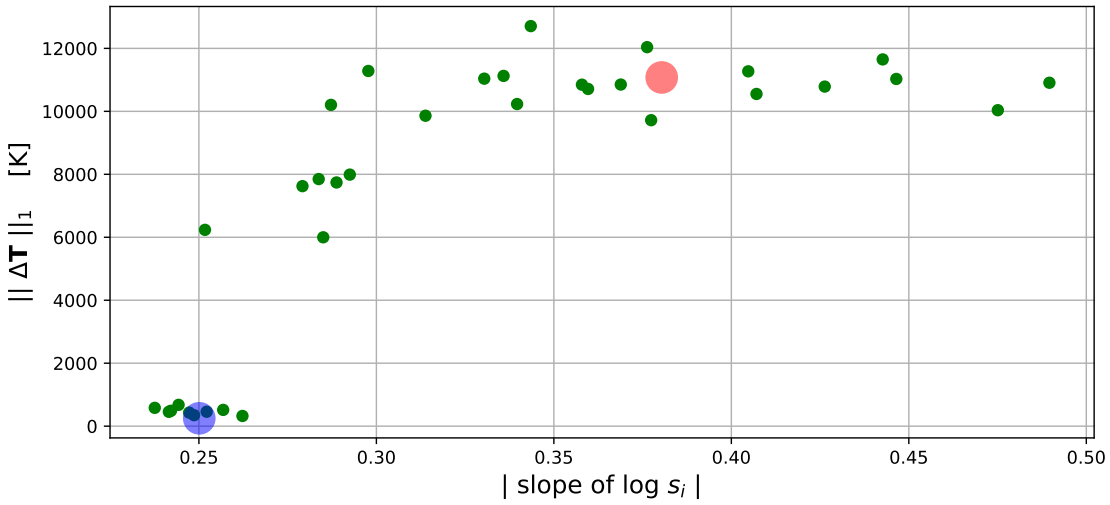

Figure 5.5: Inversion quality metric vs. slope for all 3 line combinations (out of the 7 total mentioned in Table A.1) is depicted by green-dots. Redundant response functions are removed from $\mathbf{R}_{\mathrm{T}}$ using $p_3 = 5\%$. The bigger dots correspond to inversions done using all spectral lines with (red) and without (blue, $p_3 = 5\%$) redundancy.

inversion window shrunk (instead of widening). This resulted in the 'edge-effect' errors to corrupt the solution which eventually resulted in a bad inversion. This suggests that the actual inversion quality is very case specific and that singular value slope can only be used to make initial/rough assessments of which combinations are most likely to produce good overall inversions. Moreover, the best line combinations may differ if a different guess-model is used.

We suspect using the singular value slope as a comparison metric only works when comparing line combinations from a common pool of lines. Further, the slope only reflects the relative distribution of orthogonal sensitivities within the matrix, not the depths which different response functions probe. Line combinations that are sensitive to very different depths may have the same slope. However, information about to what depths response functions are sensitive to is contained in the $\mathbf{u}_i$ eigenmodes. This is exploited in the kernel construction and can be used to gain insight into what the inversion potential for a given line combination might look like (see Figure 5.6). For the line combinations that produced the best inversion result in Figure 5.5, the averaging kernel width vs. depth curve computed for the mean MURaM model (after removing redundancy using

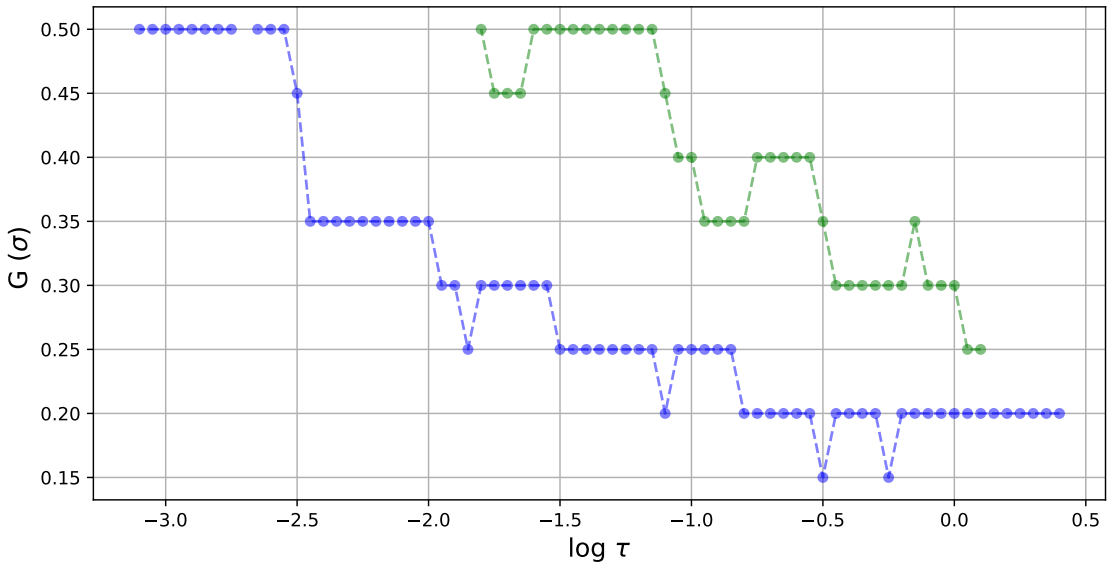

Figure 5.6: Minimum averaging kernel width vs. depth curve for the best 3 line combination found in Section 5.3. Kernel widths, constructed using rank k determined by the dominant singular values that add up to 95% and 99.9%, are shown in green and blue, respectively. For both cases, redundancy from the matrix is removed using $p_3 = 5\%$.

$p_3 = 5\%$) is shown in Figure 5.6. The two curves correspond to different ranks based on the dominant singular values that add up to 95% (green) and 99.9% (blue). Ideally, these curves give an estimate of the range of inversions capabilities of the line combinations, assessed in terms of the depth range (OLA inversion window) and the corresponding depth resolution (kernel width). It is important to reemphasize that these are rough estimates and exact inversion quality would be case dependent.

5.4 Summary

In this chapter, we demonstrated that redundancies in the response function matrix (e.g. $\mathbf{R}_\mathrm{T}$) degrades the overall inversion capability. Redundancy results from a large fraction of wavelengths corresponding to continuum intensities for which the response functions are 'almost identical'. This leads to the dominant eigenmodes to have biased depth sensitivity. This degrades the ability to invert for the properties of shallower regions using a lower rank *pseudo-inverse*. We demonstrated

that a workaround to this issue is to artificially remove these redundant response functions. This yields dominant eigenmodes that are 'similarly' sensitive to different depths and thus improves the overall global inversion capability. Thus, using more spectral lines/wavelengths does not necessarily improve inversions.

The challenge faced is to optimally identify and remove redundant response functions. Conservatively removing the most similar response function may not be sufficient and liberally removing them may impact sensitivity and degrade the overall inversion capability. Moreover, whether or not a response function is redundant depends on the underlying perturbation. This makes it non-trivial to determine an optimal way to remove redundancy. From this work, we suspect that removing the sensitivity bias should improve the overall inversion capability. We also expect that other inversion methods e.g. SIR/RLS could benefit from this idea. To optimally identify and remove 'redundant' response functions, however, for single variable and multivariable system and in the presence of observational noise, is future work.

We also demonstrated that the slope of the singular value curve (after removal of the redundant response functions) is a quantitative metric of the inversion potential of different spectral line combinations. Once the best line-set is identified, the averaging kernel width provides insight into what the inversion capability is with depth. Note that these are estimates and the best line combination and the inversion capability is ultimately case dependent. They are however useful because no a posteriori measure of the inversion quality is typically available. Further, the metrics are not tied to any particular inversion approach as they do not require an inversion to be done. They can thus be used irrespective of the choice of inversion method. Determining if singular value slope can consistently find best line-combinations in more complicated situations e.g. multivariable system, spectral noise, etc., is a part of ongoing effort.

5.5 Appendix: $\mathbf{R_T}$ redundancy removal parameter p_3

In order to identify if response functions, say, at wavelengths λ_j and λ_k, are redundant or not, we used the following "redundancy removal metric":

$$\left\| \frac{\mathrm{R_T}(\lambda_j)}{\|\mathrm{R_T}(\lambda_j)\|_1} - \frac{\mathrm{R_T}(\lambda_k)}{\|\mathrm{R_T}(\lambda_k)\|_1} \right\|_1 \times 100 \tag{5.1}$$

Here, $\|\mathrm{R_T}(\lambda_j)\|_1$ corresponds to the L1 norm of response function at λ_j and approximates the area (assuming linear interpolation) under absolute value response function $|\mathrm{R_T}(\lambda_j)|$. Similarly, $\|\mathrm{R_T}(\lambda_k)\|_1$ approximates the area under $|\mathrm{R_T}(\lambda_k)|$. The metric computes L1 norm of the difference between the area normalized response functions. Normalization is done to consider the fact that response functions that only differ by a constant factor are essentially the 'same' and carry similar sensitivity information (with different amplitudes). Thus the metric can be interpreted as a % difference between the two response functions. The response functions are marked redundant if the metric is smaller than a user defined redundancy parameter p_3. Note that the metric serves the purpose of identifying dissimilar response functions but, in detail, will fail to recognize response functions as similar if they differ by a constant negative factor. This is not an issue here as none of the temperature response functions fall into this category (see top plot in Figure 5.1). It would be future endeavor to figure out a more robust metric.

Chapter 6

Summary and Future work

6.1 Brief thesis summary

In this thesis, we, for the first time, applied the Optimally Localized Averages (OLA) inversion method to spectroscopic data to invert for the depth dependent thermodynamic parameters of the solar photosphere, namely, $\mathbf{T}$, $\mathbf{V_{los}}$, and $\mathbf{P_e}$. The basic approach to inversions (as discussed in Chapter 2) is to start with an initial guess-model and solve for the depth dependent model differences (e.g. $\frac{\Delta \mathbf{T}}{\mathbf{T}}$) between the underlying (actual, observed) and the guess-model that accounts for the spectral differences ($\Delta \mathbf{I}$) between the observed and the guess-model spectra. Typically, the spectral differences are related to the corresponding model differences by linear response functions (e.g. $\mathbf{R}_{\mathrm{T}}$). For a set of wavelengths, the relationship can be written as a 1st order linear system of Equations 2.5. This linear system is only approximate. There are inherent non-zero error $\boldsymbol{\varepsilon}$ contributions from the omitted higher order terms.

Solving the approximate system requires computing the inverse of the response function matrix $\mathbf{R}_{\mathrm{T}}$. This is non-trivial, as the underlying system is severely ill-posed system, as evident from the exponential decay of the singular values of the matrix (see Figure 2.4). This severe ill-posedness is due to redundancies in the spectral line formation resulting in the response functions (that make up the response function matrix) to have similar sensitivity information. Ill-posedness combined with non-zero error $\boldsymbol{\varepsilon}$ results in the employable number of linear independent equations to be much smaller than the total number of unknowns ($\frac{\Delta \mathbf{T}}{\mathbf{T}}$) we intend to invert for. This means that the system is 'effectively' underdetermined and one cannot uniquely solve for $\frac{\Delta \mathbf{T}}{\mathbf{T}}$. The ill-posed

nature also means that the numerical rank of the matrix is ill-determined and naively computing its *pseudo-inverse* (approximate inverse) using arbitrary rank will likely result in an inverse matrix with larger amplitude elements which can amplify error ε, resulting in error dominated solutions. These error dominated solutions are highly oscillatory and lack physical significance.

To obtain a physically meaningful solution (not dominated by error), some sort of regularization is employed, and a lower rank version of the response function matrix is inverted. This removes contributions from smaller singular values which would otherwise yield larger amplitude terms in the *pseudo-inverse* matrix. The obtained solution depends heavily on the 'amount' of regularization. Over-regularization removes many smaller singular values (and eigenmodes), and leads to solutions that are smoother but fails to capture the sharp gradients in the underlying atmosphere (if present). Under-regularization improves sensitivity of these gradients, but results in error amplification. Determining the 'optimal' regularization to balance resolution vs. error amplification is one of the hardest tasks when carrying out inversions. This is because the spectral difference metric used to assess the inversion quality (how well the underlying perturbation is recovered) is flawed. Due to the inherently underdetermined nature of the problem, inversions with different regularization can produce equally good fit spectra.

Current state of the art spectropolarimetric inversion methods (e.g. SIR) aim to obtain globally smooth solutions by inverting at a limited number of user-defined depth locations (nodes). This, by design, ensures that the inverted solutions are non-oscillatory below nodal scales. However, the number of nodes utilized, which is decided based on user experience, limits the inversion depth resolution. MURaM simulations of the solar photosphere show gradients at scales much smaller than those recoverable using the standard SIR node values. Further, the inversion solutions most likely do not correspond to the 'true resolution limit' that can be recovered using the spectropolarimetric data, particularly that which will be available from the upcoming DKIST. Determining the inversion resolution limit that is achievable at each depth, and inverting at that resolution is critical to using DKIST at its full potential. This is the goal of the OLA inversion method, to find the 'best possible' inversion solution at each depth, based on how localized a solution can be computed at that depth.

It is critical to emphasize that one should be mindful of what solution is required and accordingly decide on what inversion method should be employed. Results obtained from different inversion approaches may lead to similarly good fit observed spectra (due to the underdetermined nature of the problem) but may be quite different from one another (and from the underlying perturbation). This is because different approaches are influenced by different types of error e.g. SIR solutions obtained using limited number of nodes are subject to cross-talk errors from other depths and variables. OLA actively tries to minimize such errors, and though they are not completely eliminated, solutions are more likely to be dominated by error from the higher order terms ignored in the linear response function formulation. In addition, solutions using our current version HOLA are dominated by the edge-effect issue if non-linear shaped large-scale offsets are present.

In Section 2.2, we introduced the OLA method to invert for temperature perturbations (single variable) for artificially constructed test cases. Unlike SIR/RLS, where one simultaneously inverts for all depths, OLA inversions are done for one location at a time with the help of averaging kernels. The width of the kernel dictates the resolution of the obtained solution at a given depth. The process is repeated for each depth to invert at 'all' depth locations. There are depths at which kernels cannot be constructed, as the 'amount' of orthogonal information in the $\mathbf{R}_{\mathrm{T}}$ matrix is non-uniformly distributed across depths. This failure usually occurs above and below a limit range of depths, defining the 'OLA inversion window'. The range of depths over which we can invert using OLA, and the corresponding kernel widths at those depths, depends on the rank (number of eigenmodes) used when computing the *pseudo-inverse* matrix (when solving for coefficients using Equation 2.9). A larger rank allows us to construct narrower width kernels over a larger depth range, but with the caveat that the solutions are more likely to be error dominated. Thus, the question of what rank to use, or in general, 'how much' to regularize, remains. This would not be an issue if we had robust error estimates, but this is not possible, as the error introduced by the higher order terms, itself depends on the magnitude of underlying $\frac{\Delta \mathbf{T}}{\mathbf{T}}$ we aim to capture.

In Section 2.2.4, we developed an iterative OLA scheme where we aim to 'slowly' approach to the optimal rank achievable given the data. Iterative approach allows us to invert non-linear

perturbations (when $\frac{\Delta \mathbf{T}}{\mathbf{T}}$ is large) using linear response functions, extending the capability of the original method. But there is an inherent difficulty with iterative-OLA when the underlying perturbation has large-scale offsets. This has to do with the finite width of the OLA inversion window (it does not span the entire depth domain) combined with the fact that the width of the averaging kernel is not a δ-function. When making iterative updates only to depths 'inside' the inversion window, there is a leakage of information ($\frac{\Delta \mathbf{T}}{\mathbf{T}}$) from outside of the inversion window to the inside, due to the finite width of the kernels. This can corrupt the entire solution. We termed this the 'edge-effect' issue. It defeats the very strength of OLA where the method aims to prevent such leakage by focusing on keeping the information ($\frac{\Delta \mathbf{T}}{\mathbf{T}}$) where it belongs. In spite of the efforts already made, resolution of edge-effect remains. In Section 6.2 below, we briefly discuss those efforts and future directions.

In Chapter 3, we statistically assessed single variable inversion capabilities of the HOLA method, and compared it with SIR. To make this assessment, we inverted a sufficiently large number of widely differing semi-real MURaM atmospheres. Using the mean MURaM as the starting guess-model, the goal was to see how well individual atmospheres can be recovered using HOLA (and SIR). We inverted individual MURaM columns using HOLA (and SIR) and computed the difference between the underlying atmosphere and the inverted model (for the given variable). Both methods produce very similar inversion results and achieve good overall inversion in $\log \tau \in [-2, 0]$ (for each variable). Even though the average inversion quality is very similar for these methods, the underlying cause of error is very different. The source of error in SIR is its inability to recover higher spatial frequency offsets, while HOLA struggles with the edge-effect issue when the underlying perturbation has large-scale non-linear offsets.

In Chapter 4, we extended the HOLA method to invert more realistic multivariable system. The goal here is to 'simultaneously' invert for $\mathbf{T}$, $\mathbf{V_{los}}$ and $\mathbf{P_e}$, assuming that these thermodynamic variables completely define the system. The 1st order equation for the multivariable system states that the spectral differences $\mathbf{\Delta I}$ between the underlying and guess-model spectra corresponds to the model differences from all variables weighted by their respective response functions (with error

contributions from the omitted higher order terms for each variable and spectral noise). Unlike SIR (or RLS), where one simultaneously inverts for all variables at all depth locations with the goal to attain a globally smooth solution, OLA (within the HOLA framework) inverts for 1 variable at 1 depth location at a time. The goal here is to compute linear coefficients which constructs narrow width averaging kernels at a given depth location (for the variable we intend to invert) and simultaneously minimizes cross-talk variable sensitivities. The computed inversion solution for this variable (at this depth) then has minimized cross-talk error contributions from other depth locations (from same variable perturbations) and from cross-talk variables.

The main difficulty faced, and common to all inversion methods, is when using the *pseudo-inverse* matrix to invert variables in a multivariable system. This has to do with the inherent spectral sensitivity bias between different variables as evident from their differing response functions magnitudes e.g. amplitude of response functions in $\mathbf{R}_{\mathrm{T}}$ is about 30 times larger than $\mathbf{R}_{\mathrm{P_e}}$, and about 3 times larger than $\mathbf{R}_{\mathrm{V_{los}}}$. This bias results in the dominant eigenmodes of the giant matrix to be mostly sensitive to $\mathbf{R}_{\mathrm{T}}$, as compare to $\mathbf{R}_{\mathrm{P_e}}$. For example, this makes it harder to invert for $\mathbf{P_e}$ using a lower rank *pseudo-inverse* matrix as the dominant modes contain little to no $\mathbf{R}_{\mathrm{P_e}}$ sensitivity. We developed a workaround to this issue by manually amplifying/de-amplifying cross-talk variable response function matrices to make their amplitude 'similar' to that of the variable we intend to invert. This results in the dominant eigenmodes to have similar sensitivity across all variables and allows for $\mathbf{A}_{\mathrm{P_e}}$ construction, in the presence of temperature response functions, without using too many eigenmodes. We demonstrated that using amplification factors allows us to construct $\mathbf{A}_{\mathrm{P_e}}$ (with smaller eigenmodes) and gives us a better chance at inverting electronic pressure in a multivariable system with more spectrally sensitive variables.

We concluded the thesis with Chapter 5 where we investigated how redundancies in the response function matrix degrades its overall inversion capability. These redundancies are due to the presence of large fraction of wavelengths that correspond to continuum intensities and have almost identical response functions. The corresponding dominant eigenmodes of the response function matrix are biased and are more sensitive to deeper regions to which redundant response functions

are mostly sensitive to. This degrades our ability to invert in shallower regions using a lower rank *pseudo-inverse*. This is similar to the issue faced when we try to invert for electronic pressure in the presence of temperature using smaller rank. We demonstrated that the redundancy bias can be mitigated by artificially removing these redundant response functions from the matrix. This results in the dominant eigenmodes (corresponding to redundancy bias removed matrix) to be similarly sensitive to 'all' response functions including the ones that are sensitive to shallower depths, improving the overall inversion capability.

The challenge now faced is how to optimally identify and remove redundant response functions. If we are too conservative when identifying (and removing) the most similar response function then the bias issue may still remain, while if we are too liberal and remove too many 'dissimilar' response functions that correspond to 'good' sensitivity information in the matrix then the overall inversion capability gets degraded. Moreover, whether or not a response function is redundant depends on the depth of the underlying perturbation being inverted. These trade-offs make it non-trivial to determine an optimal way to remove the bias from the matrix. To optimally identify and remove 'redundant' response functions, for single variable and multivariable system, and in the presence of observational noise, would be future endeavor. All inversion methods e.g. SIR/RLS should be equally benefited from further development of this idea.

Finally, we demonstrated that the slope of the singular value curve (once the redundancy bias is removed somehow) can be used as a metric to quantitatively compare the inversion capability of different spectral line combinations. We used this metric to find the best x line combination (out of n total lines) that has the most potential to produce best inversion results. Once the best line combination is identified, the minimum averaging kernel width vs. depth can be employed to get an insight into what the inversion capability may be. Even though these estimates are approximate, as they depend on the guess-model atmosphere, such metrics can still serve as a good starting point. Moreover, the metrics do not require any inversion to be done and thus can be used irrespective of the choice of inversion method. Determining whether slope can identify best line-combination in more complicated situations e.g. for multivariable system, in the presence of spectral noise, etc.,

would be a part of our future work.

Our future work also includes estimating error in the inverted solutions, inverting magnetic field vector from spectropolarimetric data and applying the method to real observations, modifying OLA to actively minimize error from the higher order terms to further widen the range of perturbations that can be inverted using this method.

6.2 Future work: Resolution of the Edge-effect

In addition to the future work on spectral line selection and wavelength redundancy indicated above, resolution of the edge-effect issue remains. We discuss it separately here in order to give justice to its difficulty, clearly outline efforts already made, where these fail and future directions.

As discussed in Section 2.2.5, to get around the edge-effect issue, we initially employed skewed target functions to suppress the sensitivity of the target functions outside the OLA inversion window. But given that kernels don't perfectly mimic target functions, the issue of leakage remains. We realized it might be better to make updates outside the inversion window, as the 'edge-effect' issue is a consequence of OLA method's inability to invert outside the window. To achieve this, we initially employed flat averaging kernels to compute large-scale average of the underlying perturbations, and made inversion updates at all depths with this average. The large-scale updates were interleaved in-between high-resolution localized OLA inversions. While this helped with inversions significantly, some difficulties still remained.

We ultimately pursued a SIR+OLA hybrid approach (HOLA) to recover large-scale constant and linear trends using SIR (with limited nodes) and high-resolution small-scale updates using OLA. This method does not suffer the same issues faced by the flat kernels approach. The method works well if the underlying large-scale offset is constant/linear with $\log \tau$, but may fail otherwise. We find models in MURaM simulations that differ from this assumption. It would be reasonable to think of making SIR large-scale updates using the largest 'allowed' node values, as SIR is good at recovering these large-scale offsets, and then make high-resolution small-scale adjustments using OLA. The caveat of this approach is that SIR itself aims to find solutions such that $\mathbf{\Delta I} \rightarrow 0$, and

once $\mathbf{\Delta I} \approx 0$ (a likely scenario when using largest allowed node values), it would be practically impossible to make further inversion updates using OLA.

Finding a more robust solution to the edge-effect issue to successfully invert non-linearly shaped large-scale perturbations using HOLA would be future endeavor. Here, we suggest a few potential ways in which this could be achieved. A general behavior of edge-effect dominated solutions is that they first become oscillatory near the OLA inversion window edge and grows uncontrollably large in amplitude with iteration. This eventually results in the entire solution to become oscillatory (unless spectral differences accordingly become worse and stop the iteration). We suspect that this oscillatory behavior (and successive large growth in inversion amplitude) can be exploited to identify once solutions start to become error dominated. Another potential solution to the edge-effect issue would be to employ the RLS method, instead of SIR, to make large-scale updates. We suspect that a smaller rank RLS inversions should be better equipped to 'adjust' according to the underlying perturbations, as we don't have to upfront decide on the order of the large-scale update (in context of shape with log τ, defined by number of nodes in SIR) that we intend to obtain. It might also be worth considering making large-scale updates only outside the OLA inversion window using SIR (with largest 'allowed' nodes), or RLS.

Bibliography

[1] Eugene H. Avrett and Rudolf Loeser. Models of the Solar Chromosphere and Transition Region from SUMER and HRTS Observations: Formation of the Extreme-Ultraviolet Spectrum of Hydrogen, Carbon, and Oxygen. The Astrophysical Journal Supplement Series, 175(1):229–276, 2008. doi:10.1086/523671.

[2] G. Backus and F. Gilbert. Uniqueness in the Inversion of Inaccurate Gross Earth Data. Philosophical Transactions of the Royal Society of London Series A, 266(1173):123–192, March 1970. URL: https://ui.adsabs.harvard.edu/abs/1970RSPTA.266..123B, doi:10.1098/rsta.1970.0005.

[3] George Backus and Freeman Gilbert. The Resolving Power of Gross Earth Data. Geophysical Journal, 16(2):169–205, October 1968. URL: https://ui.adsabs.harvard.edu/abs/1968GeoJ...16..169B, doi:10.1111/j.1365-246X.1968.tb00216.x.

[4] George E Backus and JF Gilbert. Numerical applications of a formalism for geophysical inverse problems. Geophysical Journal International, 13(1-3):247–276, 1967.

[5] Sarbani Basu. Global seismology of the Sun. Living Reviews in Solar Physics, 13(1):2, 2016. doi:10.1007/s41116-016-0003-4.

[6] Åke Björck. Numerical Methods for Least Squares Problems. Society for Industrial and Applied Mathematics, 1996. URL: https://epubs.siam.org/doi/abs/10.1137/1.9781611971484, arXiv:https://epubs.siam.org/doi/pdf/10.1137/1.9781611971484, doi:10.1137/1.9781611971484.

[7] Richard C Canfield. The height variation of granular and oscillatory velocities. Solar Physics, 50(2):239–254, 1976. doi:10.1007/BF00155287.

[8] Fausto Cattaneo. The Solar Dynamo Problem, pages 201–222. Springer Netherlands, Dordrecht, 1997. doi:10.1007/978-94-011-5167-2_21.

[9] J. Christensen-Dalsgaard, P. C. Hansen, and M. J. Thompson. Generalized singular value decomposition analysis of helioseismic inversions. Monthly Notices of the Royal Astronomical Society, 264(3):541–564, 10 1993. arXiv:https://academic.oup.com/mnras/article-pdf/264/3/541/3478967/mnras264-0541.pdf, doi:10.1093/mnras/264.3.541.

[10] J. Christensen-Dalsgaard, J. Schou, and M. J. Thompson. A comparison of methods for inverting helioseismic data. Monthly Notices of the Royal Astronomical Society, 242(3):353–369, 06 1990. arXiv:https://academic.oup.com/mnras/article-pdf/242/3/353/3863448/mnras242-0353.pdf, doi:10.1093/mnras/242.3.353.

[11] J. Christensen-Dalsgaard and M. J. Thompson. A Hands-On IDL Program for Helioseismic Inversion. In Timothy M. Brown, editor, GONG 1992. Seismic Investigation of the Sun and Stars, volume 42 of Astronomical Society of the Pacific Conference Series, page 249, January 1993. URL: https://ui.adsabs.harvard.edu/abs/1993ASPC...42..249C.

[12] National Research Council. Understanding the Sun and Solar System Plasmas: Future Directions in Solar and Space Physics. The National Academies Press, Washington, DC, 2004. URL: https://www.nap.edu/catalog/11188/understanding-the-sun-and-solar-system-plasmas-future-directions-in, doi:10.17226/11188.

[13] S. Danilovic, M. Schüssler, and S. K. Solanki. Probing quiet Sun magnetism using MURaM simulations and Hinode/SP results: support for a local dynamo. Astronomy & Astrophysics, 513:A1, April 2010. arXiv:1001.2183, doi:10.1051/0004-6361/200913379.

[14] S. Danilovic, M. van Noort, and M. Rempel. Internetwork magnetic field as revealed by two-dimensional inversions. Astronomy & Astrophysics, 593:A93, September 2016. arXiv:1607.00772, doi:10.1051/0004-6361/201527842.

[15] J. C. Del Toro Iniesta and B. Ruiz Cobo. Stokes Profiles Inversion Techniques. Solar Physics, 164(1-2):169–182, March 1996. URL: https://ui.adsabs.harvard.edu/abs/1996SoPh..164..169D, doi:10.1007/BF00146631.

[16] Jose Carlos del Toro Iniesta. Introduction to Spectropolarimetry. Cambridge University Press, 2003. doi:10.1017/CBO9780511536250.

[17] Jose Carlos del Toro Iniesta and Basilio Ruiz Cobo. Inversion of the radiative transfer equation for polarized light. Living Reviews in Solar Physics, 13(1):4, November 2016. URL: https://ui.adsabs.harvard.edu/abs/2016LRSP...13....4D, arXiv:1610.10039, doi:10.1007/s41116-016-0005-2.

[18] O. Gingerich, R. W. Noyes, W. Kalkofen, and Y. Cuny. The Harvard-Smithsonian reference atmosphere. Solar Physics, 18(3):347–365, July 1971. URL: https://ui.adsabs.harvard.edu/abs/1971SoPh...18..347G, doi:10.1007/BF00149057.

[19] G. H. Golub and C. F. Van Loan. Matrix Computations. The Johns Hopkins University Press, Baltimore, MD, 3rd edition, 1996. URL: https://twiki.cern.ch/twiki/pub/Main/AVFedotovHowToRootTDecompQRH/Golub_VanLoan.Matr_comp_3ed.pdf.

[20] D O Gough. Internal rotation and gravitational quadrupole moment of the Sun. Nature, 298(5872):334–339, 1982. doi:10.1038/298334a0.

[21] Douglas Gough. Inverting helioseismic data. Solar Physics, 100(1):65–99, 1985. doi:10.1007/BF00158422.

[22] David F. Gray. On the Existence of Classical Microturbulence. The Astrophysical Journal, 184:461–472, September 1973. URL: https://ui.adsabs.harvard.edu/abs/1973ApJ...184..461G, doi:10.1086/152344.

[23] David F. Gray. The Observation and Analysis of Stellar Photospheres. Cambridge University Press, 3 edition, 2005. doi:10.1017/CBO9781316036570.

[24] Per Christian Hansen. The discrete picard condition for discrete ill-posed problems. BIT Numerical Mathematics, 30(4):658–672, 1990. doi:10.1007/BF01933214.

[25] Per Christian Hansen. Truncated singular value decomposition solutions to discrete ill-posed problems with ill-determined numerical rank. SIAM Journal on Scientific and Statistical Computing, 11(3):503–518, 1990. arXiv:https://doi.org/10.1137/0911028, doi:10.1137/0911028.

[26] Per Christian Hansen. Analysis of discrete ill-posed problems by means of the l-curve. SIAM Review, 34(4):561–580, 1992. arXiv:https://doi.org/10.1137/1034115, doi:10.1137/1034115.

[27] Per Christian Hansen. Rank-deficient and discrete ill-posed problems: numerical aspects of linear inversion. SIAM, 1998.

[28] Richard J. Hanson. A numerical method for solving fredholm integral equations of the first kind using singular values. SIAM Journal on Numerical Analysis, 8(3):616–622, 1971. URL: http://www.jstor.org/stable/2949679.

[29] W. Jeffrey. Inversion of Helioseismology Data. The Astrophysical Journal, 327:987, April 1988. URL: https://ui.adsabs.harvard.edu/abs/1988ApJ...327..987J, doi:10.1086/166255.

[30] R I Kostik and T V Orlova. On the microturbulence in the solar photosphere. Solar Physics, 62(1):89–92, 1979. doi:10.1007/BF00150135.

[31] Rasmus Munk Larsen. Efficient algorithms for helioseismic inversion. PhD thesis, Ph. D. thesis, University of Aarhus, Denmark, 1998.

[32] M. López-Puertas and F.W. Taylor. Non-LTE Radiative Transfer in the Atmosphere. Series on atmospheric, oceanic and planetary physics. World Scientific, 2001. URL: https://books.google.com/books?id=1dC9l0q67SYC.

[33] D. J. McComas, E. R. Christian, C. M.S. Cohen, A. C. Cummings, A. J. Davis, M. I. Desai, J. Giacalone, M. E. Hill, C. J. Joyce, S. M. Krimigis, A. W. Labrador, R. A. Leske, O. Malandraki, W. H. Matthaeus, R. L. McNutt, R. A. Mewaldt, D. G. Mitchell, A. Posner, J. S. Rankin, E. C. Roelof, N. A. Schwadron, E. C. Stone, J. R. Szalay, M. E. Wiedenbeck, S. D. Bale, J. C. Kasper, A. W. Case, K. E. Korreck, R. J. MacDowall, M. Pulupa, M. L. Stevens, and A. P. Rouillard. Probing the energetic particle environment near the Sun. Nature, 576(7786):223–227, 2019. doi:10.1038/s41586-019-1811-1.

[34] Dimitri Mihalas. Stellar atmospheres. 1978. URL: https://ui.adsabs.harvard.edu/abs/1978stat.book.....M.

[35] I. Milić and M. van Noort. Line response functions in nonlocal thermodynamic equilibrium. Isotropic case. Astronomy & Astrophysics, 601:A100, May 2017. URL: https://ui.adsabs.harvard.edu/abs/2017A&A...601A.100M, doi:10.1051/0004-6361/201629980.

[36] Ivan Milić. NSO COLLAGE Course on Solar Spectral Line Diagnostics. 2021. URL: https://nso.edu/students/collage/collage-2021.

[37] E. A. Milne. Radiative equilibrium in the outer layers of a star. Monthly Notices of the Royal Astronomical Society, 81:361–375, March 1921. URL: https://ui.adsabs.harvard.edu/abs/1921MNRAS..81..361M, doi:10.1093/mnras/81.5.361.

[38] R. Mitalas and K. R. Sills. On the Photon Diffusion Time Scale for the Sun. The Astrophysical Journal, 401:759, December 1992. URL: https://ui.adsabs.harvard.edu/abs/1992ApJ...401..759M, doi:10.1086/172103.

[39] D. Müller, O. C. St. Cyr, I. Zouganelis, H. R. Gilbert, R. Marsden, T. Nieves-Chinchilla, E. Antonucci, F. Auchère, D. Berghmans, T. S. Horbury, R. A. Howard, S. Krucker, M. Maksimovic, C. J. Owen, P. Rochus, J. Rodriguez-Pacheco, M. Romoli, S. K. Solanki, R. Bruno, M. Carlsson, A. Fludra, L. Harra, D. M. Hassler, S. Livi, P. Louarn, H. Peter, U. Schühle, L. Teriaca, J. C. del Toro Iniesta, R. F. Wimmer-Schweingruber, E. Marsch, M. Velli, A. De Groof, A. Walsh, and D. Williams. The Solar Orbiter mission. Science overview. Astronomy & Astrophysics, 642:A1, October 2020. URL: https://ui.adsabs.harvard.edu/abs/2020A&A...642A...1M, arXiv:2009.00861, doi:10.1051/0004-6361/202038467.

[40] D. Orozco Suárez, L. R. Bellot Rubio, J. C. del Toro Iniesta, S. Tsuneta, B. W. Lites, K. Ichimoto, Y. Katsukawa, S. Nagata, T. Shimizu, R. A. Shine, Y. Suematsu, T. D. Tarbell, and A. M. Title. Quiet-Sun Internetwork Magnetic Fields from the Inversion of Hinode Measurements. The Astrophysical Journal Letters, 670(1):L61–L64, November 2007. arXiv:0710.1405, doi:10.1086/524139.

[41] Frédéric Paletou. On Milne-Barbier-Unsöld relationships. Open Astronomy, 27(1):76–79, April 2018. URL: https://ui.adsabs.harvard.edu/abs/2018OAst...27...76P, arXiv:1711.07026, doi:10.1515/astro-2018-0018.

[42] A. Pannekoek. Limb darkening. Monthly Notices of the Royal Astronomical Society, 95:733, June 1935. URL: https://ui.adsabs.harvard.edu/abs/1935MNRAS..95..733P, doi:10.1093/mnras/95.9.733.

[43] Clare E. Parnell and Ineke De Moortel. A contemporary view of coronal heating. Philosophical Transactions of the Royal Society A: Mathematical, Physical and Engineering Sciences, 370(1970):3217–3240, 2012. arXiv:1206.6097, doi:10.1098/rsta.2012.0113.

[44] Annamaneni Peraiah. An Introduction to Radiative Transfer. 2001. URL: https://ui.adsabs.harvard.edu/abs/2001irt..book.....P.

[45] W. Dean Pesnell, B. J. Thompson, and P. C. Chamberlin. The Solar Dynamics Observatory (SDO). Solar Physics, 275(1-2):3–15, January 2012. URL: https://ui.adsabs.harvard.edu/abs/2012SoPh..275....3P, doi:10.1007/s11207-011-9841-3.

[46] F. P. Pijpers and M. J. Thompson. Faster formulations of the optimally localized averages method for helioseismic inversions. Astronomy & Astrophysics, 262(2):L33–L36, September 1992. URL: https://ui.adsabs.harvard.edu/abs/1992A&A...262L..33P.

[47] F. P. Pijpers and M. J. Thompson. The SOLA method for helioseismic inversion. Astronomy & Astrophysics, 281(1):231–240, January 1994. URL: https://ui.adsabs.harvard.edu/abs/1994A&A...281..231P.

[48] William H. Press, Saul A. Teukolsky, William T. Vetterling, and Brian P. Flannery. Numerical Recipes 3rd Edition: The Art of Scientific Computing. Cambridge University Press, USA, 3 edition, 2007. URL: https://www.cambridge.org/us/academic/subjects/mathematics/numerical-recipes/numerical-recipes-art-scientific-computing-3rd-edition?format=HB&isbn=9780521880688.

[49] E.R. Priest. Solar physics: Overview, 07 2020. URL: https://oxfordre.com/physics/view/10.1093/acrefore/9780190871994.001.0001/acrefore-9780190871994-e-21, doi:10.1093/acrefore/9780190871994.013.21.

[50] Mark P. Rast, Nazaret Bello González, Luis Bellot Rubio, Wenda Cao, Gianna Cauzzi, Edward Deluca, Bart de Pontieu, Lyndsay Fletcher, Sarah E. Gibson, Philip G. Judge, Yukio Katsukawa, Maria D. Kazachenko, Elena Khomenko, Enrico Landi, Valentín Martínez Pillet, Gordon J. D. Petrie, Jiong Qiu, Laurel A. Rachmeler, Matthias Rempel, Wolfgang Schmidt, Eamon Scullion, Xudong Sun, Brian T. Welsch, Vincenzo Andretta, Patrick Antolin, Thomas R. Ayres, K. S. Balasubramaniam, Istvan Ballai, Thomas E. Berger, Stephen J. Bradshaw, Ryan J. Campbell, Mats Carlsson, Roberto Casini, Rebecca Centeno, Steven R. Cranmer, Serena Criscuoli, Craig Deforest, Yuanyong Deng, Robertus Erdélyi, Viktor Fedun, Catherine E. Fischer, Sergio J. González Manrique, Michael Hahn, Louise Harra, Vasco M. J. Henriques, Neal E. Hurlburt, Sarah Jaeggli, Shahin Jafarzadeh, Rekha Jain, Stuart M. Jefferies, Peter H. Keys, Adam F. Kowalski, Christoph Kuckein, Jeffrey R. Kuhn, David Kuridze, Jiajia Liu, Wei Liu, Dana Longcope, Mihalis Mathioudakis, R. T. James McAteer, Scott W. McIntosh, David E. McKenzie, Mari Paz Miralles, Richard J. Morton, Karin Muglach, Chris J. Nelson, Navdeep K. Panesar, Susanna Parenti, Clare E. Parnell, Bala Poduval, Kevin P. Reardon, Jeffrey W. Reep, Thomas A. Schad, Donald Schmit, Rahul Sharma, Hector Socas-Navarro, Abhishek K. Srivastava, Alphonse C. Sterling, Yoshinori Suematsu, Lucas A. Tarr, Sanjiv Tiwari, Alexandra Tritschler, Gary Verth, Angelos Vourlidas, Haimin Wang, Yi-Ming Wang, NSO and DKIST Project, DKIST Instrument Scientists, DKIST Science Working Group, and DKIST Critical Science Plan Community. Critical Science Plan for the Daniel K. Inouye Solar Telescope (DKIST). Solar Physics, 296(4):70, April 2021. URL: https://ui.adsabs.harvard.edu/abs/2021SoPh..296...70R, arXiv:2008.08203, doi:10.1007/s11207-021-01789-2.

[51] M. Rempel. Numerical simulations of quiet sun magnetism: On the contribution from small-scale dynamo. The Astrophysical Journal, 789(2):132, jun 2014. doi:10.1088/0004-637x/789/2/132.

[52] M. Rempel. EXTENSION OF THE MURAM RADIATIVE MHD CODE FOR CORONAL SIMULATIONS. The Astrophysical Journal, 834(1):10, dec 2016. doi:10.3847/1538-4357/834/1/10.

[53] Thomas R Rimmele, Mark Warner, Stephen L Keil, Philip R Goode, Michael Knölker, Jeffrey R Kuhn, Robert R Rosner, Joseph P McMullin, Roberto Casini, Haosheng Lin, Friedrich Wöger, Oskar von der Lühe, Alexandra Tritschler, Alisdair Davey, Alfred de Wijn, David F Elmore, André Fehlmann, David M Harrington, Sarah A Jaeggli, Mark P Rast, Thomas A Schad, Wolfgang Schmidt, Mihalis Mathioudakis, Donald L Mickey, Tetsu Anan, Christian Beck, Heather K Marshall, Paul F Jeffers, Jacobus M Oschmann, Andrew Beard, David C Berst, Bruce A Cowan, Simon C Craig, Eric Cross, Bryan K Cummings, Colleen Donnelly, Jean-Benoit de Vanssay, Arthur D Eigenbrot, Andrew Ferayorni, Christopher Foster,

Chriselle Ann Galapon, Christopher Gedrites, Kerry Gonzales, Bret D Goodrich, Brian S Gregory, Stephanie S Guzman, Stephen Guzzo, Steve Hegwer, Robert P Hubbard, John R Hubbard, Erik M Johansson, Luke C Johnson, Chen Liang, Mary Liang, Isaac McQuillen, Christopher Mayer, Karl Newman, Brialyn Onodera, LeEllen Phelps, Myles M Puentes, Christopher Richards, Lukas M Rimmele, Predrag Sekulic, Stephan R Shimko, Brett E Simison, Brett Smith, Erik Starman, Stacey R Sueoka, Richard T Summers, Aimee Szabo, Louis Szabo, Stephen B Wampler, Timothy R Williams, and Charles White. The Daniel K. Inouye Solar Telescope – Observatory Overview. Solar Physics, 295(12):172, 2020. doi:10.1007/s11207-020-01736-7.

[54] B. Ruiz Cobo and J. C. del Toro Iniesta. Inversion of Stokes Profiles. The Astrophysical Journal, 398:375, October 1992. URL: https://ui.adsabs.harvard.edu/abs/1992ApJ...398..375R, doi:10.1086/171862.

[55] B. Ruiz Cobo and J. C. del Toro Iniesta. On the sensitivity of Stokes profiles to physical quantities. Astronomy & Astrophysics, 283:129–143, March 1994. URL: https://ui.adsabs.harvard.edu/abs/1994A&A...283..129R.

[56] Robert J. Rutten. Radiative Transfer in Stellar Atmospheres. 2003. URL: https://ui.adsabs.harvard.edu/abs/2003rtsa.book.....R.

[57] George B. Rybicki. Properties of statistical equilibrium equations: Positivity and uniqueness. The Astrophysical Journal, 479(1):357–362, apr 1997. doi:10.1086/303877.

[58] K. Schwarzschild. On the equilibrium of the Sun's atmosphere. Nachrichten von der Königlichen Gesellschaft der Wissenschaften zu Göttingen. Math.-phys. Klasse, 195:41–53, January 1906. URL: https://ui.adsabs.harvard.edu/abs/1906WisGo.195...41S.

[59] V. A. Sheminova. Turbulence and Rotation in Solar-Type Stars. Kinematics and Physics of Celestial Bodies, 35(3):129–142, May 2019. URL: https://ui.adsabs.harvard.edu/abs/2019KPCB...35..129S, arXiv:1907.12241, doi:10.3103/S088459131903005X.

[60] Otto Struve and C. T. Elvey. The Intensities of Stellar Absorption Lines. The Astrophysical Journal, 79:409, May 1934. URL: https://ui.adsabs.harvard.edu/abs/1934ApJ....79..409S, doi:10.1086/143551.

[61] J. M. Varah. On the numerical solution of ill-conditioned linear systems with applications to ill-posed problems. SIAM Journal on Numerical Analysis, 10(2):257–267, 1973. arXiv:https://doi.org/10.1137/0710025, doi:10.1137/0710025.

[62] J. M. Varah. A practical examination of some numerical methods for linear discrete ill-posed problems. SIAM Review, 21(1):100–111, 1979. arXiv:https://doi.org/10.1137/1021007, doi:10.1137/1021007.

[63] A. Vögler, S. Shelyag, M. Schüssler, F. Cattaneo, T. Emonet, and T. Linde. Simulations of magneto-convection in the solar photosphere. Equations, methods, and results of the MURaM code. Astronomy & Astrophysics, 429:335–351, January 2005. URL: https://ui.adsabs.harvard.edu/abs/2005A&A...429..335V, doi:10.1051/0004-6361:20041507.

[64] O. R. White. A General Solution of the Statistical Equilibrium Equations. The Astrophysical Journal, 134:85, July 1961. URL: https://ui.adsabs.harvard.edu/abs/1961ApJ...134...85W, doi:10.1086/147130.

[65] Hongyuan Zha and Per Christian Hansen. Regularization and the general gauss-markov linear model. Mathematics of Computation, 55(192):613–624, 1990. URL: http://www.jstor.org/stable/2008436.

Appendix A

Brief Introduction to the Theory of Radiative Transfer

In this chapter we discuss the theory of radiative transfer (transport theory) that describes light-matter interactions as radiation propagates through a medium. Our goal here is to discuss how spectral lines form in the solar photosphere and how the spectral line shape depends on the atmospheric properties. It is these that later allow us to infer for these atmosphere parameters from an observed spectra. Please note that the derivations follow from the work by Mihalas [34], Peraiah [44], Puertas [32] and Rutten [56], and COLLAGE course by Ivan Milić [36].

A.1 Radiative transfer equation

In transport theory, the fundamental quantity that describes the radiation field is the monochromatic specific intensity I_λ. Specific intensity at point p in an arbitrary direction $\hat{s}$ is defined as the amount of energy dE_λ transported by the radiation field through an infinitesimal area dA $(\hat{n})$, in directions confined to the solid angle $d\omega$, over time dt, in the wavelength interval $(\lambda, \lambda + d\lambda)$ (see Figure A.1). Mathematically, it is given by

$$I_\lambda(\vec{r}, \hat{n}, t) = \frac{dE_\lambda}{d\lambda \; d\omega \; dt \; dA \; (\hat{n} \cdot \hat{s})} \quad [\text{W m}^{-3} \text{ sr}^{-1}] \tag{A.1}$$

Transport theory states that as a beam of light travels through a thin slab of thickness dz, absorption, emission and scattering processes within the medium may add or remove photons from this beam (see Figure A.2). In a nutshell it means to keep track of photons as radiation travels through a medium. The relation between the change in intensity dI_λ (at wavelength λ) to the underlying

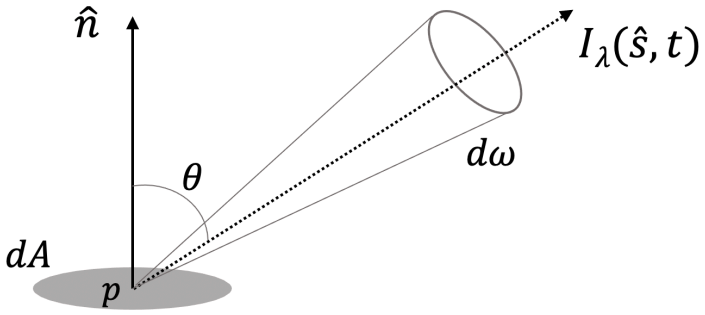

Figure A.1: Monochromatic specific intensity I_λ at point p in an arbitrary direction $\hat{s}$, passing through an infinitesimal area dA (directed along $\hat{n}$), into the solid angle $d\omega$, at time t.

interaction processes is given by the radiative transfer equation (RTE):

$$\frac{dI_\lambda}{dz} = -\chi_\lambda \, I_\lambda + j_\lambda \tag{A.2}$$

In Equation A.2, we assume that the quantities/processes are time invariant. This assumption is followed throughout this work. In the next section, we describe individual terms in the RTE.

A.1.1 Absorption and emission processes in RTE

In Equation A.2, $-\chi_\lambda I_\lambda$ corresponds to the intensity attenuation per unit path length due to absorption/scattering processes. Here, χ_λ ($[\mathrm{m}^{-1}]$) is the monochromatic opacity (total absorption/attenuation/extinction coefficient) and is a measure of degree of opaqueness of the medium. It is defined as the fractional change in intensity per unit path length (along the ray path) and corresponds to all processes that removes/destroys photons from the radiation beam. Mathematically, it is given by the product of the number density of absorbers ($[\mathrm{m}^{-3}]$) and their absorption cross-section ($[\mathrm{m}^2]$), where absorption cross-section is a measure of the probability of photon absorption by an absorber. Thus, a photon has a higher chance of getting absorbed (or scattered) if the number density of absorbers is large and/or if individual absorbers have a larger cross-section.

Opacity can also be understood in terms of the photon mean free path ($1/\chi_\lambda$), which cor-

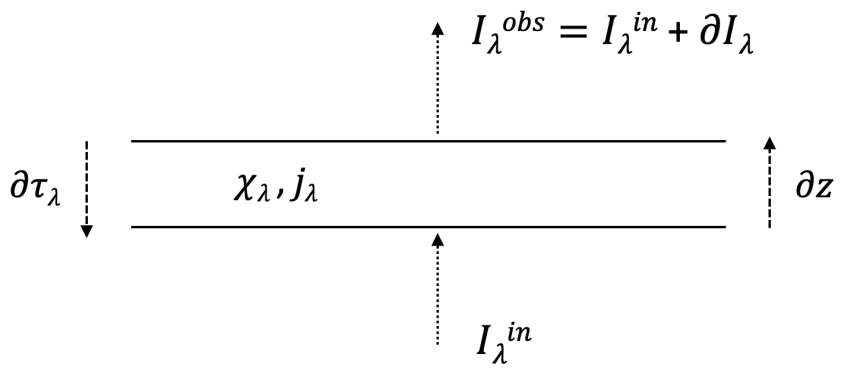

Figure A.2: Intensity passing through a thin atmospheric slab of width ∂z (optical depth $\partial\tau_\lambda$). $I_\lambda^{\rm in}$ is the incident radiation on the lower slab boundary, while $\mathrm{I}_\lambda^{\rm obs}$ is the emergent (or observed) intensity. χ_λ and j_λ are the opacity and emissivity of the medium. ∂I_λ corresponds to the change in intensity due to absorption and emission (and scattering) processes as radiation passes through the slab.

responds to the average distance a photon travels before it gets absorbed (or scattered). A larger opacity thus implies a shorter mean free path, which means that the photon would travel a shorter distance before it would be absorbed by the medium.

Opacity has contribution from both absorption and scattering processes. In 'true' absorption, a photon is destroyed completely and its energy (completely or partially) is converted into the thermal energy of the gas. On the other hand, in scattering processes, a photon is not destroyed but its interaction with a 'scatterer' results in it being re-emitted in a new direction with approximately the same wavelength (and energy). To understand this distinction, let's consider a case where an atom (or ion) absorbs a photon and moves into a higher energy electronic state. Subsequently, a collisional de-excitation of the atom would mean that the energy of the photon went into increasing the thermal energy of the gas pool and the entire process would be termed 'true' absorption. Instead, it would be a scattering event if the atom radiatively de-excites and returns to the original atomic state. In this case, the photon would be emitted in a 'new' direction with approximately the same energy.

In Equation A.2, j_λ ([W m^{-4} sr^{-1}]) is the monochromatic emission coefficient or emissivity

and is a sum of all emission/scattering processes that adds photons at wavelength λ to the radiation beam. It can be understood as opposite of absorption. Unlike the attenuation term -$\chi_\lambda I_\lambda$, emissivity is independent of the incident intensity.

A.2 Standard form of RTE

Standard form of RTE is expressed in terms of optical depth scale τ_λ and source function S_λ, and is obtained by dividing both sides of Equation A.2 by $-\chi_\lambda$:

$$\frac{dI_\lambda}{d\tau_\lambda} = I_\lambda - S_\lambda \tag{A.3}$$

Here, source function S_λ is defined as the ratio of total emissivity to total opacity j_λ/χ_λ and the optical depth difference is defined as $d\tau_\lambda = -\chi_\lambda \, dz$. Here, negative sign is a consequence of the sign convention where dz is taken to be positive along the ray path (towards the observer), while $d\tau_\lambda$ increases opposite to the ray path, away from the observer (see Figure A.2).

Optical depth scale τ_λ is a dimensionless quantity and is a measure of how opaque the medium is along the line-of-sight. For a finite thickness atmospheric slab, the optical depth $\tau_\lambda{}'$ at depth z corresponds to the integrated opacity along the line-of-sight i.e. $\tau'_\lambda = \int_0^{\tau'_\lambda} d\tau_\lambda = \int_{z_{max}}^{z} -\chi_\lambda(z) \, dz$ (see Figure A.3). Optical depth can also be understood in terms of the number of photon mean free paths along the line-of-sight and thus is a measure of how 'deep' an outside observer located at $\tau_\lambda = 0$ can see into the medium.

Compared to geometrical length scale z, optical depth scale τ_λ is a natural length scale for radiation as it carries information about both the geometrical scale and the optical properties of the medium e.g. absorption, scattering etc. In Figure A.3, as light travels through the slab it is hard to make claims about the geometrical thickness of the slab simply based on the incident (I_λ^{in}) and emergent/observed ($\text{I}_\lambda^{\text{obs}}$) intensities i.e. for a given I_λ^{in}, a wide slab (large $\Delta z = z_{max} - z$) with optically tenuous material (small χ_λ), and a thin slab (small Δz) with optically dense material (large χ_λ) can result in the same emergent intensity. In other words, as light travels through a medium, its interaction depends on both the geometrical path length and the opacity along that

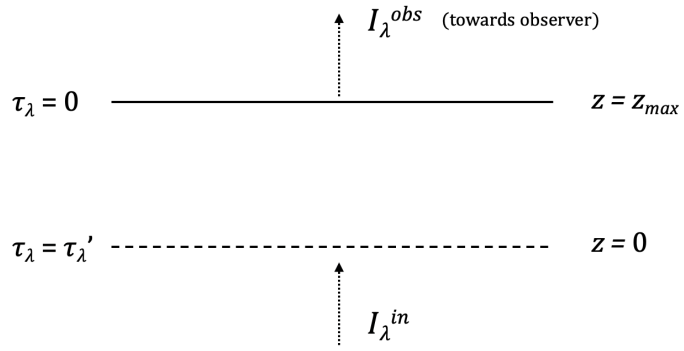

Figure A.3: Radiation through a finite thickness atmospheric slab. Similar to Figure A.2, $I_\lambda^{\rm in}$ is the incident radiation on the lower boundary located at $z = 0$ ($\tau_\lambda = \tau'_\lambda$). $z = z_{max}$ ($\tau_\lambda = 0$) corresponds to the upper boundary of the slab and marks the location where emergent radiation $\mathrm{I}_\lambda^{\rm obs}$ escapes out (and also the location of the 'observer'). By convention, $\tau_\lambda = 0$ corresponds to the 'observer' location.

path. Optical depth scale combines these two and thus is a natural length scale for radiation.

A.2.1 Formal solution of RTE

Using the RTE (Equation A.3), our goal is to solve for the emergent intensity through a medium, given that the incident intensity and the properties of the medium are known i.e. opacity and source function. The emergent intensity $\mathrm{I}_\lambda^{\rm obs}$ coming out of a finite atmospheric slab in Figure A.3 is given by

$$I_\lambda^{\rm obs} = I_\lambda^{\rm in}\ e^{-\tau'_\lambda} + \int_0^{\tau'_\lambda} S_\lambda(\tau_\lambda)\ e^{-\tau_\lambda}\ d\tau_\lambda \tag{A.4}$$

Equation A.4 corresponds to the integral form of RTE and is also called the formal solution. The solution states that the emergent intensity is a sum of contribution from the incident intensity $I_\lambda^{\rm in}$ attenuated by the absorbing material ($e^{-\tau'_\lambda}$), and the source function (emission) from all volume elements located at depths τ_λ, which also gets attenuated by the absorbing material in between the observer ($\tau_\lambda = 0$) and the location of the emitting element. Thus, source function from the material closer to the observer contributes more to the $\mathrm{I}_\lambda^{\rm obs}$ as compared to material further away.

For a simple test case when the source function is constant and is invariant with optical depth, the emergent intensity is given by

$$I_\lambda^{\rm obs} = I_\lambda^{\rm in}\ e^{-\tau'_\lambda} + S_\lambda(1 - e^{-\tau'_\lambda}) \tag{A.5}$$

In the limit $\tau'_\lambda \rightarrow\ 0$, $e^{-\tau'_\lambda} \rightarrow 1$ and $I_\lambda^{\rm obs} \rightarrow\ I_\lambda^{\rm in}$. This states that if there are no sources/sinks along the ray path, then the intensity stays constant.

In the limit $\tau'_\lambda \rightarrow \infty$, $e^{-\tau'_\lambda} \rightarrow 0$, and $I_\lambda^{\rm obs} \approx S_\lambda$. This means that when looking at an optically thick medium the information about the incident radiation is lost and the emergent intensity effectively corresponds to the source function of the medium.

So far we discussed radiative transfer through a finite width atmospheric slab. In the next section we extend the discussion to boundary condition that is more applicable to the case of solar/stellar atmospheres.

A.2.2 Radiative transfer through solar/stellar atmosphere

In this section, we discuss radiative transfer through a simplified solar (or stellar) atmosphere where the boundary conditions are similar to that shown in Figure A.4. Here, the atmosphere is semi-infinite in the sense that the boundary exists only on one side ($\tau_\lambda = 0,\ z = z_{max}$) where radiation escapes out, while on the other side, it extends deep into the sun where $\tau_\lambda\ = \tau'_\lambda\ \rightarrow \infty$. Thus, the incident radiation $I_\lambda^{\rm in}$ here is immaterial as given the boundary condition its contribution to the emergent intensity $I_\lambda^{\rm in} e^{-\tau'_\lambda} \rightarrow 0$. The emergent intensity $\mathrm{I}_\lambda^{\rm obs}$ then only depends on the source function and its variation with optical depth, and is given by

$$I_\lambda^{\rm obs} = \int_0^\infty S_\lambda(\tau_\lambda)\ e^{-\tau_\lambda}\ d\tau_\lambda \tag{A.6}$$

When representing solar atmosphere in Figure A.4, we assumed a *plane-parallel* geometry. Here, properties of the atmospheres and thus optical depth and source function are assumed to vary only along the radial direction (local z-direction), and are constant along the transverse direction (local x and y directions). The validity of this assumption lies in the fact that the width of the

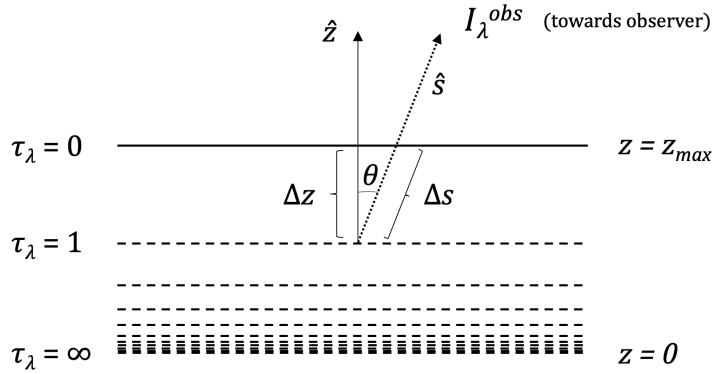

Figure A.4: A simplified *plane-parallel* atmosphere where medium properties vary along the z-direction only and are invariant along the horizontal directions. The observer is located at $\tau_\lambda = 0$ (upper boundary of the atmosphere) and $\hat{s}$ marks the line-of-sight direction towards the observer. Optical depth increases as we go deeper into that atmosphere (away from the observer). Assuming Milne-Eddington atmosphere, $\tau_\lambda = 1$ marks the deepest we can see at this wavelength and the $\mathrm{I}_\lambda^{\mathrm{obs}}$ effectively corresponds to the source function at this depth location.

photosphere ($\approx$ 500 km) is much small in comparison to the radius of curvature of the sun ($\approx$ 700 Mm). Thus, if we zoom into a small patch containing the photosphere, the geometry will be essentially flat or *plane-parallel*.

In Figure A.4, we show a more generalized case of radiative transfer where the line-of-sight radiation is directed along a general direction $\hat{s}$, at an angle θ with respect to the z-direction. In this case, a correction factor $\mu = cos\ \theta$ enters the RTE that relates the 'true' optical path ds along the ray to the vertical path dz by $ds = dz/\mu$. The emergent intensity for this generalized case is then given by

$$I_\lambda^{\mathrm{obs}}(\mu) = \int_0^\infty \frac{S_\lambda(\tau_\lambda, \mu)}{\mu}\ e^{\frac{-\tau_\lambda}{\mu}}\ d\tau_\lambda \tag{A.7}$$

In the next section, we solve for the emergent intensity for a test case where source function varies linearly with optical depth.

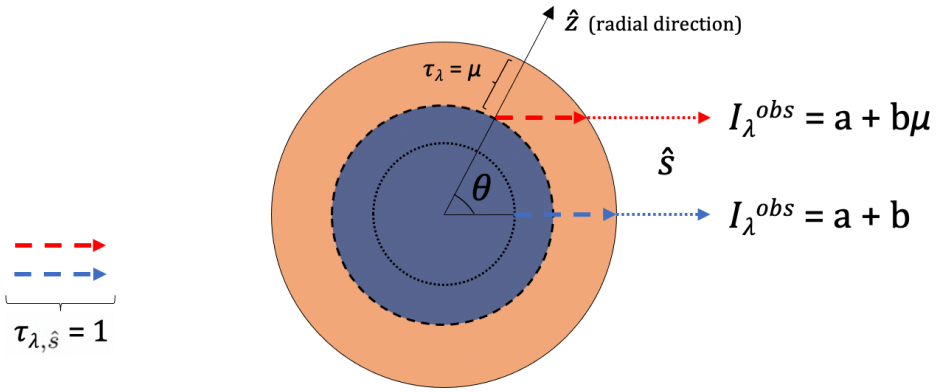

Figure A.5: Here we show a 2-D cross-sectional top-view of the sun, where blue region corresponds to the deeper layers and orange region corresponds to the upper layers of the sun. Blue and red rays, directed towards the observer along $\hat{s}$ direction, correspond to radiation from the disc-center and closer to the limb, respectively. For a Milne-Eddington atmosphere, we effectively get radiation from depth where the 'true' optical depth/path length $\tau_{\lambda,\hat{s}} = 1$ or where radial optical depth $\tau_\lambda = \mu = cos\ \theta$. For radiation from the disc-center this corresponds to deeper layers of the atmosphere ($\mu \approx 1$) where source function is larger. For radiation from the limb, $\tau_{\lambda,\hat{s}} = 1$ occurs at upper layers of the atmosphere where source function is smaller. This results in the disc-center to 'appear' brighter as compared to the limb, resulting in the *limb-darkening* effect.

A.2.3 Emergent intensity through a Milne-Eddington atmosphere

Milne-Eddington atmosphere is a simplified atmospheric model where source function varies linearly with optical depth i.e. $S_\lambda = a + b\tau_\lambda$, where a and b are constants. The emergent intensity for this model is given by

$$I_\lambda^{\text{obs}}(\mu) = a + b\mu \tag{A.8}$$

This solution is called the Eddington-Barbier relationship ([41, 56]) and states that when source function varies linearly with optical depth, the emergent intensity effectively corresponds to source function at $\tau_\lambda = \mu$. This means that closer to the disk center where $\mu \approx 1$ we are looking at the deepest layers observable at wavelength λ. On the other hand, as we go closer to the limb

the emergent intensity corresponds to source function at shallower layers as μ gets smaller ($\mu < 1$). Given that source function decreases as we go higher up in the solar photosphere i.e. smaller τ_λ, this angular dependence of the emergent intensity results in an phenomena where limb 'appears' darker as compared to the disc-center. This is called the *limb-darkening* effect (see Figure A.5) ([42, 56]).

The physical reason behind *limb-darkening* has to do with the difference between the optical path length $\tau_\lambda = \mu$ along the radial (local z) direction, and the 'actual' optical path length $\tau_{\lambda,\hat{s}}$ along the line-of-sight. These are related to each other by $\tau_\lambda = \mu \times \tau_{\lambda,\hat{s}}$. According to Eddington-Barbier relation mentioned above, the emergent intensity corresponds to source function from the atmospheric layer where $\tau_\lambda = \mu$. This means that the observed intensity 'effectively' corresponds to source function at the depth where the actual optical path length $\tau_{\lambda,\hat{s}} = 1$. For a slanted beam with respect to the local radial direction, $\tau_{\lambda,\hat{s}} = 1$ occurs at upper layers of the atmosphere, while for radiation from the disc-center, the two optical path lengths are equal $\tau_\lambda = \tau_{\lambda,\hat{s}} = 1$ and we are looking at the deepest layers possible at wavelength λ (see Figure A.5).

It is evident that in order to solve for the emergent intensity in Equation A.7, we would need to know the source function and its variation with optical depth. Given that source function depends on opacity and emissivity, we discuss the physical processes that contributes to these quantities in the next section.

A.3 Opacity and Emissivity

A.3.1 Physical processes that contribute to opacity and emissivity

As mentioned previously, opacity χ_λ and emissivity j_λ characterize the interaction between radiation and matter. Total opacity is a sum of contribution from all the absorption (and scattering) processes that remove photons from a radiation beam, while total emissivity is a sum of contribution from all the emission (and scattering) processes that add photons to the beam path. Following is a list of physical processes that contribute to opacity (not exhaustive):

- Bound-bound absorption (photo-excitation; $\chi_{\lambda,\mathrm{bb}}$) - In this process, a photon with energy equal to the energy level difference of the atomic states involved, is absorbed by an atom (or ion). Subsequently, if the atom collisionally de-excites then it would mean that the original photon energy went into increasing the kinetic energy of the colliding particles, therefore increasing the thermal energy of the gas pool. Instead, if the atom radiatively de-excites to the original state then the process would be termed scattering.

  Opacity and emissivity (at wavelength λ), corresponding to bound-bound line transitions between two atomic states (upper u and lower l) due to radiative excitation and spontaneous/stimulated de-excitation, are given by:

$$\chi_\lambda = \frac{hc}{4\pi\lambda}(n_l B_{lu} - n_u B_{ul})\phi_\lambda \tag{A.9}$$

$$j_\lambda = \frac{hc}{4\pi\lambda} n_u A_{ul} \phi_\lambda \tag{A.10}$$

  where, h is the Planck constant, c is the speed of light, n_l and n_u are the level populations in the lower and upper atomic states, A_{ul}, B_{ul} and B_{lu} are Einstein coefficients (probabilistic measure of absorption/emission by an atom), and ϕ_λ is the absorption line profile (see Section A.3.2 for details).

- Bound-free absorption (photo-ionization; $\chi_{\lambda,\mathrm{bf}}$) - In this process, an atom gets ionized by absorbing a photon with energy greater than the ionization potential, and the excess photon energy goes into the kinetic energy of the escaped electron.

- Free-free absorption ($\chi_{\lambda,\mathrm{ff}}$) - In this process, a free electron in the vicinity of an ion 'collides' with a photon and moves into a higher energy continuum state. The process is called free-free absorption because the electron is not bound to any atom/ion before or after absorbing the photon.

- Electron (Thompson) scattering - In this process, a free 'isolated' electron interacts with the electric field of an incident electromagnetic waves (photon) and oscillates. This accelerated electron then re-emits the photon (with approximately the same wavelength) in a 'new'

direction resulting in scattering of the the original photon. Note, in case the 'scatterer' is an atom (or molecule) the process would be Rayleigh scattering.

For each of the above mentioned processes that contributes to opacity, there is an equivalent reverse process that contributes to emissivity e.g. the opposite of photo-ionization is the radiative recombination process where a free electron is captured by an ion emitting photon in the process. So far we discussed physical quantities such as opacity, emissivity etc. in context of single monochromatic wavelength λ. In the next section we extend this discussion and talk about the wavelength dependence of these quantities and ultimately the formation of spectral lines.

A.3.2 Wavelength dependence of opacity and emissivity

In the last section, we briefly discussed the physical processes that contribute to opacity (and emissivity) at a given wavelength. Given that opacity varies with wavelength, these contributions can be further sub-categorized into line and continuum opacities. This categorization is based on how quickly the opacity varies with wavelength. Continuum opacities ($\chi_{\lambda,\mathrm{bf}}$, $\chi_{\lambda,\mathrm{ff}}$, etc), and thus the magnitude of continuum intensity, vary very slowly with wavelength. On the other hand, line opacity, which has contribution from the bound-bound transitions only ($\chi_{\lambda,\mathrm{bb}}$), may vary drastically over a short wavelength span. This steep opacity variation with wavelength, close to the line-center λ_0, is one of the reasons for the existence of spectral lines in the solar photosphere, where dark (less intense) absorption lines are superimposed on top of the bright continuum spectra.

Line opacity is a result of the transition between two bound energy levels within an atom (or ion). Thus, only those photons should be absorbed (or emitted) that have wavelength λ_0 corresponding to the energy difference between the atomic levels involved. The resulting emergent spectral line should thus have a $\delta-$function shape. In reality, spectral lines are not infinitely sharp and are 'broadened'. This is due to processes both internal and external to the atom that allow atoms to absorb and emit over a range of wavelengths near the line center i.e. opacity (and emissivity) is non-zero over a range of wavelengths around λ_0. The normalized absorption

line profile function ϕ_λ describes this variation of opacity (and emissivity) with wavelength and represents the probability of absorption of photons close to the line center. In other words, it describes the distribution of absorption (and emission) around the line center. ϕ_λ is usually largest close to the line center (assuming stationary atmosphere i.e. line-of-sight velocity is 0) and gets smaller further away. This means that for a line process, photons with wavelength close to the line center have the highest chances of getting absorbed (or emitted).

Following is a list of processes that contribute to the ϕ_λ (not exhaustive):

- Natural broadening (Lorentzian-shaped ϕ_λ) - This process is a consequence of the Heisenberg uncertainty principle which states that the finite lifetime of a given atomic state (Δt_{life}) results in an uncertainty in energy ΔE associated with it i.e. $\Delta E \times \Delta t_{life} \approx \hbar$. This means that energy levels with smaller lifetimes have larger ΔE uncertainties, and vice-versa. This uncertainty in energy levels results in a spread in wavelengths and allows for absorption/emissions of photons over a range of wavelengths. Given that this uncertainty is independent of factors external to the atom, it determines the 'natural broadening' of the transition involved. This broadening is Lorentzian in shape.

- Doppler broadening (Gaussian-shaped ϕ_λ) - This is a consequence of the fact that absorbers (or emitters) are moving with respect to the observer, resulting in the apparent shift in wavelengths of the 'observed' photons. The component of the line-of-sight velocity of the atoms follows a Maxwell-Boltzmann distribution and thus the associated line profile ϕ_λ has Gaussian shape. Further, the velocity distribution and the width of doppler broadening depends on the temperature (kinetic) of the medium.

- Pressure or collisional broadening (Lorentzian-shaped ϕ_λ) - This broadening mechanism comes into play when atoms are packed very close to each other i.e. when the number density of the medium is large, resulting in quantum effects to distort (broaden) the energy levels, resulting in the broadening of spectral line.

- Zeeman splitting - In the presence of magnetic fields, energy levels may split and 'broaden'

spectral lines.

- Turbulence broadening - Broadening due to micro-turbulence (V_{mic}) and macro-turbulence (V_{mac}) velocities. V_{mic} ([7, 22, 23, 30, 59, 60]), which is included with the doppler/thermal width of the line profile, is due to small-scale non-thermal (turbulent) motions of the gas. V_{mac} ([7, 23, 59]), on the other hand, is a result of the fact that observations have finite spatial (horizontal) resolution and thus the observed spectra corresponds to radiation from the underlying unresolved 'macro' cells.

In addition to the above process, gradients in the line-of-sight velocity can also add to the broadening of the line and may result in line asymmetry.

Please note that when multiple broadening mechanisms are active, the net line profile shape is given by the convolution between all of the underlying processes e.g. in the presence of natural and doppler broadenings, the line profile is given by the Voigt function, a convolution between Lorentzian and Gaussian functions. In Voigt line profile, closer to line center, doppler broadening mechanism dominate and the line profile is similar to a Gaussian profile. Given that a Gaussian function falls off faster with wavelength, as compared to a Lorentzian function, away from the line center, the line profile is dominated by natural broadening mechanism. These broadening mechanisms (apart from Natural broadening) depend on the physical properties of the medium.

A.3.3 Formation of spectral lines

The variation of opacity with wavelength and source function with optical depth are the reason for the existence of spectral lines in the solar atmosphere. The emergent intensity I_λ^{obs} is effectively given by the source function at $\tau_\lambda = 1$ for that wavelength (assuming Milne-Eddington atmosphere). Given that wavelengths closer to the line-center have larger opacity and thus are more opaque, as compared to the line wings, the corresponding $\tau_\lambda = 1$ for these wavelengths occurs higher up in the atmosphere, where the source function is smaller. This results in intensity in the line-core to be smaller compared to the line wings, resulting in typical shape of the absorption line

in solar atmosphere. This differential sensitivity of different wavelengths within a spectral line later allows us to do depth dependent inversion of the physical properties of the medium (see Chapter 2 for more details).

It is important to emphasize that the shape of a spectral line is not equal to that of the line profile function ϕ_λ. Line profile shape depends on the 'local' properties of the medium, and thus vary with depth, while spectral lines are a net result of this depth dependent variation of the line profiles (and source functions). Only in the case of an optically thin atmosphere i.e. $\tau_\lambda << 1$ for all wavelengths and assuming a constant source function, the spectral line shape approximates the line profile function.

A.4 Synthesizing spectra through a model atmosphere

A.4.1 How to compute opacity and emissivity

As discussed in section A.3.1, line opacities are a result of bound-bound transition between two energy levels within an atom (and processes that broaden the line). In order to compute the opacity, we would require the level populations corresponding to the energy levels involved (see Equation A.9). Level populations are determined by the microscopic processes that populate or de-populate atomic energy levels e.g. spontaneous absorption and emission, induced emission, thermal (collisional) processes, radiative processes, etc. Thus, in order to compute level populations we would need to solve the statistical equilibrium equation that couples different atomic states ([34, 57, 64]). This equation states that the net rate of change of the number of atoms in a given energy level is given by difference in the rate at which atoms get added to that level and the rate at which they get removed from that level. Statistical equilibrium equation for energy level i is given by

$$\frac{dn_i}{dt} = \sum_{i \neq j} n_j P_{ji} - n_i \sum_{i \neq j} P_{ij} \tag{A.11}$$

Where n_i and n_j corresponds to level population in energy levels i and j, while P_{ij} and P_{ji} correspond to different processes that dictate the transition rates from level $i \rightarrow j$ and $j \rightarrow i$,

respectively. In the case of solar/stellar atmospheres, one usually assumes time invariance i.e. the net change in level population $\frac{dn_i}{dt}$ is 0. Under this assumption, the statistical equilibrium equation simplifies to

$$\sum_{i \neq j} n_j P_{ji} = n_i \sum_{i \neq j} P_{ij} \tag{A.12}$$

The processes that dictate level populations generally involve both collisional and radiative processes i.e. level populations depends on the thermodynamic state of the gas and the radiation field. This dependence of level population on radiation field makes the problem non-local in nature (Non-LTE) as radiation field depends on the properties of the medium at other locations and directions. Any changes to remote level population will change the corresponding opacity and source function and the resulting radiation field, which in turn can change the local level populations. Thus, the statistical equilibrium equation (that gives the population distribution among energy levels of the medium) and RTE (that describes how radiation is absorbed/emitted/transported through the medium) are coupled to each other. One usually has to iteratively solve the coupled RTE and statistical equilibrium equations until an equilibrium solution is achieved between the level populations and the radiation field. In general, this is computationally expensive as one needs to account for 'every' direction at 'every' depth in order to compute an exact solution. In the next section we discuss the LTE assumption which greatly simplifies this system.

A.4.2 Local thermodynamic equilibrium (LTE) approximation

Local Thermodynamic Equilibrium (LTE) ([34, 37, 58]) assumptions are usually employed to simplify the coupled system of equations mentioned in last section. Here, one assumes that in a small volume of the atmosphere, level populations are dominantly determined by the collisional processes only, which depend on the local properties of the medium e.g. local temperature and density. This decouples the statistical equilibrium equation from the RTE. Note that radiative excitation/de-excitation do occur in LTE, but collisions are frequent enough to transfer the net absorbed/emitted photon into the thermal energy of the gas pool. In other words, only matter

affects the radiation. Thus, the validity of the LTE approximation requires the pressure of the medium to be large enough so that the collisions are frequent and is assumed to be valid in the solar photosphere, the atmospheric region of interest in this thesis.

Another way to determine the validity of the LTE approximation is by comparing the photon mean free path and the typical distance over which atmospheric parameter (e.g. temperature) changes. A relatively small mean free path length implies that the photon does not travel far enough before getting absorbed and on average 'sees' the same (local) temperature plasma. This ensures that there is less photon scattering and the local plasma properties are not dictated by the remote properties of the medium.

LTE approximation greatly simplifies the calculation of the level populations for relevant energy levels and thus the opacity. Under this assumption, relative number of atoms/ions in different excitation and ionization states is given by Saha-Boltzmann statistics [34], which depend only on the local temperature. In addition, pressure (or number density etc.) is needed to close the system i.e. to compute the actual number of atoms in these levels. Opacity further depends on the absorption line profile function ϕ_λ (see Equation A.9) which is dictated by the local properties of the medium e.g. doppler broadening depends on the local temperature, pressure broadening depends on the local gas pressure (or total number density) etc. Note that an 'absorption' line profile ϕ_λ is different from the 'emergent' line profile, which corresponds to the observed spectra.

The source function, under LTE assumption, which dictates the local rate of energy generation depends only on the local temperature and is given by the Planck function (*Kirchoff-Planck* law) i.e. we assume that the medium locally radiates like a black body. Note that the energy distribution of the local radiation field may not be Planckian.

A.4.3 Synthesizing spectra under LTE approximation

In this section we discuss the basic step that goes into synthesizing an emergent spectra through a one-dimensional atmospheric model under the LTE approximation. The model has atmospheric parameters specified at each depth location (spatial grid). Under the assumption that

Table A.1: List of spectral lines used in this thesis

λ_0 [Å]	Blends (if any)	Spectral resolution $\Delta\lambda$ [mÅ]
Fe II (6147.743)	Fe I (6147.835)	17.5
Fe II (6149.241)	-	17.5
Ti I (6149.725)	-	17.5
Fe II (6150.113)	V I (6150.167)	17.5
Fe I (6301.499)	Fe I (6302.493)	17.5
Fe I (15648.515)	Fe I (15647.423)	36.0
Fe I (15652.882)	-	36.0

gas behaves ideally, any two thermodynamic variables (in addition to the line-of-sight velocity) is needed to completely define the state of the gas e.g. temperature and gas pressure (or number density or electronic pressure). Note that, in this work, other atmospheric variables such as magnetic field vector, micro- and macro- turbulence velocity are assumed to have negligible magnitude and thus do not contribute to spectra.

As mentioned in last section, all depths are decoupled in LTE assumption, and using the atmospheric variables we can compute the level population and the resulting opacity χ_λ and emissivity j_λ at each depth corresponding to the wavelengths that make up the spectral line we intend to synthesize. The ratio of j_λ and χ_λ gives us the source function and the optical depth at each scale is computed by integrating opacity on the spatial grid. We finally integrate the source function on the optical depth grid to compute the emergent spectra at each wavelength, and thus the spectral line.

The spectral lines (listed in Table A.1) synthesized through the mean MURaM atmosphere (see Section 3.1) using the forward solving capabilities of SIR are shown in Figure 1.5. The intensity shown in the plot is normalized to the corresponds intensity through the HSRA [18] model of the solar atmosphere. These spectral lines are consistently used throughout this thesis.

A.5 Summary

The main goal of solar spectroscopy is to allow us to infer the atmospheric properties of the medium that resulted in the spectra. This is possible because the physical properties of the atmosphere determines the overall shape of this spectral line e.g. temperature determines the source function, doppler width of the line and the collision frequency; gas pressure puts a constraint on the Saha equation, determines pressure broadening, and the collision rate; large-scale line-of-sight velocity shifts the overall line profile and gradients in this velocity can lead to asymmetry in the emergent line shape. Moreover, variable sensitivity of different wavelengths that make up a spectral line to different depths in the atmosphere allows us to do depth dependent inversion of these parameters. This dependence of spectral line shape on the physical properties of the atmosphere allows us to infer them given a spectra.

Appendix B

SIR node values for different cases

Table B.1: Node values when inverting using SIR

Inverting	T nodes	V_{los} nodes	P_e nodes	Number of cycles
T	1,2,3,4,5,6,8,10[a]	0	1[b]	8
V_{los}	0	1,2,3,4,5,6,8,10	0	8
P_e	0	0	1,2,3,4,5[c]	5
T, V_{los} and P_e	1,2,3,4,5,6,8,10	1,2,3,4,5,6,8,10	1,2,3,4,5	8

Notes.
[a] Comma separated values correspond to the node value used in a given cycle.
[b] P_e inversion required else SIR inverts for T assuming *hydrostatic equilibrium*. Inverted $\mathbf{\Delta P_e}$ is manually set to 0 to be consistent with single variable T inversion.
[c] SIR inverted P_e solutions (generally) deviate drastically from underlying P_e model for larger node values.

Table B.2: Node values when inverting using SIR within HOLA framework

Inverting	T nodes	V_{los} nodes	P_e nodes	Number of cycles
T	1,2[a]	0	1[b]	2
V_{los}	0	1,2	0	2
P_e	0	0	1[c]	2
T, V_{los} and P_e	1,2	1,2	1	2

Notes.
[a] Node value to make large-scale constant/linear updates.
[b] P_e inversion required else SIR inverts for T assuming *hydrostatic equilibrium*. Inverted $\mathbf{\Delta P_e}$ is manually set to 0 to be consistent with single variable T inversion.
[c] Unlike for other variables, SIR inverts for P_e in fractional units. So, P_e node value = 1 is more consistent with linear updates.